The Legendre Polynomial Axial Expansion Method

by

Nicholas F. Herring

A dissertation submitted in partial fulfillment
of the requirements for the degree of
Doctor of Philosophy
(Nuclear Engineering and Radiological Sciences)
in the University of Michigan
2022

Doctoral Committee:

Adjunct Professor Benjamin Collins, Co-Chair
Professor Thomas Downar, Co-Chair
Assistant Professor Brendan Kochunas
Professor Divakar Viswanath

Nicholas F. Herring
nfherrin@umich.edu
ORCID iD: 0000-0002-0614-2486

For my family, Jim, Anita, Rebecca, and Nolan. Without whom I would not have found the patience, support, or confidence to finish my PhD.

ACKNOWLEDGMENTS

This thesis is a monument to the support and contributions of the scientists and engineers in my life. I did not do this work alone, and every engineer I have interacted with over these past 8 years as a nuclear engineering student has my thanks for the contributions they have made, intentional or incidental

First, I would like to thank my advisor Prof. Thomas Downar, who has been an incredible help in keeping me on track and pushing me to do my best work. Without him I would likely not have come to the University of Michigan and my PhD experience would have otherwise been poorer. The expertise and intelligence found in both students and scientists that Prof. Downar has assembled into his group at the University of Michigan has been an invaluable source of both information and inspiration.

Second, I would like to thank my co-advisor, Dr. Benjamin Collins. It is through my work with him as an intern at ORNL in summer of 2019 that the subject of this dissertation was initially proposed and explored. Dr. Collins has been invaluable in the development of this dissertation and my weekly meetings with him have kept me grounded and focused despite the strange circumstances of the pandemic.

I would also like to thank Dr. Aaron Graham and the MPACT team at Oak Ridge National Laboratory. Discussion and meetings with the MPACT team proved valuable as both a place to share my work, as well as a place to get feedback and advice when difficulties arose.

Finally, I would like to thank the DOE for the NEUP fellowship that funded my first two years as a PhD student, and later the funding provided by ORNL at the end of my time as a student.

TABLE OF CONTENTS

LIST OF TABLES

LIST OF FIGURES

LIST OF ALGORITHMS

LIST OF ABBREVIATIONS

NTE *Neutron Transport Equation*

CMFD *Coarse Mesh Finite Difference*

MOC *Method of Characteristics*

LWR *Light Water Reactor*

ODE *Ordinary Differential Equation*

PDE *Partial Differential Equation*

MPACT *Michigan PArallel Characteristics-based Transport*

ANL *Argonne National Laboratory*

FSR *Flat Source Region*

LPAEM *Legendre Polynomial Axial Expansion Method*

KAERI *Korea Atomic Energy Research Institute*

KAIST *Korea Advanced Institute of Science and Technology*

ABSTRACT

Designing and analyzing nuclear reactors requires the development of software tools for the simulation of reactor physics. One of the most important aspects of reactor simulation is the determination of the distribution of neutrons in the system. This distribution is described by a *Partial Differential Equation* (PDE) called the *Neutron Transport Equation* (NTE). Typical reactor systems are too complex to analytically solve the NTE, so instead computational methods of solving the equation are developed and used.

A variety of methods to efficiently solve the 3D NTE for reactor systems have been devised. Prominent among these methods are the 2D/1D methods. Traditional 2D/1D methods generate a 3D solution to the NTE by iteratively solving 2D radial transport equations coupled with 1D axial P_N equations.

The standard iterative methods to solve the traditional 2D/1D equations have inherent instabilities. These instabilities can lead to divergence of the problem solution. The instabilities are of particular concern in problems with neutronically important void-like regions adjacent fuel.

This work proposes to fill in these limitations of traditional 2D/1D methods in *Michigan PArallel Characteristics-based Transport* (MPACT) for such problems using the axial expansion method. Proposed by *Argonne National Laboratory* (ANL) and first implemented in Proteus-MOC, axial expansion methods directly solve the full 3D NTE, but use *Method of Characteristics* (MOC) for the discretization of the radial direction, while using discontinuous finite element methods for the axial direction treatment. This work develops a new discretization using an explicit Legendre polynomial form for the axial expansion, and introduces an alternative axial coupling treatment to allow for non-extruded axial meshes.

One of the most computationally expensive portions of axial expansion methods involves the calculation of matrix exponentials. While the matrix exponential is well defined, general explicit forms are only known for up to 3×3 matrices. The explicit *Legendre Polynomial Axial Expansion Method* (LPAEM) formulation allowed investigation into the precise form of the matrix exponentials present in the calculation. This investigation revealed a form that lent itself to matrix exponential tables, which showed substantial speedup compared to analytic or iterative methods of computing the matrix exponential.

This work implements the LPAEM with non-extruded axial mesh coupling and matrix exponential tables in the reactor physics code MPACT. Using this implementation, numerical investigations into the stability of the method in comparison to traditional 2D/1D are performed. The investigations performed in this work demonstrate the stability of the axial expansion method in systems with neutronically important void-like regions adjacent to fuel, that fail to converge using traditional 2D/1D.

CHAPTER 1

Introduction

This chapter describes the motivation for solving the 3D *Neutron Transport Equation* (NTE) using the *Legendre Polynomial Axial Expansion Method* (LPAEM). This motivation is primarily found in limitations present in traditional 2D/1D methods for solving the transport equation. A brief history of some "2D/1D" like methods is then given to describe current methods of efficient deterministic neutron transport in 3D. The uniqueness of the LPAEM lies in the fact that it solves only a single set of axial moment equations for the system, so there exists no discontinuity between the axial and radial solution, nor is there an independent axial equation to solve. At the end of this chapter, an outline is given for the remainder of the dissertation, in which this method of solving 3D neutron transport is developed and tested.

1.1 Motivation

Current nuclear reactors produce power through the fissioning of heavy particles of fuel material, often unstable isotopes of Uranium [1]. In a reactor, this fission process is primarily driven by incident collisions with free neutrons in the system [2]. We call the rate of fission incidents the "reaction rate" for fission, and this rate is the primary determinant of power production in a nuclear reactor. The interaction probability for a single incident is primarily dependent upon the speed, or energy, of the free neutron [3]. The reaction rate as a whole is also determined by the number of potential incidents, which is dependent upon the density of free neutrons and fissionable material within a given region of space. The density of fissionable material in a given space is typically known due to manufacturer specifications, or can be determined through depletion physics in situations where the system has been irradiated for some time. As such, the primary unknown needed to determine reactor power and spatial distribution of power production, is the energy and spatial distribution of the density of free neutrons in the system [4].

The density distribution of neutrons can be described by the linearized Boltzmann equation, often referred to as the NTE [5]. This seven dimensional *Partial Differential Equation* (PDE),

which is also an integro-differential equation, is too complex to solve analytically for typical reactor systems. As such, numerical methods are often used and the power of modern computers is applied to solve the system. For reactor design, this solution typically comes in the form of a computational deterministic solution to this equation. Stochastic methods can also be used, however the costs of stochastic simulations for the level of accuracy needed is often prohibitive in large, complex reactor systems.

The *Method of Characteristics* (MOC) is commonly used in reactor physics computations to deterministically solve the NTE in 2D [6]. MOC involves using a change of variables in which a multivariate PDE can be rewritten as a single-variable *Ordinary Differential Equation* (ODE) along a track length for several rays in discrete angular ordinates, e.g. the characteristic directions of the solution. In 2D, it is fairly simple to keep the number of rays relatively limited. However, in 3D, despite recent work to improve the speed of 3D MOC [7], it can sometimes be untenable to perform a full MOC calculation since the number of rays is increased geometrically and the cost of a single iteration can be very expensive. This is especially true for complex reactor systems. To avoid this issue, many MOC codes take advantage of the broadly invariant axial properties of typical reactor designs by treating the axial direction differently, performing full 2D MOC in several radial slices and using a simpler approximation to couple each slice together axially.

Many methods perform this coupling through an additional transverse leakage term in the source, and the *Michigan PArallel Characteristics-based Transport* (MPACT) code is no exception. MPACT's current standard 2D/1D method uses a P_3 angular approximation and a 4th order polynomial to solve for a coarse axial shape in each pin cell. This approximation is fairly cheap and allows pin cells to have *Flat Source Region* (FSR) variations without the need for cell extrusion. However, this method does have several limitations. Inconsistencies between the radial and axial solution methods occasionally cause negative fluxes that require nonphysical means of correction, or may compound with other instabilities in the solution and cause the problem to fail to converge.

Perhaps most concerning, traditional 2D/1D methods rely on a pin cell radially homogenized P_N approximations [8] to solve the axial variance. The formulation and coupling of the axial equations to the 2D radial MOC, can sometimes introduce instability in the iterative calculation. One situation where this can occur is when neutronically important regions of void, or void-like low density material, are present. Because low density materials are quite non-diffusive, they are not well approximated by P_N equations. This leads to the axial solver being unstable, increasing the instability that can lead to solution break down in these types of problems.

One of the more interesting systems where these limitations are on display, are some critical experiments that vary the water level to control criticality. One example is the KRITZ-2 experiments. These were a series of critical configurations where an assembly of fuel rods were placed in a containment vessel and the moderator height was adjusted along with boron concentration in order

to achieve a critical configuration. This was done with multiple different temperatures for multiple different fuel assemblies [9] [10] [11].

A side view of the KRITZ-2:1 experiment at 19.7° C is shown in Figure 1.1. It is here that it can be observed that the system has large regions of importance above the water line. Indeed, in the critical configuration, only 65.28 cm of the 200 cm of active fuel available is covered by the moderator. For the rest of the fuel above the water line, the fuel pins are surrounded by air, which given its low density, is very nearly approximated as void in the small gaps between the fuel pins.

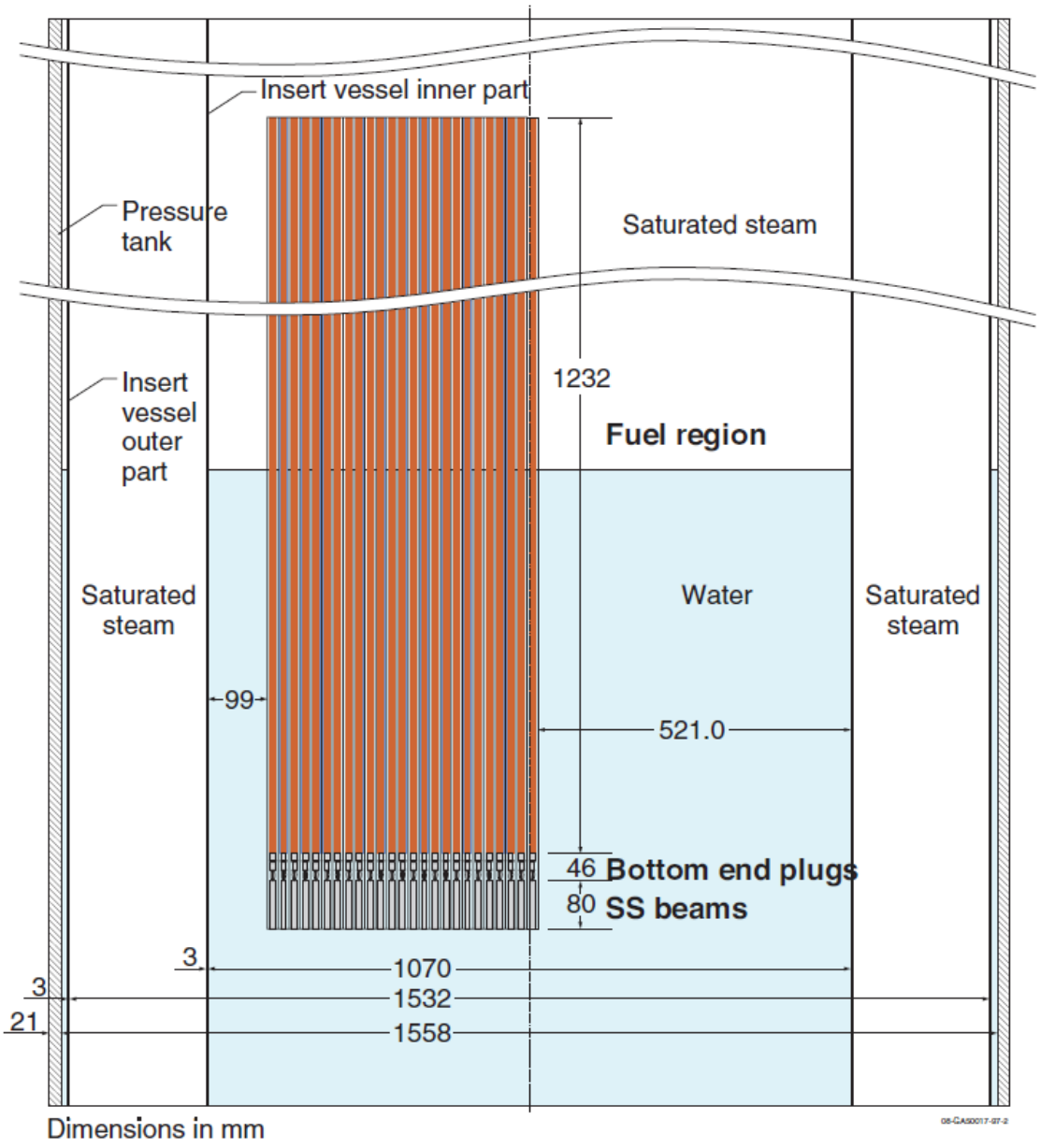

Figure 1.1: KRITZ-2:1 Side-view [9]

KRITZ-2 is a popular benchmark problem for both deterministic [12] [13] [14] and Monte Carlo [15] codes because of its unique characteristics such as variable temperature. Benchmarking for two of these configurations, KRITZ-2:1 and KRITZ-2:13, were attempted with MPACT [16]. Because traditional 2D/1D can be unstable in systems with voided regions that have non-negligible neutronic importance, successful MPACT solutions to these configurations were limited to 2D models with the reported axial critical buckling. While these 2D simulations were successful, they left something to be desired in simulating the full 3D system. 3D models inspired by the KRITZ-2 experiments were created with the fuel above the water line removed from the model, however the fuel above the water line is neutronically important and led to an underestimation of the eigenvalue. Models were also made with artificially increased density for the air to avoid the void problem in 2D/1D, however this led to additional moderation and reflection above the water line and an overestimation of the eigenvalue.

The KRITZ-2 experiments are considered important evaluated reactor physics benchmarks with criticality and reaction rate measurements. However, the data for the critical buckling is not considered an acceptable benchmark experiment for critical buckling benchmarks. As such, the limited benchmarking that MPACT has been able to perform on KRITZ-2 does not provide a sufficient case of verification and validation of the code using KRITZ-2 since it is limited to buckling calculations. This prevents the KRITZ-2 experiments from being added to the list of critical experiments used to validate MPACT [17], though MPACT remains well validated with conventional LWR type problems.

To address these limitations, an alternative method of 2D/1D was proposed to be added to MPACT's capabilities. Inspired by Proteus-MOC [18], this new method expands the axial component of the transport equation by using an arbitrary number of Legendre polynomials. In this new method, the unknowns of the system become the coefficients associated with these polynomials. So now, the solution on a radial slice can give the leakage to adjacent slices for both upward and downward traveling neutrons averaged over a coarse pin cell from the polynomial value at the borders. This method should not break down for arbitrarily small slices compared with MPACT's current 2D/1D method due to the lack of transverse leakage from a separate equation. Additionally, since the method directly approximates the transport equation, some instabilities introduced in traditional 2D/1D are expected to be avoided for problems with void-like regions adjacent to the fuel. The implementation in MPACT also does not require *Coarse Mesh Finite Difference* (CMFD) acceleration for problems in which CMFD might not easily converge—a capability that MPACT currently lacks for 3D systems, except when using prohibitively expensive full 3D MOC.

To demonstrate the viability of this method before MPACT implementation, an exploratory 2D code was created and directly compared with MPACT's current method [19]. Referred to as *1D/1D*, these problems allowed for the investigation of method behaviors in a simple testing

environment. This method was then implemented in MPACT and correctness of the method and implementation is demonstrated by comparison to MPACT's current 2D/1D implementation on a variety of demonstration problems, among them configurations of KRITZ-2.

Following these initial exploratory studies, the axial expansion method was implemented into MPACT and a fast method for the necessary matrix exponential computations was devised [20]. The implementation was tested on small scale systems to confirm correctness of the method and implementation in 3D in MPACT. The implementation was later extended to include linkage with CMFD and used in analysis of the KRITZ-2:1 experiment where it showed success in converging in models where traditional 2D/1D failed.

1.2 History of 2D/1D Methods

The idea of splitting up the 3D transport equation in a 2D/1D like manner that treats the axial portion in a distinct fashion from the radial portion has its roots in two independent publications from 2002. These two methods were the "2D/1D" method developed by the *Korea Atomic Energy Research Institute* (KAERI) to be used in DeCART [21] (and later nTRACER [22]) and the "2D/1D Fusion" method developed by the *Korea Advanced Institute of Science and Technology* (KAIST) for the CRX code [23] [24].

The original method implemented in MPACT used isotropic transverse leakage, which is the leakage between axial slices determined by the 1D solution described further in Section 2.6, and was similar to the method from KAERI. This method treats the axial component of the system using nodal diffusion solvers to approximate the axial shape of the flux. Not content with the error introduced by the isotropic treatment, later on, Stimpson [25] implemented a similar method in MPACT that utilized anisotropic leakage making it more similar to the KAIST method. In order to save memory from the explicit azimuthal treatment of the KAIST method, Stimpson's solver used a Fourier expansion in the azimuthal angle for the axial and radial transverse leakage. Additionally, memory was saved in the solver by using P_3 Legendre polynomial expansions of the polar angle instead of the explicit treatment in the original KAIST method. Analysis of errors determined that one of the most significant sources of error left in the 2D/1D method in MPACT was in the form of the cross section homogenization in the nodal solver. To fix this, Jarrett [26] introduced anisotropic cross sections with the anisotropic transverse leakage, which showed significant improvements in the accuracy of the 2D/1D method in MPACT, primarily in the polar direction.

As MPACT was being developed, an alternative method at *Argonne National Laboratory* (ANL), was being developed from the basic concepts in DeCART for use with the Proteus-MOC code [18]. This method uses 2D MOC with a finite element discretization in the axial direction to technically make it a 3D transport method. It can still be considered a type of 2D/1D method

in the sense that it treats the axial and radial directions of the domain differently with respect to the discretization method. However, it is distinguished from traditional 2D/1D methods in that the 3D transport equation is treated and discretized directly, albeit differently in different directions. This discretization also does not require the solving of a 1D homogenized problem. Other codes that adopted similar methods to solve the 3D transport equation with 2D/1D like methods through alternative axial discretization include APOLLO3 [27], PANX [28], NECP-X [29], and STREAM [30]. These methods are disadvantaged in the fact that they tend to be computationally more expensive on the same mesh due to their finer treatment of the axial direction and direct discretization of the 3D transport equation.

Now, traditional 2D/1D methods can have stability issues in part due to the fact that the axial portion of the calculation is not a different discretization of the axial direction, but instead an entirely different equation [31]. In particular, the cross section homogenization in traditional 2D/1D methods coupled with the 1D P_N axial solution can be unstable in optically thin regions. Additionally, the nodal methods used to solve the axial portion in traditional 2D/1D methods has stability issues in the presence of axially thin radial slices in systems where they may be required. For systems where large voided regions are unlikely, such as most *Light Water Reactor* (LWR) models, traditional 2D/1D methods have sufficient accuracy and stability while maintaining computational efficiency.

This dissertation focuses on extending the development of the direct 2D/1D method proposed by ANL for use in more diverse meshes through the removal of fine mesh extrusion requirements. Additionally, the re-development of the method here with explicit use of Legendre Polynomials allows for further work on method performance enhancements both through fine mesh extrusion removal as well as the introduction of matrix exponential tables. The method is also implemented in MPACT to allow for development and testing by a more diverse set of scientists and engineers and demonstrations on problems featuring void-like regions is performed to demonstrate the theorized stability.

1.2.1 Failure in Void-like Regions

One of the largest concerns with traditional 2D/1D methods is failure in optically thin regions. In general, P_N approximations will do poorly in terms of accuracy when there is a lot of anisotropy, like when a void-like region is connected to a non-void region. However, this lack of accuracy is often not as relevant as the instability that traditional 2D/1D methods often face in these problems. Regardless of the accuracy of the solution, if the solution method is not robust then a solution may not be able to be reached at all. The axial transverse leakage can be very large at the interface between void and non-void regions. A large negative transverse leakage could lead to instability in the solver itself, and additionally since the scattering source in void is very small, a strong

negative transverse leakage can also lead to negative fluxes, which may themselves cause additional instability.

As mentioned in Section 1.1, instability of the 2D/1D method was examined in the particular instance of the KRITZ-2 experiments. The lack of convergence in 2D/1D problems is due to at least 3 types of instability related to 2D/1D that can cause a solution to be non-convergent [31].

1. Instability arising from thin axial slices can cause the 2D/1D problem to diverge. Work has been done to mitigate this to allow 2D/1D to typically converge even with very thin axial slices [32].

2. CMFD acceleration may cause instability in situations where some coarse cells are too thick. This concern can be solved by reducing the coarse cell size, but can pose a problem since that 2D/1D is almost exclusively solved using CMFD acceleration, and in fact can only be solved using CMFD in the current MPACT implementation.

3. The axial transverse leakage can go negative in traditional 2D/1D. This is fine as it is just the flow of neutrons normal to a surface. However, this can potentially produce a negative source if the magnitude of the transverse leakage is large enough, and the remaining source in a region is sufficiently small.

It is the third instability which can occur in systems with void-like regions that fail to converge. If the transverse leakage is very strongly negative due to production in the non-void like region, then the low void scattering source is unlikely to be large enough to overcome it. This can lead to the angular source becoming negative in some regions and directions, and potentially even the scalar flux could become negative in certain regions. Negative fluxes in a FSR could lead to the homogenized cross section for that pin cell becoming non-physical during the cross section homogenization portion of traditional 2D/1D methods described in Section 2.6.1. This non-physicality can be the result of either a very small, or even negative, number in the denominator of Eq. 2.57.

A very large or negative homogenized cross section could cause instability in both the 1D axial calculation and the CMFD acceleration. As such, even with the removal of CMFD in systems where this instability prevents convergence, it is not guaranteed that the 2D/1D method alone will converge. This problem can be exacerbated with a large number of energy groups since scattering in these problems tends to be even lower for each individual group, but the transverse leakage may still be non-negligibly negative. With less groups, the overall scattering source is more likely to be large enough to overcome negative transverse leakage sources due to less spectrum peaking of the scattering source. So this presents the problem that some systems may converge as few group problems with void-like regions but then fail to converge when the number of groups is increased, as may be necessary to obtain a sufficient accuracy.

Furthermore, anisotropic transverse leakage can also make the instability more likely to occur. Because the transverse leakage is now peaked along certain directions, negativity of the angular flux has more opportunities to occur. This is especially a problem at an axial boundary between reflector and void since the anisotropic peaking of the axial transverse leakage can be particularly high at those locations. One of the standard ways to fix negative transverse leakage is to use transverse leakage splitting. However, transverse leakage splitting is best used for isotropic transverse leakage, since with anisotropic transverse leakage it will completely change the anisotropic distribution of the leakage and defeat the purpose of anisotropic transverse leakage.

So this means that the two of the most important methods to increase problem accuracy, finer energy groups and anisotropic axial leakage, both increase the likelihood of instability occuring in 2D/1D. Additionally, the fix for transverse leakage leaves anisotropic transverse leakage ineffective.

Some work has been done to fix some aspects of the instability here. Recently, a linearized CMFD acceleration technique was developed [33] [34] to increase the stability of the solution in systems where the CMFD homogenized cross sections, or fluxes, become very large or negative. However, the homogenized cross sections for the 1D problem may still become negative or very large, and may still lead to instability and non-convergence in the 2D/1D solution even if the instability in CMFD is properly addressed. Additionally, an improved leakage splitting method has been proposed to potentially resolve some of the instability caused by negative leakage while maintaining some of the accuracy of anisotropic leakage [35]. But this leakage splitting method is still relatively young and has yet to be tested in systems with void-like regions where the instability is prominent.

1.3 Outline

This doctoral dissertation thesis seeks to present research in reactor physics that is both significant and original. The significance of this work involves the implementation in MPACT of an alternative to traditional 2D/1D that is more stable in some problematic systems. The originality of this work is threefold. First, the new reformulation of the axial leakage term for the axial expansion method allows the method to be used with meshes that do not possess extruded FSRs, which is a common feature of LWR design models due to buffers of water above and below the fuel that are not modeled well with the same FSR divisions found in fuel cells. This reformulation also introduces significant memory savings since each FSR need not store a separate axial leakage term. Second, the re-derivation of the axial expansion method explicitly using Legendre polynomials led to an investigation of performance improvements, including the development of efficient matrix exponential tables that provide significant speedup with minimal memory increase and negligible pre-calculation computational costs. Third, while the axial expansion method had previously been

reported to have additional stability in problems with void-like regions compared to traditional 2D/1D methods, the research performed here demonstrated this for the first time using original models as well as international benchmark problems of the KRITZ-2:1 critical experiments. This demonstration of stability represents a significant new capability for the MPACT code.

The remainder of this dissertation is structured as follows. Chapter 2 provides an overview of neutron transport theory centered around the NTE. This chapter describes the equation and its terms in a general time dependent system. The eigenvalue problems more commonly found in computational codes are then introduced, with particular emphasis on the k_{eff} eigenvalue problem, which is the problem that the method in this dissertation is used to solve. The two primary computational methods for solving the transport equation are then briefly described and advantages of both are discussed. Focus is then shifted solely to deterministic methods and common means of discretization and solution computation and described.

Chapter 3 gives a mathematical foundation for the LPAEM. Here the method is derived from the discretized transport equation by introducing the axial expansion approximation, taking axial moments of the approximated equation, and finally reforming the equation in matrix-vector notation. Balance equations are then derived to demonstrate that the approximation preserves neutron balance. To close out the chapter, three forms of axial leakage treatments are introduced, and while all three have been implemented in the exploratory code, it was determined that the integrated pin cell method would serve as the primary axial leakage function for implementation in MPACT.

Chapter 4 describes numerical methods for solving the axial expansion method. Here is detailed the 1D/1D equations used in the initial investigation into the method as well as the 2D/1D MOC equations needed for a complete 3D simulation. Next, details for proper CMFD acceleration are described to guarantee that the axial moments are properly updated from the CMFD solutions. Afterwords a fast method for solving matrix exponentials is introduced in the form of matrix exponential lookup tables. The chapter closes out with a detailed analysis of the predicted memory usage for this method, as well as a comparison to the memory usage for traditional 2D/1D.

Chapter 5 describes the verification and validation campaigns performed for this dissertation. In this chapter demonstration 1D/1D problems are described and their results analyzed from the initial exploratory code. More complex 2D/1D problems are then introduced and their results in MPACT using the axial expansion method are analyzed, including a B&W 1484 critical experiment. The KRITZ-2 experiments are then introduced in more complete detail and their results in MPACT using the axial expansion method are analyzed. To close out, the chapter investigates the speedup provided by the matrix exponential tables introduced in chapter 4.

Finally, Chapter 6 presents the conclusion to the work. A summary of the motivation, method, results, and analysis is reiterated. Concluding this chapter, potential future work and investigations related to the LPAEM are described.

CHAPTER 2

Neutron Transport Theory

This chapter describes neutron transport theory in nuclear reactor simulations. The NTE is introduced and described physically. Additionally, the eigenvalue forms of this equation are described. Computational methods for solving the equation are discussed and discretization methods are presented. Finally, brief discussion of solution methods for deterministically solving the equation are introduced.

The NTE itself has been well documented and constitutes one of the core equations of nuclear engineering as it describes the distribution of neutrons throughout a system [36] [37] [38]. The angular neutron flux, ψ, is the principal unknown in neutron transport theory and is defined as the speed of the neutrons, v, multiplied by the density distribution of the neutrons, N. It is a seven dimensional distribution dependent on 3 spatial variables, $\boldsymbol{r} = (x, y, z)$, the neutron energy (or speed), $E = \frac{1}{2}mv^2$, the two variables describing direction of flight $\hat{\Omega} = (\sqrt{1-\mu^2}\cos\omega, \sqrt{1-\mu^2}\sin\omega, \mu)$ where μ is the polar angle cosine and ω is the azimuthal direction, and the time, t. The conglomeration of these seven dimensional variables is often called "phase-space".

2.1 The Boltzmann Transport Equation

We define the linear "loss" operator due to streaming and collision as:

$$\mathbf{L}\psi(\boldsymbol{r}, \hat{\Omega}, E, t) = \hat{\Omega} \cdot \boldsymbol{\nabla}\psi(\boldsymbol{r}, \hat{\Omega}, E, t) + \Sigma_t(\boldsymbol{r}, E, t)\psi(\boldsymbol{r}, \hat{\Omega}, E, t) \tag{2.1a}$$

Here Σ_t is the macroscopic total neutron cross section, independent of angular direction, which is a good approximation in reactor like systems where molecular arrangements rarely take forms that lend non-negligible angular dependence to cross sections.

And the linear "secondary source" operator due to in-scattering and fission is defined as:

$$\mathbf{S}\psi(\boldsymbol{r},\hat{\Omega},E,t) = \int_{4\pi}\int_{0}^{\infty} \Sigma_s(\boldsymbol{r},\hat{\Omega}\cdot\hat{\Omega}',E'\rightarrow E,t)\psi(\boldsymbol{r},\hat{\Omega}',E',t)\,dE'\,d\Omega' + \frac{\chi(\boldsymbol{r},E,t)}{4\pi}\int_{4\pi}\int_{0}^{\infty} \nu\Sigma_f(\boldsymbol{r},E',t)\psi(\boldsymbol{r},\hat{\Omega}',E',t)\,dE'\,d\Omega' \quad (2.1b)$$

Here Σ_s is the macroscopic scattering cross section, whose sole angular dependence is found in the scattering cosine, $\hat{\Omega}\cdot\hat{\Omega}'$. $\nu\Sigma_f$ is the macroscopic fission production cross section, and is the product of the average neutron production per fission event, ν, and the macroscopic fission cross section, Σ_f. χ is the fission production spectrum which, in reality, is not independent of incident neutron energy and is not isotropic. However, at the neutron energies that produce the bulk of induced fissions in a nuclear reactor, χ has very little dependence on incident neutron energy and is nearly isotropic, so it is approximated as such.

Then the time dependent linearized 3D Boltzmann equation (NTE) is:

$$\frac{1}{v}\frac{\partial}{\partial t}\psi(\boldsymbol{r},\hat{\Omega},E,t) + \mathbf{L}\psi(\boldsymbol{r},\hat{\Omega},E,t) = \mathbf{S}\psi(\boldsymbol{r},\hat{\Omega},E,t) + Q(\boldsymbol{r},\hat{\Omega},E,t), \quad \boldsymbol{r}\in V, \quad \hat{\Omega}\in 4\pi, \quad 0<E<\infty \quad (2.1c)$$

Where Q is some known external source.

This equation can have general specified boundary conditions:

$$\psi(\boldsymbol{r},\hat{\Omega},E,t) = \Gamma(\boldsymbol{r},\hat{\Omega},E,t), \quad \boldsymbol{r}\in\partial V, \quad \hat{\Omega}\cdot\hat{n}<0, \quad 0<E<\infty \quad (2.1d)$$

Where $\hat{n}$ is the outward normal unit vector of the system boundary surface. For this work we will arbitrarily assume that the system volume V is a general right convex prism so that the "top" and "bottom" of the system are at $z = Z_{max}$ and $z = 0$ respectively and the system boundary is $\partial V = \partial V_R(x,y)\,\forall\ 0<z<Z_{max}\cup(x,y,0)\in V\cup(x,y,Z_{max})\in V$.

2.2 Eigenvalue Problems

Time dependence in neutron transport problems provides a unique issue since the equation is often quite expensive and must normally be solved iteratively with temperature feedback in reactor applications. However, most systems are time dependent. This prompts us to convert the equation to an eigenvalue problem where the flux is now an eigenfunction in the system. As eigenvalues problems, we must necessarily remove the external source, Q, from the problem.

2.2.1 k_{eff} Eigenvalue

Perhaps the most common eigenvalue problem in neutron transport theory is the k_{eff} eigenvalue problem. For this problem, the eigenvalue is defined as the value that when dividing the fission source, causes total system integral of the flux to lose all time dependence:

$$\hat{\Omega}\cdot\boldsymbol{\nabla}\psi(\boldsymbol{r},\hat{\Omega},E)+\Sigma_t(\boldsymbol{r},E)\psi(\boldsymbol{r},\hat{\Omega},E)=\int_{4\pi}\int_0^\infty\Sigma_s(\boldsymbol{r},\hat{\Omega}\cdot\hat{\Omega}',E'\rightarrow E)\psi(\boldsymbol{r},\hat{\Omega}',E')\,dE'\,d\Omega' + \frac{\chi(\boldsymbol{r},E)}{k_{eff}4\pi}\int_{4\pi}\int_0^\infty\nu\Sigma_f(\boldsymbol{r},E')\psi(\boldsymbol{r},\hat{\Omega}',E')\,dE'\,d\Omega' \quad (2.2)$$

So that now k_{eff} is the eigenvalue for the eigenfunction ψ.

The value of k_{eff} is then determined by the ratio of the neutron leakage and absorption loss to the production of neutrons through fission. As such, for $k_{eff}<1$ the actual system would be time dependent with flux decreasing with time and the system is said to be sub-critical. For $k_{eff}>1$ the actual system would be time dependent with flux increasing with time and the system is said to be supercritical. For $k_{eff}=1$ the actual system would be steady state with constant flux in time and the system is said to be critical. Distance of k_{eff} from 1 also determines the rate at which the flux is changing and as such, k_{eff} is one of the most important parameters in reactor analysis. Finally, the closer k_{eff} is to 1, the closer the eigenfunction ψ will be to the true flux distribution in terms of spatial, directional, and energy shape.

2.2.2 α Eigenvalue

It is the k_{eff} eigenvalue problem that is most commonly solved by neutron transport codes, however, other eigenvalue problems exist. Perhaps most notably, the α eigenvalue problem is often solved to give a more precise asymptotic rate to the change in the flux for non steady state problems. This problem assumes a time independent flux shape, the eigenfunction ψ, and that the time dependence of the magnitude of that flux is exponential with a rate coefficient of α. So with this approximation, the NTE becomes:

$$\frac{1}{v}\frac{\partial}{\partial t}\psi(\boldsymbol{r},\hat{\Omega},E)e^{\alpha t}+\mathbf{L}\psi(\boldsymbol{r},\hat{\Omega},E)e^{\alpha t}=\mathbf{S}\psi(\boldsymbol{r},\hat{\Omega},E)e^{\alpha t} \quad (2.3)$$

Which then gives the α eigenvalue problem:

$$\sqrt{2E/m}(\mathbf{S}-\mathbf{L})\psi(\boldsymbol{r},\hat{\Omega},E)=\alpha\psi(\boldsymbol{r},\hat{\Omega},E) \quad (2.4)$$

Now when α is negative, the system is sub-critical, when it is positive the system is supercritical, and when it is 0 the system is critical. Similar to k, the closer α is to 0 (the critical value), the closer

the true physical flux shape will be to the eigenfunction shape ψ. So now for a solved α eigenvalue problem a relatively accurate description of the asymptotic rate of change in the flux magnitude in a system is known.

2.3 Computational Methods

The NTE can be solved a variety of ways but every method of solving the equation falls into one of two categories. The solutions are either computed stochastically or deterministically. Stochastic methods for neutron transport are typically called "Monte Carlo" methods and simulate particles individually as they move through the system. The solution is then composed of the distribution of the simulated particles with some uncertainty dependent upon the number of particles simulated. Deterministic methods instead attempt to solve the NTE as a differential equation directly through some discretization approximations to the system. Typically deterministic methods are faster than Monte Carlo methods, however discretization approximations may make them less accurate. For design and reactor simulation purposes, deterministic methods are therefore more commonly used as the systems are quite large and complex.

2.3.1 Monte Carlo Methods

Solutions of the NTE can be obtained without solving the actual PDE at all. These stochastic methods of determining the neutron distribution in a system are referred to as Monte Carlo methods.

Monte Carlo methods involve direct simulation of particle histories, probabilistically sampling particle creation, collision, scattering, and fission induction [39]. These simulations are normally done in batches of neutrons born from fission, where a number of neutrons making up the batch are followed and individually simulated until absorption. For this method, because it is unknown prior to solving the system where fission neutrons will be born, typically a few uncounted batches are run to approximate the fission source distribution. These uncounted batches are discarded in the tallied data, but the fission source they estimate is used as the starting point for the counted batches.

Because these simulations follow individual particles, the need for discretization of phase-space is removed unless phase-space specific values are sought. Not every point in phase-space will be seen with a finite amount of particle histories, and technically some discretization is present due to the finite precision nature of computers. However, it is approximately accurate to say that Monte Carlo methods remove the need for discretization found in deterministic solutions, except in the case when they are used for depletion and feedback modeling. As such, errors introduced by multi-group cross sections, finite angular quadrature sets, and FSR approximations are all avoided by Monte Carlo methods. This leads to Monte Carlo methods being considered highly accurate in comparison

to deterministic methods.

Unfortunately, as a stochastic method, values tallied from results of Monte Carlo simulations are subject to inherent statistical error since the number of particles simulated is necessarily finite. This statistical error is proportional to $\frac{1}{\sqrt{N}}$, where N is the number of particle histories simulated. As such, the statistical error decreases increasingly slowly as the number of simulated particles increases, making certain levels of error untenable in large reactor systems. This leads to Monte Carlo methods being both less precise and much slower for sufficient precision compared to deterministic methods in large systems.

One additional drawback of Monte Carlo methods is that the continuous nature of the calculation does not naturally yield a phase space distribution for the neutron flux. Instead, integral quantities must be tallied for some phase-space discretization that must be determined before the run so that tallying may occur during the simulation. This requirement to predetermine phase-space tallied values before the sweep comes from the fact that saving all particle history data would be prohibitively expensive. The phase-space distribution values are essential for multi-physics and depletion calculations, making this discretization still necessary for Monte Carlo methods used in those contexts.

2.3.2 Deterministic Methods

Due to the computational costs of Monte Carlo simulations, for most reactor applications, the NTE itself is typically solved using discrete numerical methods. These methods are called deterministic methods, and involve various approximations and discretization of phase-space [40]. This discretization transforms the NTE from a PDE to a large algebraic system of equations. This system of equations is then solved, typically using iterative methods.

The introduction of discretizations reduces the accuracy of the solution since the discrete problem being solved no longer perfectly matches the true system that is being solved. However, the precision of the solution of the new algebraic system is very good with the limit typically being near machine precision. As such, the primary difficulty in deterministic methods is determination of discretization schemes that will provide an optimal balance of accuracy to the original problem and reasonable computational costs.

2.4 Discretization Methods

Perhaps the most important aspect of deterministic methods is the necessity of problem discretization. While Monte Carlo methods typically treat the phase-space continuously, this treatment is not possible in deterministic methods. As such, discretization schemes for energy, angle, and physical

space are necessary for a deterministic steady state transport solution. How these discretizations are developed has large impacts on both computational costs, as well as problem accuracy. As such, one of the most challenging parts of deterministic methods is determination of appropriate phase-space discretizations to give a problem that is computationally feasible, while still being sufficiently accurate.

2.4.1 Multi-group Energy Approximation

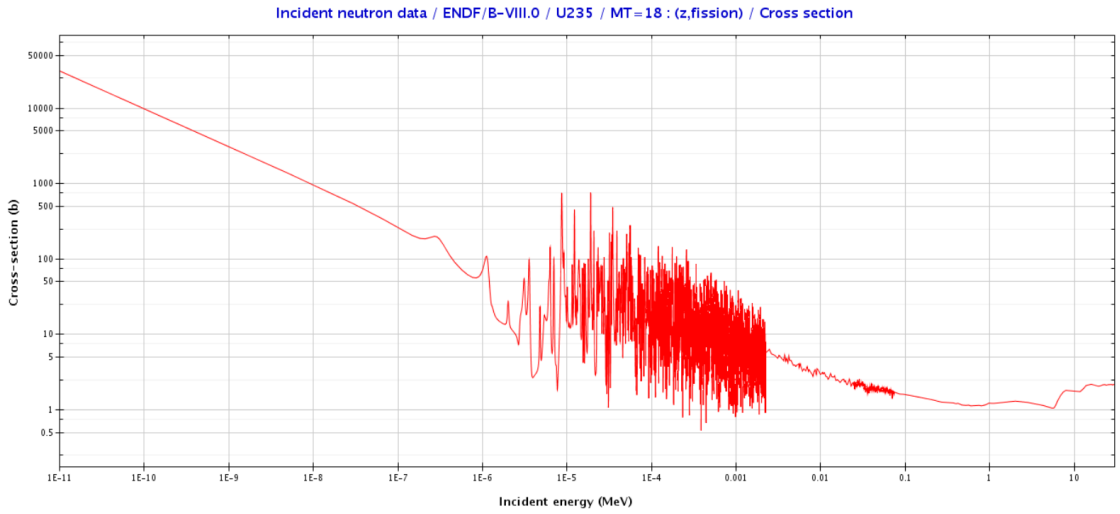

(a) Reactor Energy Range

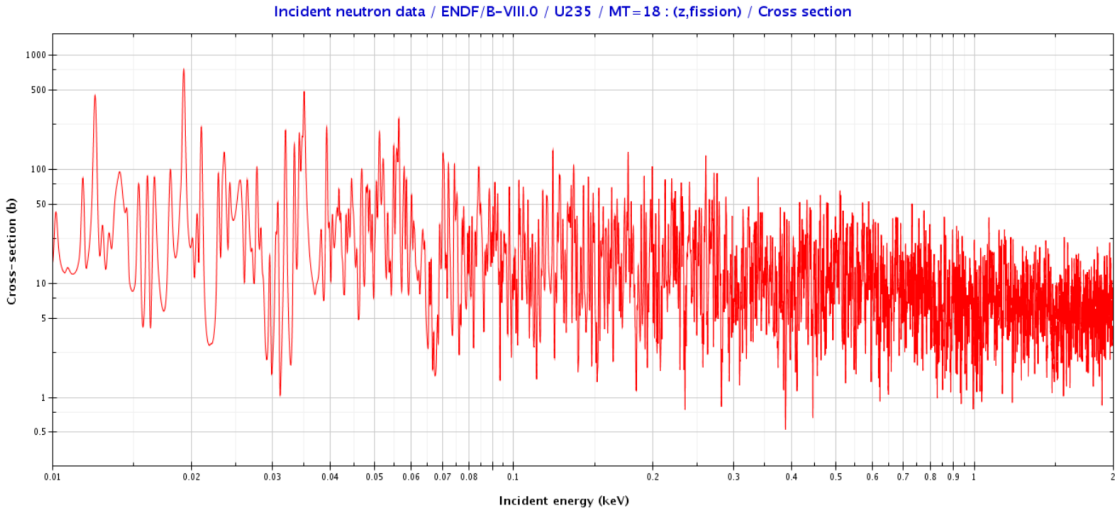

(b) Resonance Energy Range

Figure 2.1: U-235 Fission Cross Sections [41]

For deterministic methods, neutron energy is always treated discretely. To do this requires a multi-group approximations to the neutron energy spectrum. Nuclear reaction cross sections [42] are

highly dependent upon incident neutron energy and can be exceedingly complex, with academic research in cross sections being a driving force of nuclear physics research. This is evidenced by the fact that the subject of the very first dissertation in nuclear engineering was nuclear cross sections [43]. Because reaction rates are the driving force of the neutron distribution in a system, multi-group approximations attempt to capture effective cross sections in an energy range [44]. This is complicated by the fact that cross section energy dependence for most materials is highly variant, sometimes within a very small energy window as illustrated by Figure 2.1.

In particular, most cross sections feature resonance peaks and valleys within small neutron energy ranges. In ranges featuring these tight resonances, neutron energy spectrum is very important for accurate reaction rates. However, these resonances are too numerous to assign each an individual energy group, as such the expected energy distribution within a given energy group is pre-computed and used to reduce continuous energy cross sections to multi-group cross sections.

The total energy range of neutrons in the reactor is quite broad. Neutrons are found all the way down from thermal energy around 10^{-2} eV, to fast fission neutrons which can be produced at energies up to about 10^{7} eV. The microscopic U-235 fission cross section for the full reactor energy range is shown in Figure 2.1a and the complexity of these cross sections are further illustrated in the resonance energy range in Figure 2.1b. It can be seen that the resonance energy range consists of a large amount of variation in cross section magnitude, which makes up the primary complication in multi-group energy discretizations.

To precisely define the multi-group flux and multi-group cross sections, consider the steady state angular flux $\psi(\boldsymbol{r}, \hat{\Omega}, E)$. Define now a set of G energy groups with lower bounds ranging from $E_0 \to \infty$ (though E_0 is practically more or less 20 MeV), and $E_G = 0$ eV (though E_G is practically more or less 10 meV). Then the multi-group angular flux for energy group g is:

$$\psi_g(\boldsymbol{r}, \hat{\Omega}) = \int_{E_g}^{E_{g-1}} \psi(\boldsymbol{r}, \hat{\Omega}, E)\, dE \tag{2.5}$$

For calculating multi-group cross section, it is assumed that the flux energy spectrum will be separable from the angular portion. That is to say, it is assumed that the normalized energy spectrum at a given point is roughly the same for every angle. This normalized energy spectrum is also typically assumed to be weaker than $\psi(\boldsymbol{r}, \hat{\Omega}, E)$. This allows the multi-group cross sections to be independent of incident angle.

$$\psi(\boldsymbol{r}, \hat{\Omega}, E) \approx \varphi(\boldsymbol{r}, E)\gamma(\boldsymbol{r}, \hat{\Omega}) \tag{2.6}$$

and the multi-group macroscopic cross sections (sans scattering) are:

$$\Sigma_{x,g}(\boldsymbol{r}) = \frac{\int_{E_g}^{E_{g-1}} \Sigma_x(\boldsymbol{r}, E)\varphi(\boldsymbol{r}, E)\, dE}{\int_{E_g}^{E_{g-1}} \varphi(\boldsymbol{r}, E)\, dE} \tag{2.7}$$

The scattering cross section however, does retain the scattering cosine angle dependence so that it is defined as:

$$\Sigma_{s,g'\to g}(\boldsymbol{r}, \hat{\Omega}\cdot\hat{\Omega}') = \frac{\int_{E_{g'}}^{E_{g'-1}} \int_{E_g}^{E_{g-1}} \Sigma_s(\boldsymbol{r}, \hat{\Omega}\cdot\hat{\Omega}', E'\to E)\varphi(\boldsymbol{r}, E)\, dE\, dE'}{\int_{E_g}^{E_{g-1}} \varphi(\boldsymbol{r}, E)\, dE} \tag{2.8}$$

And the multi-group fission production spectrum is:

$$\chi_g(\boldsymbol{r}) = \int_{E_g}^{E_{g-1}} \chi(\boldsymbol{r}, E)\, dE \tag{2.9}$$

Then the multi-group k_{eff} eigenvalue transport equation is:

$$\begin{aligned}\hat{\Omega}\cdot\boldsymbol{\nabla}\psi_g(\boldsymbol{r}, \hat{\Omega}) + \Sigma_{t,g}(\boldsymbol{r})\psi_g(\boldsymbol{r}, \hat{\Omega}) = \sum_{g=1}^{G} \int_{4\pi} \Sigma_{s,g'\to g}(\boldsymbol{r}, \hat{\Omega}\cdot\hat{\Omega}')\psi_g(\boldsymbol{r}, \hat{\Omega}')\, d\Omega' \\ + \frac{\chi_g(\boldsymbol{r})}{k_{eff}4\pi} \sum_{g=1}^{G} \nu\Sigma_{f,g}(\boldsymbol{r}) \int_{4\pi} \psi_g(\boldsymbol{r}, \hat{\Omega})\, d\Omega\end{aligned} \tag{2.10}$$

Notice that the multi-group cross sections are independent of incident angle. This is due to the assumed separability of the flux with respect to angular and energy distribution. This separability is not true strictly speaking and is a source of error in the multi-group approximation.

2.4.2 Angular Discretization

For deterministic methods in neutron transport, the angular variable is universally approximated. This is typically performed in one of two ways. The first way to approximate the angular variable is to expand it into moments of the spherical harmonics. Once the spherical harmonics expansion is applied, angular moments can be taken of the equation, with closure equations then the spherical harmonics expansion can become finite. We call these finite closed equations P_N methods, where N is the order of the expansion before closure. The simplest case, P_0, is also called the diffusion equation after closure. Typically, spherical harmonics work best when the angular dependence of the flux is low and the angular distribution is smooth. We call systems like this "diffusive".

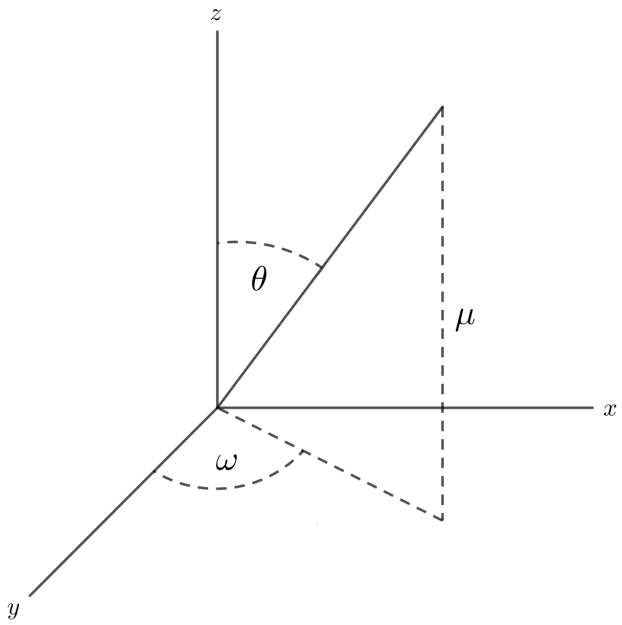

Figure 2.2: Angular Variables

For non-diffusive systems where the flux is expected to be highly anisotropic, the discrete ordinates approximation is used for the discretization of the angular variable. The discrete ordinates, or S_N methods, use an N^{th} order quadrature set to discretize the angular variable. While these discrete ordinates can introduce problems such as ray effects [45] in shielding and detection problems [46], work has been done to mitigate such problems [47] [48] and they rarely plague reactor systems, with the exception of fast reactors [49], due to the relatively small mean free path in LWRs.

Because the transport equation is typically written in terms of neutron energy and direction instead of velocity, the directional variable, $\hat{\Omega}$, has three terms but is only two dimensional in nature since it is a unit vector. It is commonly written as:

$$\hat{\Omega} = (\Omega_x, \Omega_y, \Omega_z) = (\sqrt{1-\mu^2}\cos\omega, \sqrt{1-\mu^2}\sin\omega, \mu) \tag{2.11}$$

Where μ is the polar cosine that ranges from -1 to 1 and ω is the azimuthal angle that ranges from 0 to 2π. The actual polar angle is θ that ranges from 0 to π so that $\cos\theta = \mu$. The unit circle coordinates are shown in Figure 2.2.

Now, a quadrature set is applied to discretize the angular directions. The two most commonly used quadrature types in neutron transport theory are the level symmetric quadratures [50] and the product quadratures [51]. Level symmetric quadratures, shown in Figure 2.3, uniformly distribute the discrete directions across the unit sphere and are rotationally invariant. This works well in systems that are closer to homogeneous without large discrepancies in directional variance. For

LWRs the variance in the axial direction is very different from the radial plane, so level-symmetric are not always the best choice.

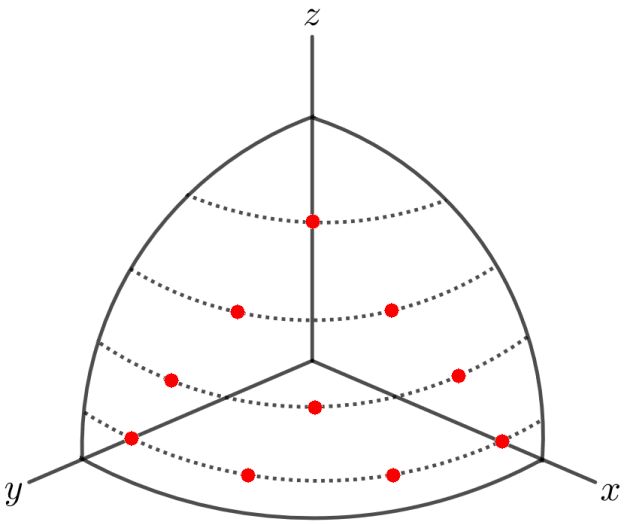

Figure 2.3: Level Symmetric Quadrature

For this work, and for most work done in MPACT, product quadratures are used due to the increased efficiency product quadrature sets provide in 2D MOC. In these quadrature sets the two angular variables are independently discretized so that the quadrature appears in axial layers and each axial layer has identical azimuthal components as the axial layer below it. This is illustrated in Figure 2.4, and has the additional benefit that the axial and azimuthal portions can be separated during computation and each variable can have its own method of discretization.

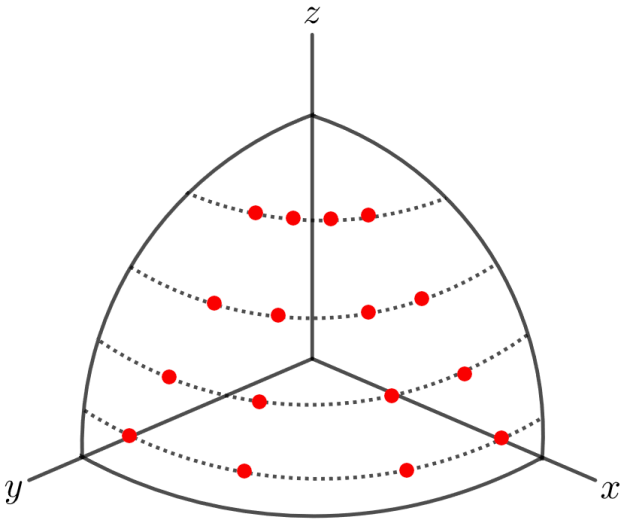

Figure 2.4: Product Quadrature

With the angular discretization chosen, our discrete angles are indexed $1 \leq m \leq M$ for an

angular quadrature set with M directions. This quadrature set will have angular weights w_m for each discrete angle:

$$\hat{\Omega}_m = (\Omega_{x,m}, \Omega_{y,m}, \Omega_{z,m}) = (\sqrt{1-\mu_m^2}\cos\omega_m, \sqrt{1-\mu_m^2}\sin\omega_m, \mu_m) \tag{2.12}$$

Introducing this into the multi-group equation, Eq. 2.10, we get the discrete ordinates multi-group equations:

$$\hat{\Omega}_m \cdot \boldsymbol{\nabla}\psi_{m,g}(\boldsymbol{r}) + \Sigma_{t,g}(\boldsymbol{r})\psi_{m,g}(\boldsymbol{r}) = \sum_{g=1}^{G}\sum_{m'=1}^{M}\Sigma_{s,m'\to m,g'\to g}(\boldsymbol{r})\psi_{m',g}(\boldsymbol{r})w_{m'} + \frac{\chi_g(\boldsymbol{r})}{k_{eff}4\pi}\sum_{g'=1}^{G}\nu\Sigma_{f,g}(\boldsymbol{r})\sum_{m'=1}^{M}\psi_{m',g}(\boldsymbol{r})w_{m'} \tag{2.13}$$

Anisotropic Scattering

The simplest scattering approximation for neutron transport problems is the approximation of isotropic scattering. This approximation assumes that scattering events with neutrons and isotopes have no angular dependence. In reality, neutron scattering is angularly dependent upon the scattering cosine angle, $\hat{\Omega}'\cdot\hat{\Omega}$. For LWR systems, the light elements present in the moderator lead to particularly anisotropic scattering, making some accounting for anisotropic scattering important.

In order to facilitate anisotropic scattering in discrete ordinates calculations, the scattering cross sections are typically expanded using Legendre polynomial moments of the scattering cosine:

$$\Sigma_s(E'\to E, \hat{\Omega}\cdot\hat{\Omega}') = \sum_{\ell=0}^{L}\Sigma_{s\ell}(E'\to E)P_\ell(\hat{\Omega}\cdot\hat{\Omega}') \tag{2.14}$$

Scattering approximated in this way is referred to as P_L scattering, where L is the order of the scattering Legendre polynomial cutoff, and it can be recognized that P_0 is then isotropic scattering. The Legendre components of the scattering cross sections are then defined as:

$$\Sigma_{s\ell}(E'\to E) = \frac{2\ell+1}{2}\int_{-1}^{1}\Sigma_s(E'\to E, \hat{\Omega}\cdot\hat{\Omega}')P_\ell(\hat{\Omega}\cdot\hat{\Omega}')\,d\mu \tag{2.15}$$

Now, Legendre polynomials of the cosine between two angles can actually be expressed as the sum of the real spherical harmonics functions, $R_\ell^r(\hat{\Omega})$ defined in [37], of those angles:

$$P_\ell(\hat{\Omega}\cdot\hat{\Omega}') = \sum_{r=-\ell}^{\ell}R_\ell^r(\hat{\Omega})R_\ell^r(\hat{\Omega}'); \quad \ell \geq 0 \tag{2.16}$$

So then applying the Legendre polynomial expansion of the scattering cross section to Equation 2.13, the scattering term becomes:

$$\sum_{g'=1}^{G}\sum_{m'=1}^{M}\Sigma_{s,m'\to m,g'\to g}(\boldsymbol{r})\psi_{m',g}(\boldsymbol{r})w_{m'} = \sum_{g'=1}^{G}\sum_{\ell=0}^{L}\Sigma_{s\ell,g'\to g}(\boldsymbol{r})\sum_{r=-\ell}^{\ell}R_\ell^r(\hat{\Omega}_m)\langle\psi_g(\boldsymbol{r})\rangle_\ell^r \tag{2.17}$$

Where $\langle\psi_g(\boldsymbol{r})\rangle_\ell^r$ are the spherical harmonic moments of the flux, defined as:

$$\langle\psi_g(\boldsymbol{r})\rangle_\ell^r = \sum_{m'=1}^{M}R_\ell^r(\hat{\Omega}_{m'})\psi_{m',g}(\boldsymbol{r})w_{m'} \tag{2.18}$$

Using this expansion instead of isotropic scattering can add significant extra time and memory to the computation due to the added requirement of computing and storing angular moments of the flux and source. Commonly, when some of the additional accuracy given by anisotropic scattering is desired, but computational capabilities are limited to isotropic scattering, the linear scattering cross section, Σ_{s1}, is subtracted from the total cross section to create what is called the transport cross section:

$$\Sigma_{tr,g} = \Sigma_{t,g} - \sum_{g'=1}^{G}\Sigma_{s1,g\to g'} \tag{2.19}$$

The form shown here is the out-scatter approximation for Σ_{tr}, though other approximations such as in-scatter and neutron leakage conservation are also used. This "transport cross section" is then used in place of the total cross section in the calculation, and isotropic P_0 expansion is still used for scattering computations. This method of scattering computation is called transport corrected P_0, or TCP_0.

2.4.3 Method of Characteristics

At this point the only part of phase-space still not discretized are the three locational variables. There are a variety of methods to discretize the spatial component of the transport equation including weighted diamond differencing techniques [40], finite element methods [52], and the *Method of Characteristics* (MOC) [53]. For this work, the method of spatial discretization will come in the form of the flat source approximation and constant cross section approximation applied to the MOC. Strictly speaking, MOC methods need not be limited to spatial variables, however because the only differential terms in the steady state NTE are spatial, it is only used for spatial variables here.

From the multi-group discrete ordinates equations, Eq. 2.13, we consider the advection gradient term and expand it.

$$\hat{\Omega}_m\cdot\boldsymbol{\nabla} = \Omega_{x,m}\frac{\partial}{\partial x} + \Omega_{y,m}\frac{\partial}{\partial y} + \Omega_{z,m}\frac{\partial}{\partial z} \tag{2.20}$$

Now we consider a discrete ray along the direction of a discrete angle. Let the distance along the ray be the variable s where $s = 0$ at the ray start point located for some arbitrary location along the ray at $\boldsymbol{r}_0 = (x_0, y_0, z_0)$. Then we can express any point $\boldsymbol{r} = (x, y, z)$ along the ray in terms of the starting location and distance along the ray:

$$\boldsymbol{r} = \boldsymbol{r}_0 + s\hat{\Omega}_m \tag{2.21}$$

Then we get the following relations for the partial derivatives of the spatial variables

$$x = x_0 + s\Omega_{x,m} \Rightarrow \frac{\partial x}{\partial s} = \Omega_{x,m} \tag{2.22a}$$

$$y = y_0 + s\Omega_{y,m} \Rightarrow \frac{\partial y}{\partial s} = \Omega_{y,m} \tag{2.22b}$$

$$z = z_0 + s\Omega_{z,m} \Rightarrow \frac{\partial z}{\partial s} = \Omega_{z,m} \tag{2.22c}$$

So then the gradient can be expressed as

$$\hat{\Omega}_m \cdot \boldsymbol{\nabla} = \frac{\partial x}{\partial s}\frac{\partial}{\partial x} + \frac{\partial y}{\partial s}\frac{\partial}{\partial y} + \frac{\partial z}{\partial s}\frac{\partial}{\partial z} = \frac{d}{ds} \tag{2.23}$$

this amounts to a change of variables from $(\boldsymbol{r}, \hat{\Omega})$ to s where s is the distance along the characteristic.

So then the discrete ordinates multi-group equation along the line can now be transformed from the original PDE transport equation into an ODE differential. This form of the MOC equations has a single independent variable, s:

$$\frac{d}{ds}\psi_{m,g}(s) + \Sigma_{t,g}(s)\psi_{m,g}(s) = \sum_{g=1}^{G}\sum_{m'=1}^{M}\Sigma_{s,m'\to m,g'\to g}(s)\psi_{m',g}(s)w_{m'} + \frac{\chi_g(s)}{k_{eff}4\pi}\sum_{g=1}^{G}\nu\Sigma_{f,g}(s)\sum_{m'=1}^{M}\psi_{m',g}(s)w_{m'} \tag{2.24}$$

Now because the scattering and fission operators are generally not analytically invertible functions, we cannot use a closed form integrating factor on the equation in its current form. However, neutron transport computations often make use of source iterations where the source is computed from the previous iteration and then treated as constant for the current iteration. So rewriting the equation for a constant source we get:

$$\frac{d}{ds}\psi_{m,g}(s) + \Sigma_{t,g}(s)\psi_{m,g}(s) = Q_{g,m}(s) \tag{2.25}$$

Then we change from s to s' and take an integrating factor to get

$$\frac{d}{ds'}\left[e^{\int_{s_0}^{s'}\Sigma_{t,g}(s'')\,ds''}\psi_{m,g}(s')\right] = e^{\int_{s_0}^{s'}\Sigma_{t,g}(s'')\,ds''}Q_{g,m}(s') \tag{2.26}$$

Which can be solved by integrating s' from s_0 to s to get the integral form of the 3D MOC equations:

$$\psi_{m,g}(s) = \psi_{m,g}(s_0)e^{-\int_{s_0}^{s}\Sigma_{t,g}(s'')\,ds''} + \int_{s_0}^{s} Q_{g,m}(s')e^{-\int_{s'}^{s}\Sigma_{t,g}(s'')\,ds''}\,ds' \tag{2.27}$$

2.4.4 Constant Cross Section and Flat Source Approximations

While the MOC allows us to express the solution as a set of functions along discrete characteristic rays, the continuous nature of these functions can still make it difficult to solve. We desire to instead transform Equation 2.27 into a set of coupled algebraic equations. To do this, the spatial domain must be discretized. This is done using the flat source approximation [54]. While higher order spatial approximations are sometimes used [55] [56], they are considered more advanced and will not be introduced into this work.

Consider a discrete set of subdivisions of the system volume indexed i. We then approximate these volume subdivisions as being constant in material. This then means that the volumes each have spatially constant material cross sections. If we divide our system in such a way that division boundaries do not cross material boundaries, then this becomes a very good approximation. In particular, for 0 power systems with fresh fuel, this approximation is very nearly exact. In situations of nonuniform depletion and material temperature gradients this approximation may become less accurate, however this can be mitigated with smaller subdivisions. This is the constant cross section approximation.

Consider these same volume subdivisions and approximate each volume as having spatially uniform source throughout. This spatially uniform source is the result of flux in the volume being cast as spatially uniform before source computation each iteration. Casting the flux as spatially flat throughout the subdivision before source calculation means that the induced fission and scattering source are necessarily spatially flat throughout the volume. This is the flat source approximation. We call each of these subdivision a *Flat Source Region* (FSR).

Now consider again the integral form of the MOC equations established in Eq. 2.27. If we let $s_0 = s_{in}$ be the position where the characteristic ray enters the subdivision and $s = s_{out}$ be the position where the ray exits the region, then we can get the following equation for the segment exit

flux along the characteristic ray, where the segment length is $\Delta s = s_{in} - s_{out}$.

$$\psi_{m,g,out} = \psi_{m,g,in} e^{-\Delta s \Sigma_{t,i,g}} + \frac{Q_{i,g,m}}{\Sigma_{t,i,g}} \left(1 - e^{-\Delta s \Sigma_{t,i,g}}\right) \tag{2.28}$$

We can also integrate Eq. 2.27 over the segment length to get the segment integrated flux:

$$\psi_{m,g,int} = \frac{1}{\Sigma_{t,i,g}} (\psi_{m,g,in} - \psi_{m,g,out} + Q_{i,g,m} \Delta s) \tag{2.29}$$

Then each characteristic ray can be followed along the domain of the system, solving for the segment exiting flux at each intersection and accumulating segment integrated flux to compute the volume integrated flux in the FSRs. Notice that FSRs need not be convex, in fact a single ray may have many segments in the same FSR for concave FSRs.

2.5 Deterministic Solution Methods

With the FSR approximation applied to the multi-group discrete ordinates transport equation in Eq. 2.27, a large number of characteristic rays can be traced along the volume. With these rays traced across the domain, the problem reduces to an algebraic system of equations. Strictly speaking, this makes the problem now an invertible matrix-vector equation. However, the matrix is far too complex and large to construct, so iterative methods are necessary to solve the system. The most common iterative method for solving this form of the transport equation is called source iterations, and it is almost universally accelerated since convergence can sometimes be quite slow.

2.5.1 Source Iterations

Deterministic neutron transport calculations using MOC are necessarily iterative due to the size and complexity of the algebraic set of equations [57]. The most common method for iteratively solving this system is called the source iterations method. This method treats the source in the system as fixed, and solves the fixed source MOC problem. With this new solution, the fixed source is updated for the next iteration. Eventually, the iterative change to the source is small enough that the method is said to have converged.

We also iteratively compute the eigenvalue k_{eff} for iteration l using the updated fission source from each iteration.

$$k_{eff}^{l} = \frac{\sum_i \sum_{g=1}^{G} \nu\Sigma_{f,i,g} \sum_{m=1}^{M} \psi_{i,m,g}^{l} w_m}{\sum_i \sum_{g=1}^{G} \nu\Sigma_{f,i,g} \sum_{m=1}^{M} \psi_{i,m,g}^{l-1} w_m} \tag{2.30}$$

Algorithm 2.1 Source Iteration Solution to the Transport Equation

1: $l = 0$
2: **while** $|k_{eff}^{l} - k_{eff}^{l-1}| \geq \epsilon_k$ & $\|\psi^{l} - \psi^{l-1}\| \geq \epsilon_\psi$ **do**
3: $l = l + 1$
4: Compute Eq. 2.28 to traverse each ray using Q^{l-1}
5: Evaluate Eq. 2.29 and accumulate FSR integrated flux during traversal to get ψ^{l}
6: Evaluate Eq. 2.30 to get k_{eff}^{l}
7: Compute new source Q^{l}
8: **end while**

2.5.2 Coarse Mesh Finite Difference Acceleration

The source iteration method described in Algorithm 2.1 is valid and generally effective at iteratively converging the solution to the multi-group discrete ordinates MOC form of the transport equation with flat source approximations. However, this process can sometimes take a prohibitively large number of iterations, sometimes requiring hundreds if not thousands of iterations. To reduce the time spent solving the system, we often attempt acceleration of the solution through the use of low order methods [58] [59] [60]. These methods can improve the convergence of the system, often bringing the number of iterations down from $O(1000)$ to $O(10)$. Typically, the computational costs added per iteration from solving the low order equations are quite minor. This makes the usage of low-order acceleration schemes effective in more quickly solving large systems using modern computational capabilities.

Of these low-order acceleration schemes, perhaps the most commonly used acceleration method for solving the NTE for reactors is the CMFD scheme [59]. This method of acceleration makes use of a diffusion equation on a coarse mesh with corrections to the diffusion coefficient to preserve current between cells using the MOC computed fine mesh flux. CMFD also uses homogenized cross sections in the coarse cells made using the computed fine mesh scalar flux from the MOC calculation. This then leaves a coarse mesh diffusion equation that has been corrected by both the angular dependence, as well as the fine mesh variance from the flux of the previous source iteration. This diffusion equation is then solved for the given iteration parameters and the solution is projected back onto the fine mesh such that the fine mesh data is scaled by the CMFD solution. This leads to converged solutions with CMFD acceleration being necessarily exact to solutions converged with pure source iterations, due to the equivalence of the corrected diffusion equation at each iteration.

The CMFD equations starts with the P_0 equation, that is to say the 0^{th} angular moment of the transport equation integrated over a coarse cell. At this point the equation is still exact in comparison

to the transport equation, but is not closed.

$$\sum_s J^{net}_{j,g,s} A_{j,s} + \Sigma_{t,j,g}\phi_{j,g}V_j = \sum_{g'=1}^{G}\left(\Sigma_{s0,j,g'\to g} + \frac{\chi_{j,g}}{k_{eff}}\nu\Sigma_{f,j,g'}\right)\phi_{j,g'} \tag{2.31}$$

Where $A_{j,s}$ is the area of the surface s and V_j is the volume of cell j. The equation is then closed using Fick's law with finite-difference spatial discretization for the first angular moment, the current J, using the diffusion coefficient.

$$J^{net}_{j,g,s} = -\tilde{D}_{j,g,s}(\phi_{j,g,s} - \phi_{j,g,s}) \tag{2.32}$$

The diffusion coefficient here then takes the form of:

$$D_{j,g} = \frac{1}{3\Sigma_{tr,j,g}} \tag{2.33a}$$

$$\tilde{D}_{j,g,s} = \frac{2D_{j,g}D_{j_s,g}}{h_{j,s}\left(D_{j,g} + D_{j_s,g}\right)} \tag{2.33b}$$

However this approximation does not preserve current that would be computed in the actual transport problem. This closed approximation can introduce error relative to transport since it is not exact compared to the spatially discretized MOC equations unless the current is computed in a such a way to match the transport equation and the cross sections are collapsed to preserve the spatial distribution of the flux in the fine cells.

Instead, CMFD uses a corrected diffusion coefficient to preserve the net current across the coarse cells. Using the iterative transport net current on surface s, the corrective diffusion coefficient, $\hat{D}$, is defined as:

$$\hat{D}^{l-1/2}_{j,g,s} = \frac{J^{net,l-1/2}_{j,g,s} + \tilde{D}_{j,g,s}(\phi^{l-1/2}_{j,g} - \phi^{l-1/2}_{j,g,s})}{\phi^{l-1/2}_{j,g} - \phi^{l-1/2}_{j,g,s}} \tag{2.34}$$

Where j_s is the index of the coarse cell bordering cell j across surface s, $h_{j,s}$ is the distance between cell j and j_s across s, and $\Sigma_{tr} = \Sigma_t - \Sigma_{s1}$, or just Σ_t if P0 scattering is used. This correction coefficient then makes it so that the new definition, below, of net current in CMFD preserves equivalence between the fine mesh MOC equations and CMFD at convergence.

$$J^{net}_{j,g,s} = -\tilde{D}_{j,g,s}(\phi_{j,g,s} - \phi_{j,g,s}) + \hat{D}^{l}_{j,g,s}(\phi_{j,g} + \phi_{j,g,s}) \tag{2.35}$$

With this correction in place, homogenization of the coarse cell cross sections must also be defined in terms of the fine mesh transport solution. The cross sections, fission spectrum, and scalar

flux for coarse cell j is computed after source iteration $l-1$ from the fine mesh values as:

$$\phi_{j,g}^{l-1/2} = \frac{\sum_{i \in j} \phi_{i,g}^{l-1/2} V_i}{\sum_{i \in j} V_i} \tag{2.36a}$$

$$\Sigma_{x,j,g}^{l-1/2} = \frac{\sum_{i \in j} \Sigma_{x,i,g} \phi_{i,g}^{l-1/2} V_i}{\sum_{i \in j} \phi_{i,g}^{l-1/2} V_i} \tag{2.36b}$$

$$\chi_{j,g}^{l-1/2} = \frac{\sum_{i \in j} \chi_{i,g} \sum_{g'=1}^{G} \nu\Sigma_{f,i,g'} \phi_{i,g'}^{l-1/2} V_i}{\sum_{i \in j} \sum_{g'=1}^{G} \nu\Sigma_{f,i,g'} \phi_{i,g'}^{l-1/2} V_i} \tag{2.36c}$$

In order for the changes from CMFD to be reflected in the transport sweeps, the solution is projected back onto the fine mesh flux before sources are computed.

$$\phi_{i,g}^{l} = \phi_{i,g}^{l-1/2} \frac{\phi_{j,g}^{l}}{\phi_{j,g}^{l-1/2}}, \; i \in j \tag{2.37}$$

These new definitions of the net current and the coarse cell homogenized cross sections preserve both the fine mesh spatial discretization and the angular variance of the MOC equation at convergence. As such, CMFD accelerated neutron transport will converge to the exact same solution as pure source iterations, but typically much faster.

With CMFD fully defined and consistent with neutron transport in convergence, Algorithm 2.1 is now modified to include CMFD acceleration:

Algorithm 2.2 CFMD Accelerated Source Iterations

1: $l = 0$
2: **while** $|k_{eff}^{l} - k_{eff}^{l-1}| \geq \epsilon_k$ & $\|\psi^{l+1/2} - \psi^{l-1/2}\| \geq \epsilon_\psi$ **do**
3: $l = l + 1$
4: Compute cell-averaged values for CMFD coefficients from Eqs. 2.36 and 2.34 using $\phi_{i,g}^{l-1/2}$
5: Solve Eq. 2.31 for $\phi_{j,g}^{l}$
6: Project CMFD flux back onto the fine mesh with Eq. 2.37 using $\phi_{j,g}^{l}$ and $\phi_{j,g}^{l-1/2}$
7: Compute new source Q^l
8: Compute Eq. 2.28 to traverse each ray using Q^l
9: Evaluate Eq. 2.29 and accumulate FSR integrated flux during traversal to get $\psi^{l+1/2}$
10: Evaluate Eq. 2.30 to get k_{eff}^{l}
11: **end while**

2.6 Review of 2D/1D Methods For Neutron Transport

2D/1D methods in general split the transport equation into two separate equations. One for the radial part and one for the axial part of the equations. Now to begin this discussion, start with the 3D Boltzmann transport equation

$$\mathbf{L}\psi(\boldsymbol{r},\hat{\Omega},E)=\mathbf{S}\psi(\boldsymbol{r},\hat{\Omega},E) \tag{2.38}$$

The radial loss operator is then defined as:

$$\mathbf{L}_R\psi_R(\boldsymbol{r},\hat{\Omega},E)=\Omega_x\frac{\partial}{\partial x}\psi_R(\boldsymbol{r},\hat{\Omega},E)+\Omega_y\frac{\partial}{\partial y}\psi_R(\boldsymbol{r},\hat{\Omega},E)+\Sigma_t(\boldsymbol{r},E)\psi_R(\boldsymbol{r},\hat{\Omega},E) \tag{2.39a}$$

So that the transport equation for the radial problem is:

$$\mathbf{L}_R\psi_R(\boldsymbol{r},\hat{\Omega},E)=\mathbf{S}\psi_R(\boldsymbol{r},\hat{\Omega},E)-\Omega_z\frac{\partial}{\partial z}\psi_Z(\boldsymbol{r},\hat{\Omega},E) \tag{2.39b}$$

$$\begin{gathered}\psi_R(\boldsymbol{r},\hat{\Omega},E)=\Gamma_R(\boldsymbol{r},\hat{\Omega},E),\\ \boldsymbol{r}\in\partial V,\quad \hat{\Omega}\cdot\hat{n}<0\end{gathered} \tag{2.39c}$$

The axial loss operator is then

$$\mathbf{L}_Z\psi_Z(\boldsymbol{r},\hat{\Omega},E)=\Omega_z\frac{\partial}{\partial z}\psi_Z(\boldsymbol{r},\hat{\Omega},E)+\Sigma_t(\boldsymbol{r},E)\psi_Z(\boldsymbol{r},\hat{\Omega},E) \tag{2.40a}$$

So that the transport equation for the axial problem is is:

$$\mathbf{L}_Z\psi_Z(\boldsymbol{r},\hat{\Omega},E)=\mathbf{S}\psi_Z(\boldsymbol{r},\hat{\Omega},E))-\Omega_x\frac{\partial}{\partial x}\psi_R(\boldsymbol{r},\hat{\Omega},E)-\Omega_y\frac{\partial}{\partial y}\psi_R(\boldsymbol{r},\hat{\Omega},E) \tag{2.40b}$$

$$\begin{gathered}\psi_Z(\boldsymbol{r},\hat{\Omega},E)=\Gamma_Z(\boldsymbol{r},\hat{\Omega},E),\\ \boldsymbol{r}\in\partial V,\quad \hat{\Omega}\cdot\hat{n}<0\end{gathered} \tag{2.40c}$$

Now notice that since we have yet to introduce any approximations, we still have equivalence among all transport equations:

$$\psi_R(\boldsymbol{r},\hat{\Omega},E)=\psi_Z(\boldsymbol{r},\hat{\Omega},E)=\psi(\boldsymbol{r},\hat{\Omega},E) \tag{2.41a}$$

$$\Gamma_Z(\boldsymbol{r},\hat{\Omega},E)=\Gamma_R(\boldsymbol{r},\hat{\Omega},E)=\Gamma(\boldsymbol{r},\hat{\Omega},E) \tag{2.41b}$$

We now define a set of axial coordinates $0=z_{1/2}<z_{3/2}<\cdots<z_{K-1/2}<z_{K+1/2}=Z_{max}$,

so that $\Delta z_k = z_{k+1/2} - z_{k-1/2}$. Then if we average the values in the radial equation from $z_{k-1/2}$ to $z_{k+1/2}$ for $k = 1, 2, \ldots, K$, we get K equations for each axial slice:

$$\mathbf{L}_{R,k}\psi_{R,k}(x, y, \hat{\Omega}, E) = \mathbf{S}_k\psi_{R,k}(x, y, \hat{\Omega}, E) + Q_{TL,k}(x, y, \hat{\Omega}, E) \tag{2.42a}$$

$$\begin{aligned} \psi_{R,k}(x, y, \hat{\Omega}, E) &= \Gamma_{R,k}(x, y, \hat{\Omega}, E), \\ (x, y) \in \partial V_R(x, y), &\quad \hat{\Omega} \cdot \hat{n} < 0 \end{aligned} \tag{2.42b}$$

Where

$$\psi_{R,k}(x, y, \hat{\Omega}, E) = \frac{1}{\Delta z_k} \int_{z_{k-1/2}}^{z_{k+1/2}} \psi_R(\boldsymbol{r}, \hat{\Omega}, E)\, dz \tag{2.43a}$$

$$\Gamma_{R,k}(x, y, \hat{\Omega}, E) = \frac{1}{\Delta z_k} \int_{z_{k-1/2}}^{z_{k+1/2}} \Gamma_R(\boldsymbol{r}, \hat{\Omega}, E)\, dz \tag{2.43b}$$

$$\begin{aligned} Q_{TL,k}(x, y, \hat{\Omega}, E) &= -\frac{1}{\Delta z_k} \int_{z_{k-1/2}}^{z_{k+1/2}} \Omega_z \frac{\partial}{\partial z}\psi_Z(\boldsymbol{r}, \hat{\Omega}, E)\, dz \\ &= \frac{\Omega_z}{\Delta z_k} \Big(\psi_Z(x, y, z_{k-1/2}, \hat{\Omega}, E) - \psi_Z(x, y, z_{k+1/2}, \hat{\Omega}, E)\Big) \end{aligned} \tag{2.43c}$$

$$\begin{aligned} \mathbf{S}_k\psi_{R,k}(x, y, \hat{\Omega}, E) = &\int_{4\pi}\int_0^\infty \Sigma_{s,k}(x, y, \hat{\Omega} \cdot \hat{\Omega}', E' \to E)\psi_{R,k}(x, y, \hat{\Omega}', E')\, dE'\, d\Omega' \\ &+ \frac{\chi(E)}{4\pi} \int_{4\pi}\int_0^\infty \nu\Sigma_{f,k}(x, y, E')\psi_{R,k}(x, y, \hat{\Omega}', E')\, dE'\, d\Omega' \end{aligned} \tag{2.43d}$$

$$\begin{aligned} \mathbf{L}_{R,k}\psi_{R,k}(x, y, \hat{\Omega}, E) = \Omega_x \frac{\partial}{\partial x}\psi_{R,k}(x, y, \hat{\Omega}, E) + \Omega_y \frac{\partial}{\partial y}\psi_{R,k}(x, y, \hat{\Omega}, E) \\ + \Sigma_{t,k}(x, y, E)\psi_{R,k}(x, y, \hat{\Omega}, E) \end{aligned} \tag{2.43e}$$

$$\Sigma_{s,k}(x, y, \hat{\Omega} \cdot \hat{\Omega}', E' \to E) = \frac{\int_{z-1/2}^{z+1/2} \Sigma_s(\boldsymbol{r}, \hat{\Omega} \cdot \hat{\Omega}', E' \to E)\psi_R(\boldsymbol{r}, \hat{\Omega}', E')\, dz}{\Delta z_k \psi_{R,k}(x, y, \hat{\Omega}', E')} \tag{2.43f}$$

$$\nu\Sigma_{f,k}(x, y, E') = \frac{\int_{z-1/2}^{z+1/2} \nu\Sigma_f(\boldsymbol{r}, E') \left(\int_{4\pi} \psi_R(\boldsymbol{r}, \hat{\Omega}', E')\, d\Omega'\right) dz}{\Delta z_k \int_{4\pi} \psi_{R,k}(x, y, \hat{\Omega}', E')\, d\Omega'} \tag{2.43g}$$

$$\Sigma_{t,k}(x, y, E) = \frac{\int_{z-1/2}^{z+1/2} \Sigma_t(\boldsymbol{r}, E) \left(\int_{4\pi} \psi_R(\boldsymbol{r}, \hat{\Omega}, E)\, d\Omega\right) dz}{\Delta z_k \int_{4\pi} \psi_{R,k}(x, y, \hat{\Omega}, E)\, d\Omega} \tag{2.43h}$$

Note that thus far no approximations other than the initial assumptions have been made. Now, given

an approximation for the transverse leakage source, $Q_{TL,k}(x, y, \hat{\Omega}, E)$, then each of these axial slice equations can be solved for $\psi_{R,k}(x, y, \hat{\Omega}, E)$ with any desired 2D method. Normally these equations are solved using 2D MOC methods with multi-group approximations. So the question is how to best approximate the transverse leakage source. This then is one of the key differences between the various traditional 2D/1D methods. Another difference is the homogenization in the radial direction.

2.6.1 MPACT

In MPACT [61] the axial flux terms are discretized over the pin cell j. So the transverse leakage term takes on the form:

$$Q_{TL,k,j}(\hat{\Omega}, E) = \frac{\Omega_z}{\Delta z_k}\left(\psi_{Z,j}(z_{k-1/2}, \hat{\Omega}, E) - \psi_{Z,j}(z_{k+1/2}, \hat{\Omega}, E)\right) \tag{2.44}$$

The original (and default) 2D/1D implementation in MPACT assumed an isotropic TL. This is equivalent to averaging the leakage term over all angles:

$$Q_{TL,k,j}(\hat{\Omega}, E) = \frac{1}{4\pi\Delta z_k}\left[J_{z,k-1/2,j}(E) - J_{z,k+1/2,j}(E)\right] \tag{2.45}$$

To solve for this leakage, the axial equations must be transformed into a new 1D problem. To do this the axial transport equation, Eq. 2.40, is radially averaged over the pin cell j:

$$\begin{aligned}\frac{1}{\partial V_j}\int_{\partial V_j}\mathbf{L}_Z\psi_Z(\boldsymbol{r}, \hat{\Omega}, E)dxdy = \frac{1}{\partial V_j}\int_{\partial V_j}\mathbf{S}\psi_Z(\boldsymbol{r}, \hat{\Omega}, E)dxdy \\ - \frac{1}{\partial V_j}\int_{\partial V_j}\Omega_x\frac{\partial}{\partial x}\psi_R(\boldsymbol{r}, \hat{\Omega}, E)dxdy - \frac{1}{\partial V_j}\int_{\partial V_j}\Omega_y\frac{\partial}{\partial y}\psi_R(\boldsymbol{r}, \hat{\Omega}, E)dxdy\end{aligned} \tag{2.46}$$

Which gives:

$$\mathbf{L}_{Z,j}\psi_{Z,j}(z, \hat{\Omega}, E) = \mathbf{S}_j\psi_{Z,j}(z, \hat{\Omega}, E) + Q_{RL}(z, \hat{\Omega}, E) \tag{2.47a}$$

$$\begin{aligned}\psi_{Z,j}(z, \hat{\Omega}, E) = \Gamma_{Z,k}(z, \hat{\Omega}, E), \\ (z) \in \partial[0, Z], \quad \hat{\Omega}\cdot\hat{n} < 0\end{aligned} \tag{2.47b}$$

In the original 2D/1D implementation in MPACT, the total cross section Σ_t was assumed to be isotropic as was the axial source. Additionally, the radial transverse leakage is isotropized so that

the radial leakage becomes:

$$\begin{aligned} Q_{RL}(z,\hat{\Omega},E) &\approx -\frac{1}{\partial V_j}\int_{\partial V_j}\frac{1}{4\pi}\int_{4\pi}\left(\Omega_x\frac{\partial}{\partial x}+\Omega_y\frac{\partial}{\partial y}\right)\psi_R(\boldsymbol{r},\hat{\Omega},E)\,d\Omega\,dxdy \\ &= -\frac{1}{\partial V_j}\int_{\partial V_j}\frac{1}{4\pi}\left(\frac{\partial}{\partial x}J_x(\boldsymbol{r},E)+\frac{\partial}{\partial y}J_y(\boldsymbol{r},E)\right)\,dxdy \\ &= \frac{1}{4\pi}\left(J_{x-,j}(z,E)-J_{x+,j}(z,E)+J_{y-,j}(z,E)-J_{y+,j}(z,E)\right)\,dxdy \end{aligned} \quad (2.48)$$

where

$$J_x(\boldsymbol{r},E)=\int_{4\pi}\Omega_x\psi_R(\boldsymbol{r},\hat{\Omega},E)\,d\Omega \quad (2.49)$$

Making the 1D axial equation now

$$\Omega_z\frac{\partial}{\partial z}\psi_{Z,j}(z,\hat{\Omega},E)+\Sigma_{t,Z,j}(z,E)\psi_{Z,j}(z,\hat{\Omega},E)=\frac{1}{4\pi}\left(Q_j(z,E)-\sum_{s=N,S,E,W}J_{j,s}(z,E)\right) \quad (2.50)$$

where

$$Q_j(z,E)=\frac{1}{4\pi}\int_{4\pi}\mathbf{S}_j\psi_{Z,j}(z,\hat{\Omega},E)\,d\Omega \quad (2.51)$$

Then Eq. 2.50 is a 1D transport equation for $\psi_{Z,j}$ that can be solved using 1D P_N. This solution then is fed back into the radial equations in terms of the axial transverse leakage in Eq. 2.43c. In MPACT this is solved using a nodal expansion method with quadratic spatial expansion of the source and quartic expansion of the flux.

This constitutes the basis for 2D/1D in MPACT, however, Stimpson built upon this method by introducing azimuthal expansion of the transverse leakage [25]. To do this, the axial and radial transverse leakage were treated with a Fourier expansion. This is sufficiently accurate in comparison to maintaining full azimuthal dependence for the anisotropic TL and saves significant amounts of memory, while still benefiting from the increased accuracy of some angular dependence. The 1D axial angular flux with Fourier expansion in the azimuthal directional variable ω is:

$$\psi_{Z,j}(z,\omega,\mu,E)=\frac{\psi_{Z,0,j}(z,\mu,E)}{2\pi}+\frac{1}{\pi}\sum_{p=1}^{P}\left[\psi_{Z,c,p,j}(z,\mu,E)\cos(p\omega)+\psi_{Z,s,p,j}(z,\mu,E)\sin(p\omega)\right] \quad (2.52)$$

Each azimuthal moment, $\psi_{Z,c,p,j}$ and $\psi_{Z,s,p,j}$, is then solved by a separate 1D transport equation using a P_N method. Typically this is done using P_2 solutions since Stimpson showed this obtains solutions close to explicit angular dependence. Inserting this expansion into Eq. 2.50 we get the

new 1D equation

$$\mu\frac{\partial}{\partial z}\left(\frac{\psi_{Z,0,j}(z,\mu,E)}{2\pi}+\frac{1}{\pi}\sum_{p=1}^{P}\left[\psi_{Z,c,p,j}(z,\mu,E)\cos(p\omega)+\psi_{Z,s,p,j}(z,\mu,E)\sin(p\omega)\right]\right)$$
$$+\Sigma_{t,Z,j}(z,E)\left(\frac{\psi_{Z,0,j}(z,\mu,E)}{2\pi}+\frac{1}{\pi}\sum_{p=1}^{P}\left[\psi_{Z,c,p,j}(z,\mu,E)\cos(p\omega)+\psi_{Z,s,p,j}(z,\mu,E)\sin(p\omega)\right]\right)$$
$$=\frac{Q_j(z,E)}{4\pi}+\tilde{Q}_{RL}(z,\mu,\omega,E) \quad (2.53)$$

where the radial transverse leakage is shortened as:

$$\tilde{Q}_{RL}(z,\mu,\omega,E)=-\frac{TL_{R,0,j}(z,\mu,E)}{2\pi}$$
$$-\frac{1}{\pi}\sum_{p=1}^{P}\left[TL_{R,c,p,j}(z,\mu,E)\cos(p\omega)+TL_{R,s,p,j}(z,\mu,E)\sin(p\omega)\right] \quad (2.54)$$

and the expansion is also introduced into the radial transverse leakage terms:

$$TL_{R,0,j}(z,\mu,E)=\frac{1}{\partial V_j}\sum_{s=N,S,E,W}\int_{\partial V_j}\int_0^{2\pi}(\hat{\Omega}\cdot\hat{n}_s)\psi_R(\boldsymbol{r},\hat{\Omega},E)\,d\omega\,dxdy \quad (2.55a)$$

$$TL_{R,c,p,j}(z,\mu,E)=\frac{1}{\partial V_j 2\pi}\sum_{s=N,S,E,W}\int_{\partial V_j}\int_0^{2\pi}\cos(p\omega)(\hat{\Omega}\cdot\hat{n}_s)\psi_R(\boldsymbol{r},\hat{\Omega},E)\,d\omega\,dxdy \quad (2.55b)$$

$$TL_{R,s,p,j}(z,\mu,E)=\frac{1}{\partial V_j 2\pi}\sum_{s=N,S,E,W}\int_{\partial V_j}\int_0^{2\pi}\sin(p\omega)(\hat{\Omega}\cdot\hat{n}_s)\psi_R(\boldsymbol{r},\hat{\Omega},E)\,d\omega\,dxdy \quad (2.55c)$$

These equations have P sine and cosine and taking the moments. As such, to form them in solvable algebraic terms, the first P cosine and sine of μ moments of these equations will be taken to yield:

$$\left(\mu\frac{\partial}{\partial z}+\Sigma_{t,Z,j}(z,E)\right)\psi_{Z,0,j}(z,\mu,E)=\frac{Q_j(z,E)}{2}-TL_{R,0,j}(z,\mu,E) \quad (2.56a)$$

$$\left(\mu\frac{\partial}{\partial z}+\Sigma_{t,Z,j}(z,E)\right)\psi_{Z,c,p,j}(z,\mu,E)=-TL_{R,c,p,j}(z,\mu,E) \quad (2.56b)$$

$$\left(\mu\frac{\partial}{\partial z}+\Sigma_{t,Z,j}(z,E)\right)\psi_{Z,s,p,j}(z,\mu,E)=-TL_{R,s,p,j}(z,\mu,E) \quad (2.56c)$$

Stimpson demonstrated substantial improvement over isotropic calculations using this method.

Following up on this work, Jarrett extended this formulation to include polar angle expansion using Legendre polynomials, as well as angular dependence in cross sections [26]. The angular dependence for cross sections was originally considered for both the azimuthal and polar angles, however, Jarrett showed that the error introduced by azimuthal homogenization for cross sections was minimal [26]. Hence only polar angle dependence of cross sections are considered. Then in the preceding equations $\Sigma_{t,Z,j}(z,E)$ becomes $\tilde{\Sigma}_{t,Z,j}(z,\mu,E))$ and is homogenized as:

$$\tilde{\Sigma}_{t,Z,j}(z,\mu,E) = \frac{\int_{\partial V_j} \Sigma_t(\boldsymbol{r},E) \int_0^{2\pi} \psi_R(\boldsymbol{r},\hat{\Omega},E)\, d\omega\, dxdy}{\int_{\partial V_j} \int_0^{2\pi} \psi_R(\boldsymbol{r},\hat{\Omega},E)\, d\omega\, dxdy} \tag{2.57}$$

Jarrett found that when using Legendre polynomial expansions for the polar variable, it was often sufficient to truncate at $L = 3$ moments [26]. To do this both the angular flux and transverse leakage sources were expanded in Legendre polynomials and the anisotropic component of the cross section was collected with the source anisotropy and multiplied by the radial flux. This gives the following equation:

$$\begin{aligned}
&\mu\frac{\partial}{\partial z}\left(\frac{\psi_{Z,0,j}(z,\mu,E)}{2\pi} + \frac{1}{\pi}\sum_{p=1}^{P}\left[\psi_{Z,c,p,j}(z,\mu,E)\cos(p\omega) + \psi_{Z,s,p,j}(z,\mu,E)\sin(p\omega)\right]\right) \\
&+ \Sigma_{t,Z,j}(z,E)\left(\frac{\psi_{Z,0,j}(z,\mu,E)}{2\pi} + \frac{1}{\pi}\sum_{p=1}^{P}\left[\psi_{Z,c,p,j}(z,\mu,E)\cos(p\omega) + \psi_{Z,s,p,j}(z,\mu,E)\sin(p\omega)\right]\right) \\
&\qquad = \frac{Q_j(z,E)}{4\pi} + \tilde{Q}_{RL}(z,\mu,\omega,E) \\
&\qquad + \left[\Sigma_{t,Z,j}(z,E) - \tilde{\Sigma}_{t,Z,j}(z,\mu,E)\right]\left(\frac{\psi_{R,0,j}(z,\mu,E)}{2\pi}\right. \\
&\qquad \left. + \frac{1}{\pi}\sum_{p=1}^{P}\left[\psi_{R,c,p,j}(z,\mu,E)\cos(p\omega) + \psi_{R,s,p,j}(z,\mu,E)\sin(p\omega)\right]\right)
\end{aligned} \tag{2.58}$$

Jarrett noted that the anisotropic azimuthal moments and anisotropic azimuthal angular fluxes were small terms and their products could be safely be ignored in LWR problems [26]. So then using a Legendre expansion in the polar angle μ, Eq. 2.56 with polar dependent cross sections for the zeroth azimuthal moment becomes:

$$\frac{\partial}{\partial z}\phi_{Z,1,j}(z,E) + \Sigma_{t,Z,j}(z,E)\phi_{Z,0,j}(z,E) = q_{0,j}(z,E) \tag{2.59a}$$

$$\frac{1}{3}\frac{\partial}{\partial z}\phi_{Z,0,j}(z,E) + \frac{2}{3}\frac{\partial}{\partial z}\phi_{Z,2,j}(z,E) + \Sigma_{t,Z,j}(z,E)\phi_{Z,1,j}(z,E) = q_{1,j}(z,E) \tag{2.59b}$$

$$\frac{2}{5}\frac{\partial}{\partial z}\phi_{Z,1,j}(z,E)+\frac{3}{5}\frac{\partial}{\partial z}\phi_{Z,3,j}(z,E)+\Sigma_{t,Z,j}(z,E)\phi_{Z,2,j}(z,E)=q_{2,j}(z,E) \tag{2.59c}$$

$$\frac{3}{7}\frac{\partial}{\partial z}\phi_{Z,2,j}(z,E)+\Sigma_{t,Z,j}(z,E)\phi_{Z,3,j}(z,E)=q_{3,j}(z,E) \tag{2.59d}$$

where:

$$q_{l,j}(z,E)=\int_{-1}^{1}P_l(\mu)\Bigg(\frac{Q_j(z,E)}{2}-TL_{R,0,j}(z,\mu,E) + \left[\Sigma_{t,Z,j}(z,E)-\tilde{\Sigma}_{t,Z,j}(z,\mu,E)\right]\psi_{R,0,j}(z,\mu,E)\Bigg)\,d\mu \tag{2.60}$$

This then is the most advanced form of traditional 2D/1D present in MPACT, with anisotropic polar dependent cross sections, Fourier azimuthal expansion, and Legendre polynomial polar expansion for the transverse leakage.

2.6.2 DeCART and nTRACER

DeCART [21] and nTRACER [22] essentially perform 2D/1D in much the same manner as the original implementation in MPACT. They approximate the transverse leakage source by first integrating the term over all angle and dividing by 4π so that it is isotropic:

$$Q_{TL,k}^{\text{DeCART}}(x,y,\hat{\Omega},E)\approx\frac{1}{4\pi}\int_{4\pi}Q_{TL,k}(x,y,\hat{\Omega},E)\,d\Omega=\frac{1}{4\pi\Delta z_k}\int_{z_{k+1/2}}^{z_{k-1/2}}\frac{\partial}{\partial z}J_z(\boldsymbol{r},E)\,dz$$
$$=\frac{1}{4\pi\Delta z_k}\left[J_{z,k-1/2}(x,y,E)-J_{z,k+1/2}(x,y,E)\right] \tag{2.61a}$$

where

$$J_{z,k+1/2}(x,y,E)=\int_{4\pi}\Omega_z\psi_Z(x,y,z_{k+1/2},\hat{\Omega},E)\,d\Omega \tag{2.61b}$$

They then approximate the axial current term using Fick's law as:

$$J_{z,k+1/2}(x,y,E)\approx-D_{k+1/2}(x,y,E)\frac{\phi_{k+1}(x,y,E)-\phi_k(x,y,E)}{\Delta z_{k+1/2}} \tag{2.62a}$$

where

$$\phi_k(x,y,E)=\int_{4\pi}\Psi_{R,k}(x,y,\hat{\Omega},E)\,d\Omega \tag{2.62b}$$

$$\Delta z_{k+1/2}=\frac{1}{2}(\Delta z_{k+1}+\Delta z_k) \tag{2.62c}$$

$$D_{k+1/2}(x,y,E)=\frac{\Delta z_{k+1}+\Delta z_k}{3\Sigma_{tr,k+1}(x,y,E)\Delta z_{k+1}+\Sigma_{tr,k}(x,y,E)\Delta z_k} \tag{2.62d}$$

where $\Sigma_{tr,k}$ can be estimated for the slice in any manner desired (though how it is defined will affect the error of the solution), and can potentially just be set to $\Sigma_{t,k}$. Here $\Psi_{R,k}(x, y, \hat{\Omega}, E)$ are the solutions for the new radial equations:

$$\mathbf{L}_{R,k}\Psi_{R,k}(x, y, \hat{\Omega}, E) = \mathbf{S}_k\Psi_{R,k}(x, y, \hat{\Omega}, E) + Q_{R,k}(x, y, \hat{\Omega}, E) + Q_{TL,k}^{\text{DeCART}}(x, y, \hat{\Omega}, E) \quad (2.63)$$

Which are now coupled to each other directly through the transverse leakage source and need no solution for $\psi_Z(\boldsymbol{r}, \hat{\Omega}, E)$.

The primary concern with this method is that the approximation of the slice interaction is basically just a finite difference approximation of the flux between slices, making it potentially inaccurate and unstable.

2.6.3 MICADO

MICADO [62] does not assume that the transverse leakage source is isotropic and instead simply carries out the integral of the original formulation:

$$Q_{TL,k}^{\text{MICADO}}(x, y, \hat{\Omega}, E) \approx \frac{\Omega_z}{\Delta z_k}\left[\Psi_Z(x, y, z_{k-1/2}, \hat{\Omega}, E) - \Psi_Z(x, y, z_{k+1/2}, \hat{\Omega}, E)\right] \quad (2.64)$$

So now Ψ_Z is the solution to the transport equation:

$$\mathbf{L}_Z\Psi_Z(\boldsymbol{r}, \hat{\Omega}, E) = \mathbf{S}\Psi_Z(\boldsymbol{r}, \hat{\Omega}, E) + Q_Z(\boldsymbol{r}, \hat{\Omega}, E) + Q_{RL}(\boldsymbol{r}, \hat{\Omega}, E) \quad (2.65)$$

With a radial leakage source that is axially constant over each slice. That is to say, for $z_{k-1/2} < z < z_{k+1/2}$:

$$Q_{RL}(\boldsymbol{r}, \hat{\Omega}, E) = -\left[\Omega_x\frac{\partial}{\partial x} + \Omega_y\frac{\partial}{\partial y}\right]\Psi_{R,k}(x, y, \hat{\Omega}, E), \quad z_{k-1/2} < z < z_{k+1/2} \quad (2.66)$$

Here $\Psi_{R,k}(x, y, \hat{\Omega}, E)$ are the solutions for the new radial equations:

$$\mathbf{L}_{R,k}\Psi_{R,k}(x, y, \hat{\Omega}, E) = \mathbf{S}_k\Psi_{R,k}(x, y, \hat{\Omega}, E) + Q_{R,k}(x, y, \hat{\Omega}, E) + Q_{TL,k}^{\text{MICADO}}(x, y, \hat{\Omega}, E) \quad (2.67)$$

Which are now indirectly coupled to each other through the solution of the full axial transport equation that depends on the flux in each slice.

The primary concern with this method is that the solution of the 1D MOC equation is not cheap to compute compared to the other methods. Additionally, it requires axially extruded meshes and the fact that the leakage must be stored for each FSR introduces memory concerns.

2.6.4 NECP-X

Similar to MICADO, NECP-X [29] solves the full transport equation in the axial direction for the neutron leakage. NECP-X also introduces a material leakage approximation for the axial calculation. The traditional pin based leakage involves the radial equation with fully anisotropic axial leakage for an axial equation similar that of MPACT with homogenized cross sections in the pin cell. In this method, the radial leakage into the 1D equation for pin cell j is expressed as:

$$TL_j^{Radial}(z,\hat{\Omega},E) = \frac{\Omega_x}{\Delta x_j}\left[\psi_{j,x+}(z,\hat{\Omega},E) - \psi_{j,x-}(z,\hat{\Omega},E)\right] + \frac{\Omega_y}{\Delta y_j}\left[\psi_{j,y+}(z,\hat{\Omega},E) - \psi_{j,y-}(z,\hat{\Omega},E)\right] \quad (2.68)$$

and the cross sections are homogenized for the axial problem as:

$$\Sigma_t^j(E) = \frac{\int_{\Delta x_j}\int_{\Delta y_j}\Sigma_t(x,y,E)\phi(x,y,E)\,dy\,dx}{\int_{\Delta x_j}\int_{\Delta y_j}\phi(x,y,E)\,dy\,dx} \quad (2.69)$$

To increase discretization accuracy and avoid cross section homogenization, NECP-X instead took a material leakage approach. First MOC is applied, and then the characteristic incoming and outgoing fluxes in the segments are used to compute the material leakage, making the radial leakage for material p in pin cell j now:

$$TL_{j,p}^{Radial}(z,\hat{\Omega}_m,E) = \sum_{l=1}^{L_{j,p,m}} \frac{\sqrt{1-\mu^2}dA_m}{A_{j,p}}\left[\psi_{l,out}(z,\hat{\Omega}_m,E) - \psi_{l,in}(z,\hat{\Omega}_m,E)\right] \quad (2.70)$$

where l is the index of the $L_{j,p,m}$ characteristic segments for that angle intersecting the material region, dA_m is the ray spacing, and $A_{j,p}$ is the total area of the material region.

So that now the axial equation is solved in each material region of each pin cell instead of the pin cell as a whole, avoiding cross section homogenization. This method demonstrated some noticeable improvement in eigenvalue accuracy for a BWR assembly case tested by NECP-X reducing the pin based 2D/1D method error from 84 pcm down to 7 pcm, with a cost of adding an additional 10% run time and 9% memory usage. Additionally three C5G7 cases were tested, an unrodded case and two cases of different rod insertions. The three cases showed improvement in the eigenvalue from errors of 34, 63, and 72 pcm in the pin based calculation, to errors of 22, 33, and 24 pcm in the material based method. The C5G7 results showed a similar time cost as the BWR assembly had shown with additional sweep time of around 8% and additional memory usage of about 9%. Overall this development suggests the viability of materials based traditional 2D/1D as a way to both improve accuracy and perhaps reduce instability by avoiding cross section homogenization.

Some concerns with this method is that the 1D axial equation must now be computed for each material region in each pin cell, increasing the costs of axial calculation. Furthermore, while this method does not strictly require axially extruded meshes, it is invalid for systems without axially extruded materials unless an approximation between the material solutions is made. As such, any model with water buffers above or below fuel cannot use the material leakage method introduced by NECP-X as is.

2.6.5 Proteus-MOC

Proteus-MOC [18] [63] [64] [65] [66] discretizes the geometry into $k = 1, 2, \ldots, K$ planes and $j = 1, 2, \ldots, J$ elements on each plane. As such, it is necessary that every single plane have the same radial divisions. However, it is not a traditional 2D/1D method, and instead directly discretizes the 3D transport equation, but treating the axial discretization independent of the radial discretization. It assumes that the source is radially constant in each of the J elements, only depending on the axial change, and that every single plane can have the axial dependence expressed by a set of orthogonal basis functions $(b_k^1, b_k^2, \ldots, b_k^I)$:

$$Q_{j,k}(\boldsymbol{r}, \hat{\Omega}, E) \approx Q_{j,k}(z, \hat{\Omega}, E) = \sum_{i=1}^{I} Q_{j,k}^i(\hat{\Omega}, E) b_k^i(z) \tag{2.71}$$

It similarly expands the flux in each element, but makes no requirements on the radial dependence in an element:

$$\psi_{j,k}(\boldsymbol{r}, \hat{\Omega}, E) \approx \sum_{i=1}^{I} \psi_{j,k}^i(x, y, \hat{\Omega}, E) b_k^i(z) \tag{2.72}$$

So now the radial equation in an element is (assuming constant cross sections in the element and no integration over z yet):

$$\mathbf{L}_{R,j,k} \sum_{i=1}^{I} \psi_{j,k}^i(x, y, \hat{\Omega}, E) b_k^i(z) = \sum_{i=1}^{I} Q_{j,k}^i(\hat{\Omega}, E) b_k^i(z) - \Omega_z \sum_{i=1}^{I} \psi_{j,k}^i(x, y, \hat{\Omega}, E) \frac{d}{dz} b_k^i(z) \tag{2.73}$$

If we then multiply by b_k^l and integrate from $z_{k-1/2}$ to $z_{k+1/2}$, we get:

$$\begin{aligned} \left[\mathbf{L}_{R,j,k} \psi_{j,k}^l(x, y, \hat{\Omega}, E) - Q_{j,k}^l(\hat{\Omega}, E)\right] \int_{z_{k-1/2}}^{z_{k+1/2}} \left(b_k^l(z)\right)^2 \, dz \\ + \Omega_z \sum_{i=1}^{I} \psi_{j,k}^i(x, y, \hat{\Omega}, E) \int_{z_{k-1/2}}^{z_{k+1/2}} b_k^l(z) \frac{d}{dz} b_k^i(z) \, dz = 0 \end{aligned} \tag{2.74}$$

We can use the product rule to get:

$$b_k^l(z)\frac{d}{dz}b_k^i(z) = \frac{d}{dz}b_k^i(z)b_k^l(z) - b_k^i(z)\frac{d}{dz}b_k^l(z) \tag{2.75}$$

So the equation is now

$$\begin{aligned}\Big[\mathbf{L}_{R,j,k}\psi_{j,k}^l(x,y,\hat{\Omega},E) - Q_{j,k}^l(\hat{\Omega},E)\Big]\int_{z_{k-1/2}}^{z_{k+1/2}}\left(b_k^l(z)\right)^2\,dz \\ - \Omega_z\sum_{i=1}^{I}\psi_{j,k}^i(x,y,\hat{\Omega},E)\int_{z_{k-1/2}}^{z_{k+1/2}}b_k^i(z)\frac{d}{dz}b_k^l(z)\,dz \\ + \Omega_z\sum_{i=1}^{I}\psi_{j,k}^i(x,y,\hat{\Omega},E)\int_{z_{k-1/2}}^{z_{k+1/2}}\frac{d}{dz}b_k^i(z)b_k^l(z)\,dz = 0\end{aligned} \tag{2.76}$$

Taking the final integral using the fundamental theorem of calculus gives:

$$\begin{aligned}\Big[\mathbf{L}_{R,j,k}\psi_{j,k}^l(x,y,\hat{\Omega},E) - Q_{j,k}^l(\hat{\Omega},E)\Big]\int_{z_{k-1/2}}^{z_{k+1/2}}\left(b_k^l(z)\right)^2\,dz \\ - \Omega_z\sum_{i=1}^{I}\psi_{j,k}^i(x,y,\hat{\Omega},E)\int_{z_{k-1/2}}^{z_{k+1/2}}b_k^i(z)\frac{d}{dz}b_k^l(z)\,dz \\ + \Omega_z\sum_{i=1}^{I}\psi_{j,k}^i(x,y,\hat{\Omega},E)\Big[b_k^i(z_{k+1/2})b_k^l(z_{k+1/2}) - b_k^i(z_{k-1/2})b_k^l(z_{k-1/2})\Big] = 0\end{aligned} \tag{2.77}$$

But we know that from our flux expansion:

$$\sum_{i=1}^{I}\psi_{j,k}^i(x,y,\hat{\Omega},E)b_k^i(z_{k+1/2}) = \psi_{j,k+1/2}(x,y,\hat{\Omega},E) = \psi_j(x,y,z_{k+1/2},\hat{\Omega},E) \tag{2.78}$$

Which is the top interface flux of the element. Then the equation is now:

$$\begin{aligned}\Big[\mathbf{L}_{R,j,k}\psi_{j,k}^l(x,y,\hat{\Omega},E) - Q_{j,k}^l(\hat{\Omega},E)\Big]\int_{z_{k-1/2}}^{z_{k+1/2}}\left(b_k^l(z)\right)^2\,dz \\ - \Omega_z\sum_{i=1}^{I}\psi_{j,k}^i(x,y,\hat{\Omega},E)\int_{z_{k-1/2}}^{z_{k+1/2}}b_k^i(z)\frac{d}{dz}b_k^l(z)\,dz \\ + \Omega_z\Big[\psi_{j,k+1/2}(x,y,\hat{\Omega},E)b_k^l(z_{k+1/2}) - \psi_{j,k-1/2}(x,y,\hat{\Omega},E)b_k^l(z_{k-1/2})\Big] = 0\end{aligned} \tag{2.79}$$

So for $\Omega_z > 0$, we will need the flux at the bottom as a boundary condition (found by solving the elements below it in the extruded mesh) so that now the equation is (moving all "source" like

terms to the right hand side):

$$\begin{aligned}\mathbf{L}_{R,j,k}\psi^l_{j,k}(x,y,\hat{\Omega},E)\int_{z_{k-1/2}}^{z_{k+1/2}}\left(b^l_k(z)\right)^2\,dz \\ -\Omega_z\sum_{i=1}^{I}\psi^i_{j,k}(x,y,\hat{\Omega},E)\int_{z_{k-1/2}}^{z_{k+1/2}}b^i_k(z)\frac{d}{dz}b^l_k(z)\,dz \\ +\Omega_z\sum_{i=1}^{I}\psi^i_{j,k}(x,y,\hat{\Omega},E)b^i_k(z_{k+1/2})b^l_k(z_{k+1/2}) \\ =Q^l_{j,k}(\hat{\Omega},E)\int_{z_{k-1/2}}^{z_{k+1/2}}\left(b^l_k(z)\right)^2\,dz \\ +\Omega_z\psi_{j,k-1/2}(x,y,\hat{\Omega},E)b^l_k(z_{k-1/2}) \quad (2.80)\end{aligned}$$

and similarly for $\Omega_z > 0$. Then this is a system of I coupled 2D transport equations in each element in each axial plane and can be solved for each $\psi^i_{j,k}(x,y,\hat{\Omega},E)$ for $i = 1,2,\ldots,I$ using any standard 2D method. Proteus-MOC then makes the expansion linear in z so that there are only two equations.

The primary concerns with this method is that it can be expensive to have to store the top and bottom flux for every single element in every plane. Additionally, the method requires that the mesh is extruded so that the radial discretization must be axially uniform. Furthermore, the full MOC form of the equations that are actually solved by Proteus-MOC involve matrix exponentials, which can be costly to compute.

Thus far, the primary benchmarking of Proteus-MOC has been limited to C5G7 problems. While one C5G7 case was run with a void channel, no cases have been run with bare fuel pin cells surrounded by void. As such, the ability of the Proteus-MOC method to maintain stability in cases where bare fuel is exposed to void and neutronically important, has yet to be investigated. As the method in this work is based on the Proteus-MOC method, these types of tests will constitute new investigation into the method's ability to mitigate this instability.

2.6.6 STREAM

Much like Proteus-MOC, STREAM [67] directly discretizes the 3D NTE with a different axial discretization for a set of radial slices. STREAM uses diamond differencing to approximate the axial variable in each radial slice, a method referred to as MOC/DD. To do so, STREAM constructs the 3D flux and source as a linear combination of 2D radial and 1D axial components by approximating the flux in a given slice as follows:

$$\psi_k(\boldsymbol{r},\hat{\Omega},E) \approx \psi^0_k(x,y,\hat{\Omega},E) + \frac{z}{\Delta z_k}\left(\psi^+_k(x,y,\hat{\Omega},E) - \psi^-_k(x,y,\hat{\Omega},E)\right) \quad (2.81)$$

Here ψ_k^+ is defined as the flux at the top of the slice and ψ_k^- is defined as the flux at the bottom of the slice and $-\frac{\Delta z}{2} \leq z \leq \frac{\Delta z}{2}$. Using the diamond differencing scheme, the axially averaged flux is expressed as:

$$\psi_k^0(x, y, \hat{\Omega}, E) = \frac{1}{2}\left(\psi_k^+(x, y, \hat{\Omega}, E) + \psi_k^-(x, y, \hat{\Omega}, E)\right) \tag{2.82}$$

Introducing this approximation to the radial NTE and integrating over the axial slice gives:

$$\mathbf{L}_{R,k}\psi_k^0(x, y, \hat{\Omega}, E) = \mathbf{S}_k\psi_k^0(x, y, \hat{\Omega}, E) - \frac{\Omega_z}{\Delta z}\left(\psi_k^+(x, y, \hat{\Omega}, E) - \psi_k^-(x, y, \hat{\Omega}, E)\right) \tag{2.83}$$

For upward moving flux, $\Omega_z > 0$, this is further simplified by adding $\frac{2\Omega_z}{\Delta z}\psi_k^0(x, y, \hat{\Omega}, E)$ to each side to give:

$$\mathbf{L}_{R,k}\psi_k^0(x, y, \hat{\Omega}, E) + \frac{2\Omega_z}{\Delta z}\psi_k^0(x, y, \hat{\Omega}, E) = \mathbf{S}_k\psi_k^0(x, y, \hat{\Omega}, E) + \frac{2\Omega_z}{\Delta z}\psi_k^-(x, y, \hat{\Omega}, E) \tag{2.84}$$

So that now $\psi_k^-(x, y, \hat{\Omega}, E)$ is the incoming flux from the slice below. For the boundary this value is known through boundary conditions. For the slice above to be computed, the top flux must be calculated by the results in this slice since $\psi_k^+(x, y, \hat{\Omega}, E) = \psi_{k+1}^-(x, y, \hat{\Omega}, E)$. Using the diamond differencing scheme, that top flux (which acts as the leakage source for the slice above) becomes:

$$\psi_k^+(x, y, \hat{\Omega}, E) = 2\psi_k^0(x, y, \hat{\Omega}, E) - \psi_k^-(x, y, \hat{\Omega}, E) \tag{2.85}$$

The downward moving equations are analogously derived by instead subtracting $\frac{2\Omega_z}{\Delta z}\psi_k^0(x, y, \hat{\Omega}, E)$ from each side of Equation 2.83.

This completes the diamond differencing discretization of the axial portion of the problem, leaving only a 2D radial problem left. This radial problem can then be discretized using 2D MOC to give the MOC/DD equations and the FSR divisions are used to compute and translate the axial leakage to the FSR above and below. For the implementation in STREAM, the slices are swept up and down so only one slice leakage need be stored at a time.

The diamond differencing scheme utilized by this method for discretization of the 3D transport equation avoids the need for matrix exponential calculations that often appear in similar methods such as the one in Proteus-MOC and presented in this work. Results from this method do appear promising with respect to calculation time. C5G7 [68] was solved to an acceptable accuracy in 0.81 core hours and the BEAVRS [69] benchmark was solved in 477.28 core hours, which is comparable to the speed of traditional 2D/1D methods.

Some concerns with this method is that it can be expensive to store the top and bottom flux for every single element in a plane. Furthermore, the fact that the planes must be swept up and down limits the potential of spatial domain decomposition for parallel implementations since each plane

must be solved in order in the up and down sweeps. If the leakage were to be lagged, this limitation to the domain decomposition could be avoided, but at the cost of the requirement of storing the axial leakage for every single element of every single plane. However, radial decomposition is still possible and utilized in STREAM with scaling efficiency of over 80% at just over 140 cores in the BEAVRS benchmark. Additionally, the method requires that the mesh be axially extruded so that the radial discretization must be axially uniform.

2.7 Summary

This chapter covered the basics of neutron transport theory from a NTE centered perspective. We discussed the general transport equation as well as the eigenvalue problems that come out of it. Methods for solving the NTE were also introduced, including 2D/1D methods. Most of the content of this chapter is very well known in the nuclear engineering community and commonly used in reactor physics work. The next chapter provides the derivation of the LPAEM as an alternative to traditional 2D/1D methods.

CHAPTER 3

The Legendre Polynomial Axial Expansion Method for Neutron Transport

The focus of this dissertation is the development and implementation of the *Legendre Polynomial Axial Expansion Method* (LPAEM) for solving the 3D NTE. In this chapter, the formulation of the method is presented as are optional leakage approximation methods.

3.1 The Legendre Polynomial Axial Expansion Equations

We begin with the multi-group discrete ordinates eigenvalue problem:

$$\hat{\Omega}_m \cdot \boldsymbol{\nabla} \psi_{m,g}(\boldsymbol{r}) + \Sigma_{t,g}(\boldsymbol{r}) \psi_{m,g}(\boldsymbol{r}) = Q_{m,g}(\boldsymbol{r}) \tag{3.1}$$

Where the source is:

$$Q_{m,g}(\boldsymbol{r}) = \frac{\chi_g}{4\pi k_{eff}} \sum_{g'=1}^{G} \nu\Sigma_{f,g'}(\boldsymbol{r}) \phi_{g'}(\boldsymbol{r}) + \sum_{g'=1}^{G} \sum_{m'=1}^{M} \Sigma_{s,m' \to m, g' \to g, l}(\boldsymbol{r}) \psi_{m',g'}(\boldsymbol{r}) w_{m'} \tag{3.2}$$

and:

$$\phi_g(\boldsymbol{r}) = \sum_{m=1}^{M} \psi_{m,g}(\boldsymbol{r}) w_m \tag{3.3}$$

Writing the equation out a bit more shows the three differential terms to be dealt with:

$$\Omega_{x,m} \frac{\partial}{\partial x} \psi_{m,g}(\boldsymbol{r}) + \Omega_{y,m} \frac{\partial}{\partial y} \psi_{m,g}(\boldsymbol{r}) + \Omega_{z,m} \frac{\partial}{\partial z} \psi_{m,g}(\boldsymbol{r}) + \Sigma_{t,g}(\boldsymbol{r}) \psi_{m,g}(\boldsymbol{r}) = Q_{m,g}(\boldsymbol{r}) \tag{3.4}$$

We will now divide the system into $k = 1, 2, \ldots, K$ axial slices and assume that the slice divisions are such that cross sections are axially invariant in a single slice. We will also divide the radial system into $j = 1, 2, \ldots, J$ pin cells.

3.1.1 Legendre Polynomial Axial Approximation

We will make the following approximation of the flux in a slice:

$$\psi_{k,m,g}(\boldsymbol{r}) = \sum_{n=0}^{N} \Psi_{k,m,g,n}(x,y) P_n(\xi_{z_k}) \tag{3.5}$$

Where ξ_{z_k} is the normalized z variable in each slice and ranges from -1 to 1 for every slice. The desire here is that this expansion will result in better intra-nodal resolution of the flux to better solve coarse axial sliced systems. So for a slice centered at z_k with width $\Delta z_k = z_{k+1/2} - z_{k-1/2}$, then $\xi_{z_k} = \frac{2(z-z_k)}{\Delta z_k}$ for $z_{k-1/2} \leq z \leq z_{k+1/2}$. This brings about an important observation. Due to the change of variables necessary to compute the integral, we get the following from the Legendre Polynomial orthogonality:

$$\int_{z_{k-1/2}}^{z_{k+1/2}} P_n(\xi_{z_k}) P_r(\xi_{z_k})\, dz = \frac{\Delta z_k}{2r+1} \delta_{n,r} \tag{3.6}$$

This should be kept in mind for future portions of the derivation.

We now introduce this approximation into our equation and consider it inside a single slice:

$$\begin{aligned} \Omega_{x,m} \frac{\partial}{\partial x} \sum_{n=0}^{N} \Psi_{k,m,g,n}(x,y) P_n(\xi_{z_k}) + \Omega_{y,m} \frac{\partial}{\partial y} \sum_{n=0}^{N} \Psi_{k,m,g,n}(x,y) P_n(\xi_{z_k}) + \Omega_{z,m} \frac{\partial}{\partial z} \psi_{k,m,g}(\boldsymbol{r}) \\ + \Sigma_{t,k,g}(x,y) \sum_{n=0}^{N} \Psi_{k,m,g,n}(x,y) P_n(\xi_{z_k}) = \sum_{n=0}^{N} Q_{k,m,g,n}(x,y) P_n(\xi_{z_k}) \end{aligned} \tag{3.7}$$

notice that the axial streaming term has not yet had the approximation introduced. This will be done later to keep the algebra simpler to follow.

Where:

$$\begin{aligned} Q_{k,m,g,n}(x,y) = \frac{\chi_g}{4\pi k_{eff}} \sum_{g'=1}^{G} \nu \Sigma_{f,k,g'}(x,y) \phi_{k,g',n}(x,y) \\ + \sum_{g'=1}^{G} \sum_{l=0}^{\infty} \Sigma_{s,k,g' \to g,l}(x,y) \sum_{r=-l}^{l} R_{l,r}(\hat{\Omega}_m) \sum_{m'=1}^{M} R_{l,r}(\hat{\Omega}_{m'}) \Psi_{k,m',g',n}(x,y) w_{m'} \end{aligned} \tag{3.8}$$

3.1.2 Reduced Moment Equations

We will then multiply the equation by some Legendre polynomial $P_r(\xi_{z_k})$, where $r \leq N$, and integrate over the slice:

$$\Omega_{x,m}\frac{\partial}{\partial x}\Psi_{k,m,g,r}(x,y) + \Omega_{y,m}\frac{\partial}{\partial y}\Psi_{k,m,g,r}(x,y) + \Sigma_{t,k,g}(x,y)\Psi_{k,m,g,r}(x,y) + \frac{2r+1}{\Delta z_k}\Omega_{z,m}\int_{z_{k-1/2}}^{z_{k+1/2}} P_r(\xi_{z_k})\frac{\partial}{\partial z}\psi_{k,m,g}(\boldsymbol{r})\,dz = Q_{k,m,g,r}(x,y) \quad (3.9)$$

We use integration by parts to evaluate that final term (remember also that $P_n(1) = 1$ and $P_n(-1) = (-1)^n$):

$$\int_{z_{k-1/2}}^{z_{k+1/2}} P_r(\xi_{z_k})\frac{\partial}{\partial z}\psi_{k,m,g}(\boldsymbol{r})\,dz = \psi_{k,m,g}(x,y,z_{k+1/2}) - (-1)^r\psi_{k,m,g}(x,y,z_{k-1/2}) - \int_{z_{k-1/2}}^{z_{k+1/2}} \psi_{k,m,g}(\boldsymbol{r})\frac{\partial}{\partial z}P_r(\xi_{z_k})\,dz \quad (3.10)$$

We will reintroduce the polynomial approximation to expand the final integral as:

$$\int_{z_{k-1/2}}^{z_{k+1/2}} \psi_{k,m,g}(\boldsymbol{r})\frac{\partial}{\partial z}P_r(\xi_{z_k})\,dz = \sum_{n=0}^{N}\Psi_{k,m,g,n}(x,y)\int_{z_{k-1/2}}^{z_{k+1/2}} P_n(\xi_{z_k})\frac{\partial}{\partial z}P_r(\xi_{z_k})\,dz \quad (3.11)$$

We use the following property of Legendre Polynomials:

$$\frac{d}{dx}P_n(x) = (2(n-1)+1)P_{n-1}(x) + (2(n-3)+1)P_{n-3}(x) + (2(n-5)+1)P_{n-5}(x) + \cdots \quad (3.12)$$

to further expand the individual integrals (notice use of the chain rule):

$$\int_{z_{k-1/2}}^{z_{k+1/2}} P_n(\xi_{z_k})\frac{\partial}{\partial z}P_r(\xi_{z_k})\,dz = \frac{2}{\Delta z_k}\int_{z_{k-1/2}}^{z_{k+1/2}} P_n(\xi_{z_k})\Big[(2(r-1)+1)P_{r-1}(\xi_{z_k}) + \cdots\Big]\,dz \quad (3.13)$$

Now we recall the orthogonality of Legendre Polynomials, which then makes this integral:

$$\int_{z_{k-1/2}}^{z_{k+1/2}} P_n(\xi_{z_k})\frac{d}{dz}P_r\left(\xi_{z_k}\right)\,dz = 2\sum_{u=1}^{\lceil r/2\rceil}\delta_{r-2u+1,n} = \begin{cases} 0 & n \geq r \\ 0 & n_{\text{odd}}\ \&\ r_{\text{odd}} \\ 0 & n_{\text{even}}\ \&\ r_{\text{even}} \\ 2 & \text{otherwise} \end{cases} \quad (3.14)$$

So our equation is now:

$$\Omega_{x,m}\frac{\partial}{\partial x}\Psi_{k,m,g,r}(x,y)+\Omega_{y,m}\frac{\partial}{\partial y}\Psi_{k,m,g,r}(x,y)+\Sigma_{t,k,g}(x,y)\Psi_{k,m,g,r}(x,y)$$
$$+\frac{2r+1}{\Delta z_k}\Omega_{z,m}\Bigg[\psi_{k,m,g}(x,y,z_{k+1/2})-(-1)^r\psi_{k,m,g}(x,y,z_{k-1/2})$$
$$-2\sum_{n=0}^{N}\Psi_{k,m,g,n}(x,y)\sum_{u=1}^{\lceil r/2\rceil}\delta_{r-2u+1,n}\Bigg]=Q_{k,m,g,r}(x,y) \quad (3.15)$$

The sum can then be simplified:

$$\Omega_{x,m}\frac{\partial}{\partial x}\Psi_{k,m,g,r}(x,y)+\Omega_{y,m}\frac{\partial}{\partial y}\Psi_{k,m,g,r}(x,y)+\Sigma_{t,k,g}(x,y)\Psi_{k,m,g,r}(x,y)$$
$$+\frac{2r+1}{\Delta z_k}\Omega_{z,m}\Bigg[\psi_{k,m,g}(x,y,z_{k+1/2})-(-1)^r\psi_{k,m,g}(x,y,z_{k-1/2})$$
$$-2\sum_{u=1}^{\lceil r/2\rceil}\Psi_{k,m,g,r-2u+1}(x,y)\Bigg]=Q_{k,m,g,r}(x,y) \quad (3.16)$$

Now we will consider this equation differently for $\Omega_{z,m}>0$ then for $\Omega_{z,m}<0$. First, for $\Omega_{z,m}>0$ we will move the bottom flux to the RHS. We will also introduce the expansion of the flux to the top flux:

$$\Omega_{x,m}\frac{\partial}{\partial x}\Psi_{k,m,g,r}(x,y)+\Omega_{y,m}\frac{\partial}{\partial y}\Psi_{k,m,g,r}(x,y)+\Sigma_{t,k,g}(x,y)\Psi_{k,m,g,r}(x,y)$$
$$+\frac{2r+1}{\Delta z_k}\Omega_{z,m}\Bigg[\sum_{n=0}^{N}\Psi_{k,m,g,n}(x,y)-2\sum_{u=1}^{\lceil r/2\rceil}\Psi_{k,m,g,r-2u+1}(x,y)\Bigg]$$
$$=Q_{k,m,g,r}(x,y)+\frac{2r+1}{\Delta z_k}\Omega_{z,m}(-1)^r\psi_{k,m,g}(x,y,z_{k-1/2}),\ \forall\,\Omega_{z,m}>0 \quad (3.17)$$

Now for the lower boundary slice the bottom flux is given by the boundary condition. For non boundary slices the bottom flux is determined by the solution of the slice below. We will also now assume that we have divided the plane into regions where we will treat the incoming axial portion of the flux as constant. What this division is has not yet been stated but we will assume it ranges over some area $\partial V_{k,j}$ and further radial divisions will not overlap with these divisions. That is to

say that no radial division will have multiple flat axial incoming flux regions:

$$\Omega_{x,m}\frac{\partial}{\partial x}\Psi_{k,m,g,r}(x,y)+\Omega_{y,m}\frac{\partial}{\partial y}\Psi_{k,m,g,r}(x,y)+\Sigma_{t,k,g}(x,y)\Psi_{k,m,g,r}(x,y) + \frac{2r+1}{\Delta z_k}\Omega_{z,m}\left[\sum_{n=0}^{N}\Psi_{k,m,g,n}(x,y)-2\sum_{u=1}^{\lceil r/2\rceil}\Psi_{k,m,g,r-2u+1}(x,y)\right] = \mathcal{Q}^{up}_{k,m,g,r}(x,y),\ \forall\,\Omega_{z,m}>0 \quad (3.18)$$

Where:

$$\mathcal{Q}^{up}_{k,m,g,r}(x,y)=Q_{k,m,g,r}(x,y)+\frac{2r+1}{\Delta z_k}(-1)^r TL^{up}_{k,j,m,g} \quad (3.19)$$

So that:

$$TL^{up}_{k,j,m,g}=\begin{cases}\frac{\Omega_{z,m}}{\partial V_{k,j}}\int_{\partial V_{k,j}}\psi^b_g(x,y,0,\hat{\Omega}_m)\,dA & k=1\\ \mathbf{F}\Omega_{z,m}\psi_{k-1,m,g}(x,y,z_{k-1/2}) & k\neq 1\end{cases} \quad (3.20)$$

where $\mathbf{F}$ is some as yet undetermined function that comes from various transverse leakage approximations discussed in Section 3.2. And similarly for $\hat{\Omega}_{m,z}<0$:

$$\Omega_{x,m}\frac{\partial}{\partial x}\Psi_{k,m,g,r}(x,y)+\Omega_{y,m}\frac{\partial}{\partial y}\Psi_{k,m,g,r}(x,y)+\Sigma_{t,k,g}(x,y)\Psi_{k,m,g,r}(x,y) - \frac{2r+1}{\Delta z_k}\Omega_{z,m}\left[\sum_{n=0}^{N}(-1)^{r+n}\Psi_{k,m,g,n}(x,y)+2\sum_{u=1}^{\lceil r/2\rceil}\Psi_{k,m,g,r-2u+1}(x,y)\right] = \mathcal{Q}^{down}_{k,m,g,r}(x,y),\ \forall\,\Omega_{z,m}<0 \quad (3.21)$$

where:

$$\mathcal{Q}^{down}_{k,m,g,r}(x,y)=Q_{k,m,g,r}(x,y)-\frac{2r+1}{\Delta z_k}TL^{down}_{k,j,m,g} \quad (3.22)$$

$$TL^{down}_{k,j,m,g}=\begin{cases}\frac{\Omega_{z,m}}{\partial V_{k,j}}\int_{\partial V_{k,j}}\psi^b(x,y,Z_{max},\hat{\Omega}_m,E)\,dA & k=K\\ \mathbf{F}\Omega_{z,m}\psi_{k+1,m,g}(x,y,z_{k+1/2}) & k\neq K\end{cases} \quad (3.23)$$

For vacuum BCs the incoming flux is 0 so we get:

$$TL^{up}_{1,j,m,g}=0,\quad TL^{down}_{K,j,m,g}=0 \quad (3.24)$$

For reflective BCs the incoming flux is the downward moving flux of the same azimuthal angle

at the bottom of the system.

$$TL^{up}_{1,j,m,g} = \mathbf{F}\Omega_{z,m}\psi_{1,m',g}(x,y,z_{1/2}),\ \Omega_{x,m} = \Omega_{x,m'},\ \Omega_{y,m} = \Omega_{y,m'},\ \Omega_{z,m} = -\Omega_{z,m'} \tag{3.25a}$$

$$TL^{down}_{K,j,m,g} = \mathbf{F}\Omega_{z,m}\psi_{K,m',g}(x,y,z_{K+1/2}),\ \Omega_{x,m} = \Omega_{x,m'},\ \Omega_{y,m} = \Omega_{y,m'},\ \Omega_{z,m} = -\Omega_{z,m'} \tag{3.25b}$$

3.1.3 Matrix-Vector Form

We can now write these equations in matrix vector format. The notational convention used here involves a single bar over 1D vectors, i.e. $\bar{b}$, and two bars over 2D matrices, i.e. $\bar{\bar{A}}$. All vectors here are of size $N+1$, and all matrices are of size $(N+1)\times(N+1)$. Define:

$$\bar{\Psi}_{k,m,g}(x,y) = \big(\Psi_{k,m,g,0}(x,y),\ldots,\Psi_{k,m,g,N}(x,y)\big)^T \tag{3.26a}$$

$$\bar{Q}_{k,m,g}(x,y) = \big(Q_{k,m,g,0}(x,y),\ldots,Q_{k,m,g,N}(x,y)\big)^T \tag{3.26b}$$

$$\bar{a} = \Big(1,3,\ldots,2N+1\Big)^T \tag{3.26c}$$

$$\bar{b} = \Big(1,-3,\ldots,(-1)^N(2N+1)\Big)^T \tag{3.26d}$$

$$\bar{\mathcal{Q}}^{down}_{k,m,g}(x,y) = \bar{Q}_{k,m,g}(x,y) - \frac{TL^{down}_{k,j,m,g}}{\Delta z_k}\bar{a} \tag{3.26e}$$

$$\bar{\mathcal{Q}}^{up}_{k,m,g}(x,y) = \bar{Q}_{k,m,g}(x,y) + \frac{TL^{up}_{k,j,m,g}}{\Delta z_k}\bar{b} \tag{3.26f}$$

$$\bar{\bar{S}}^{down}_{k,m,g}(x,y) = \frac{\Omega_{z,m}}{\Delta z_k}\bar{\bar{C}}^{down} + \Sigma_{t,k,g}(x,y)\bar{\bar{I}} \tag{3.26g}$$

$$\bar{\bar{S}}^{up}_{k,m,g}(x,y) = \frac{\Omega_{z,m}}{\Delta z_k}\bar{\bar{C}}^{up} + \Sigma_{t,k,g}(x,y)\bar{\bar{I}} \tag{3.26h}$$

$$\bar{\bar{C}}^{down} = \bar{\bar{A}}^{down} + \bar{\bar{B}} \tag{3.26i}$$

$$\bar{\bar{C}}^{up} = \bar{\bar{A}}^{up} + \bar{\bar{B}} \tag{3.26j}$$

$$\bar{\bar{A}}^{down} = \begin{bmatrix} -1 & 1 & \cdots & (-1)^{N+1} \\ 3 & -3 & \cdots & 3(-1)^{N+2} \\ \vdots & \vdots & \vdots & \vdots \\ (2N+1)(-1)^{N+1} & (2N+1)(-1)^{N+2} & \cdots & -(2N+1) \end{bmatrix} \tag{3.26k}$$

$$\bar{\bar{A}}^{up} = \begin{bmatrix} 1 & \cdots & 1 \\ 3 & \cdots & 3 \\ \vdots & \vdots & \vdots \\ 2N+1 & \cdots & 2N+1 \end{bmatrix} \tag{3.26l}$$

$$\bar{\bar{B}} = \begin{bmatrix} 0 & 0 & \cdots & \ldots & 0 & 0 \\ -6 & 0 & \ddots & 0 & 0 & 0 \\ 0 & -10 & 0 & \ddots & 0 & 0 \\ -14 & 0 & -14 & \ddots & 0 & 0 \\ \vdots & \ddots & \ddots & \ddots & \ddots & \vdots \\ \cdots & \cdots & -(4N+2) & 0 & -(4N+2) & 0 \end{bmatrix} \tag{3.26m}$$

So then our matrix-vector equations are:

$$\Omega_{x,m}\frac{\partial}{\partial x}\bar{\Psi}_{k,m,g}(x,y) + \Omega_{y,m}\frac{\partial}{\partial y}\bar{\Psi}_{k,m,g}(x,y) + \bar{\bar{S}}^{down}_{k,m,g}(x,y)\bar{\Psi}_{k,m,g}(x,y) = \bar{\mathcal{Q}}^{down}_{k,m,g}(x,y),$$
$$\forall\, \Omega_{z,m} < 0 \tag{3.27}$$

and:

$$\Omega_{x,m}\frac{\partial}{\partial x}\bar{\Psi}_{k,m,g}(x,y) + \Omega_{y,m}\frac{\partial}{\partial y}\bar{\Psi}_{k,m,g}(x,y) + \bar{\bar{S}}^{up}_{k,m,g}(x,y)\bar{\Psi}_{k,m,g}(x,y) = \bar{\mathcal{Q}}^{up}_{k,m,g}(x,y),$$
$$\forall\, \Omega_{z,m} > 0 \tag{3.28}$$

3.2 Axial Leakage Treatment

The **F** function must now be specified. Multiple options exist for determining this function that will couple the axial slices together. Presented here are 3 methods that were investigated in this work.

3.2.1 Extruded Mesh Method

Regardless of method, the axial slices must be divided into I_k FSRs on each slice. We will assume that in the process of solving an axial slice we will end up with a cell averaged value of the flux moments for each of these regions which we will refer to as follows:

$$\Psi_{k,i,m,g,n} = \frac{\int_{\partial V_i} \Psi_{k,m,g,n}(x,y)\, dA}{\int_{\partial V_i} dA} \tag{3.29}$$

Now for the Extruded Mesh Method, the cells must be extruded so that each cell below matches boundaries precisely with the cell above. This method then lines up the axial leakage regions with the slice cells so that each cell has its own axial leakage region, hence the need for extrusion of the mesh. Then the axial leakage contributor is defined as exactly the solution of the adjacent slice. For $\Omega_{z,m} < 0$ then the function is:

$$TL^{down}_{k,i,m,g} = \mathbf{F}\Omega_{z,m}\psi_{k+1,m,g}(x,y,z_{k+1/2}) = \Omega_{z,m}\sum_{n=0}^{N}(-1)^n\Psi_{k+1,i,m,g,n},\ \forall\,\Omega_{z,m} < 0 \tag{3.30a}$$

and for $\Omega_{z,m} > 0$:

$$TL^{up}_{k,i,m,g} = \mathbf{F}\Omega_{z,m}\psi_{k-1,m,g}(x,y,z_{k-1/2}) = \Omega_{z,m}\sum_{n=0}^{N}\Psi_{k-1,i,m,g,n},\ \forall\,\Omega_{z,m} > 0 \tag{3.30b}$$

So that reflective BCs give:

$$TL^{up}_{1,i,m,g} = \Omega_{z,m}\sum_{n=0}^{N}(-1)^n\Psi_{1,i,m',g,n},\ \forall\,\Omega_{z,m} < 0,\ \Omega_{x,m} = \Omega_{x,m'},\ \Omega_{y,m} = \Omega_{y,m'},\ \Omega_{z,m} = -\Omega_{z,m'} \tag{3.31}$$

And for top reflective BCs given K slices:

$$TL^{down}_{K,i,m,g} = \Omega_{z,m}\sum_{n=0}^{N}\Psi_{K,i,m',g,n},\ \forall\,\Omega_{z,m} < 0,\ \Omega_{x,m} = \Omega_{x,m'},\ \Omega_{y,m} = \Omega_{y,m'},\ \Omega_{z,m} = -\Omega_{z,m'} \tag{3.32}$$

3.2.2 Integrated Pin Cell Method

For this method the FSRs need not be extruded. Rather, each of the J "Pin Cells" (however they may be defined) are considered to be the regions over which the axial leakage is constant using a spatially averaging technique. These pin cells are then subdivided into FSRs for the radial transport solutions. At each slice, this subdivision may be accomplished in any form desired so long as no subdivision overlaps with multiple Pin Cells. As such, extrusion of the mesh is limited only to extrusion of the Pin Cells and does not require storing of the leakage flux for every single subdivision. So now instead, for $\Omega_{z,m} < 0$ the function is:

$$TL^{down}_{k,j,m,g} = \mathbf{F}\Omega_{z,m}\psi_{k+1,m,g}(x,y,z_{k+1/2}) = \frac{\Omega_{z,m}}{\partial V_j}\sum_{i_{k+1}\in\partial V_j}\partial V_i\sum_{n=0}^{N}(-1)^n\Psi_{k+1,i,m,g,n},\ \forall\,\Omega_{z,m} < 0 \tag{3.33a}$$

and for $\Omega_{z,m} > 0$:

$$TL^{up}_{k,j,m,g} = \mathbf{F}\Omega_{z,m}\psi_{k-1,m,g}(x,y,z_{k-1/2}) = \frac{\Omega_{z,m}}{\partial V_j}\sum_{i_{k-1}\in\partial V_j}\partial V_i\sum_{n=0}^{N}\Psi_{k-1,i,m,g,n},\ \forall\,\Omega_{z,m} > 0 \tag{3.33b}$$

Where multiple of the I_k subdivisions in each slice pull from the same axial leakage. So that reflective BCs give:

$$TL^{up}_{1,i,m,g} = \frac{\Omega_{z,m}}{\partial V_j}\sum_{i_1\in\partial V_j}\partial V_i\sum_{n=0}^{N}(-1)^n\Psi_{1,i,m',g,n},$$
$$\forall\,\Omega_{z,m} < 0,\ \Omega_{x,m} = \Omega_{x,m'},\ \Omega_{y,m} = \Omega_{y,m'},\ \Omega_{z,m} = -\Omega_{z,m'} \tag{3.34}$$

And for top reflective BCs given K slices:

$$TL^{down}_{K,i,m,g} = \frac{\Omega_{z,m}}{\partial V_j}\sum_{i_K\in\partial V_j}\partial V_i\sum_{n=0}^{N}\Psi_{K,i,m',g,n},$$
$$\forall\,\Omega_{z,m} < 0,\ \Omega_{x,m} = \Omega_{x,m'},\ \Omega_{y,m} = \Omega_{y,m'},\ \Omega_{z,m} = -\Omega_{z,m'} \tag{3.35}$$

The primary advantage of this method is the lack of the need for fully extruded meshes. Instead of the fine mesh divisions needing to be identical on every axial level, such as required in the method described in Section 3.2.1, *only the pin cell coarse mesh need be extruded*. This means that disjoint meshes, such as the one shown in Figure 3.1, can be used in situations where such meshes are useful.

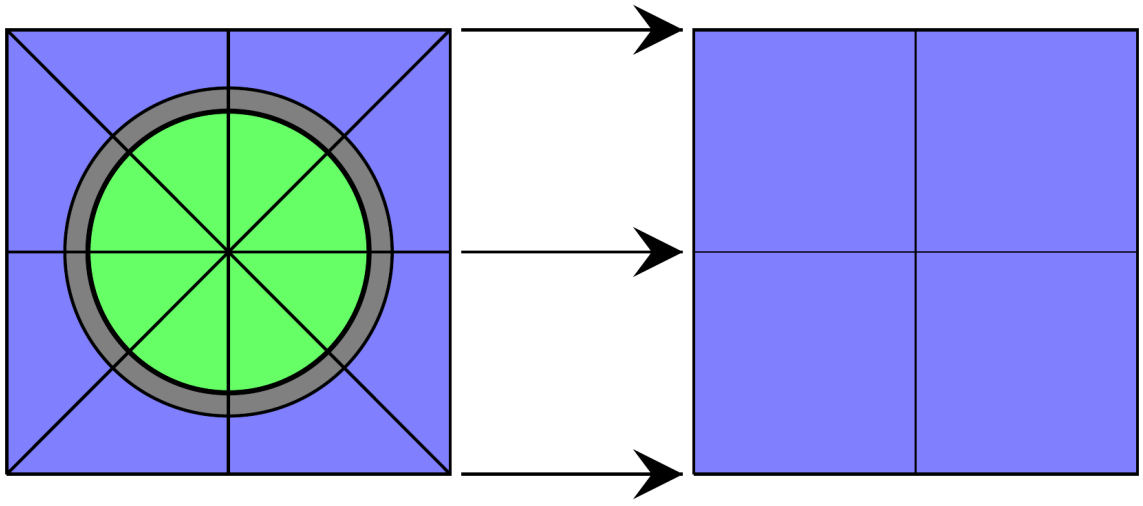

Figure 3.1: Disjoint Mesh

3.2.3 Integrated Pin Cell Current Method

For the upward moving neutrons, we will integrate the leakage term over the upper unit half sphere and divide by 2π, and similarly for the downward moving neutrons we will integrate over the lower unit half sphere and divide by 2π. This is an angle averaging technique known as a DP_0 approximation. These integrals will then serve as our "currents":

$$TL^{down}_{k,j,m,g} = \mathbf{F}\Omega_{z,m}\psi_{k+1,m,g}(x,y,z_{k+1/2}) = \frac{1}{2\pi\partial V_j}\sum_{\Omega_{z,m}<0}\Omega_{z,m}w_m\sum_{i_{k+1}\in\partial V_j}\partial V_i\sum_{n=0}^{N}(-1)^n\Psi_{k+1,i,m,g,n} \quad (3.36a)$$

$$TL^{up}_{k,j,m,g} = \mathbf{F}\Omega_{z,m}\psi_{k-1,m,g}(x,y,z_{k-1/2}) = \frac{1}{2\pi\partial V_j}\sum_{\Omega_{z,m}>0}\Omega_{z,m}w_m\sum_{i_{k-1}\in\partial V_j}\partial V_i\sum_{n=0}^{N}\Psi_{k-1,i,m,g,n} \quad (3.36b)$$

There may be some argument for isotropizing this term over the entire unit sphere. Such an argument would likely stem from the desire to only solve the flux for upward (or downward) moving neutrons. However this approach by its very nature presumes axial symmetry of the flux in each slice, exactly what we are trying to avoid! Even if we were to isotropize the axial leakage fully, it would still be necessary to compute both the up and down moving flux. This is due to the fundamental difference in the equations due to the difference in the attenuation coefficient matrices ($\bar{\bar{S}}^{up}$ and $\bar{\bar{S}}^{down}$). Additionally the leakage source is subtracted from the downward equation and added to the upward equation so even a fully isotropized leakage could not result in an equal source for both the up and down equations. One intrinsic advantage of separating the two is that the leakage term is fully up to date in every calculation while only needing the march up or down to be separated.

3.2.4 Balance Equations and F Operator Conditions

We can take the first of the matrix vector equations (for the flat values) to get the upward 0^{th} axial moment:

$$\Omega_{x,m}\frac{\partial}{\partial x}\Psi_{k,m,g,0}(x,y) + \Omega_{y,m}\frac{\partial}{\partial y}\Psi_{k,m,g,0}(x,y) + \Sigma_{t,k,g}(x,y)\Psi_{k,m,g,0}(x,y) + \frac{\Omega_{z,m}}{\Delta z_k}\sum_{n=0}^{N}\Psi_{k,m,g,n}(x,y) = Q_{k,m,g,0}(x,y) + \frac{1}{\Delta z_k}\mathbf{F}\Omega_{z,m}\psi_{k-1,m,g}(x,y,z_{k-1/2}) \quad (3.37)$$

and the downward 0^{th} axial moment:

$$\Omega_{x,m}\frac{\partial}{\partial x}\Psi_{k,m,g,0}(x,y)+\Omega_{y,m}\frac{\partial}{\partial y}\Psi_{k,m,g,0}(x,y)+\Sigma_{t,k,g}(x,y)\Psi_{k,m,g,0}(x,y)$$
$$-\frac{\Omega_{z,m}}{\Delta z_k}\sum_{n=0}^{N}(-1)^n\Psi_{k,m,g,n}(x,y)=Q_{k,m,g,0}(x,y)-\frac{1}{\Delta z_k}\mathbf{F}\Omega_{z,m}\psi_{k+1,m,g}(x,y,z_{k+1/2}) \quad (3.38)$$

We can then add the two equations together and integrate over angles to get:

$$\frac{\partial}{\partial x}J_{x,k,g}(x,y)+\frac{\partial}{\partial y}J_{y,k,g}(x,y)+\Sigma_{t,k,g}(x,y)\Phi_{k,g,0}(x,y)$$
$$+\sum_{\Omega_{z,m}>0}w_m\frac{\Omega_{z,m}}{\Delta z_k}\sum_{n=0}^{N}\Psi_{k,m,g,n}(x,y)-\sum_{\Omega_{z,m}<0}w_m\frac{\Omega_{z,m}}{\Delta z_k}\sum_{n=0}^{N}(-1)^n\Psi_{k,m,g,n}(x,y)$$
$$=Q_{k,g,0}(x,y)+\frac{1}{\Delta z_k}\sum_{\Omega_{z,m}>0}w_m\mathbf{F}\Omega_{z,m}\psi_{k-1,m,g}(x,y,z_{k-1/2})$$
$$-\frac{1}{\Delta z_k}\sum_{\Omega_{z,m}<0}w_m\mathbf{F}\Omega_{z,m}\psi_{k+1,m,g}(x,y,z_{k+1/2}) \quad (3.39)$$

We will then integrate over the rectangular domain for the j coarse cell:

$$\int_{\Delta y_j}\left(J_{x+,k,g}(y)-J_{x-,k,g}(y)\right)dy+\int_{\Delta x_j}\left(J_{y+,k,g}(x)-J_{y-,k,g}(x)\right)dx$$
$$+\int_{\partial V_j}\Sigma_{t,k,g}(x,y)\Phi_{k,g,0}(x,y)\,dA+\sum_{\Omega_{z,m}>0}w_m\frac{\Omega_{z,m}}{\Delta z_k}\sum_{n=0}^{N}\int_{\partial V_j}\Psi_{k,m,g,n}(x,y)\,dA$$
$$-\sum_{\Omega_{z,m}<0}w_m\frac{\Omega_{z,m}}{\Delta z_k}\sum_{n=0}^{N}(-1)^n\int_{\partial V_j}\Psi_{k,m,g,n}(x,y)\,dA=\int_{\partial V_j}Q_{k,g,0}(x,y)\,dA$$
$$+\frac{1}{\Delta z_k}\sum_{\Omega_{z,m}>0}w_m\int_{\partial V_j}\mathbf{F}\Omega_{z,m}\psi_{k-1,m,g}(x,y,z_{k-1/2})\,dA$$
$$-\frac{1}{\Delta z_k}\sum_{\Omega_{z,m}<0}w_m\int_{\partial V_j}\mathbf{F}\Omega_{z,m}\psi_{k+1,m,g}(x,y,z_{k+1/2})\,dA \quad (3.40)$$

We again introduce the notion of the FSR averaged flux, as well as pin cell border averaged currents, pin cell averaged flux, and pin cell averaged source i.e.:

$$J_{x\pm,k,j,g}=\frac{1}{\Delta y_j}\int_{\Delta y_j}J_{x\pm,k,g}(y)\,dy$$

$$J_{y\pm,k,j,g} = \frac{1}{\Delta x_j} \int_{\Delta x_j} J_{y\pm,k,g}(x)\, dx$$

$$\Psi_{k,j,m,g,n} = \frac{1}{\partial V_j} \int_{\partial V_j} \Psi_{k,m,g,n}(x,y)\, dA$$

$$Q_{k,j,g,0} = \frac{1}{\partial V_j} \int_{\partial V_j} Q_{k,g,0}(x,y)\, dA$$

Which can now make that equation:

$$\begin{aligned}
&\Delta y_j(J_{x+,k,j,g} - J_{x-,k,j,g}) + \Delta x_j(J_{y+,k,j,g} - J_{y-,k,j,g}) \\
&\quad + \sum_{i_k \in \partial V_j} \partial V_{k,i} \Sigma_{t,k,i,g} \Phi_{k,i,g,0} + \frac{\partial V_j}{\Delta z_k} \sum_{\Omega_{z,m}>0} w_m \Omega_{z,m} \sum_{n=0}^{N} \Psi_{k,j,m,g,n} \\
&\quad - \frac{\partial V_j}{\Delta z_k} \sum_{\Omega_{z,m}<0} w_m \Omega_{z,m} \sum_{n=0}^{N} (-1)^n \Psi_{k,j,m,g,n} = \partial V_j Q_{k,j,g,0} \\
&\quad + \frac{1}{\Delta z_k} \sum_{\Omega_{z,m}>0} w_m \int_{\partial V_j} \mathbf{F} \Omega_{z,m} \psi_{k-1,m,g}(x,y,z_{k-1/2})\, dA \\
&\quad - \frac{1}{\Delta z_k} \sum_{\Omega_{z,m}<0} w_m \int_{\partial V_j} \mathbf{F} \Omega_{z,m} \psi_{k+1,m,g}(x,y,z_{k+1/2})\, dA
\end{aligned} \tag{3.41}$$

We recall that from the definitions of Legendre polynomials that those sums of Legendre moments are top and bottom fluxes and we can again consider them pin cell averaged. So here we get:

$$\begin{aligned}
&\Delta y_j(J_{x+,k,j,g} - J_{x-,k,j,g}) + \Delta x_j(J_{y+,k,j,g} - J_{y-,k,j,g}) \\
&\quad + \sum_{i_k \in \partial V_j} \partial V_{k,i} \Sigma_{t,k,i,g} \Phi_{k,i,g,0} + \frac{\partial V_j}{\Delta z_k} \sum_{\Omega_{z,m}>0} w_m \Omega_{z,m} \Psi^{top}_{k,j,m,g,n} \\
&\quad - \frac{\partial V_j}{\Delta z_k} \sum_{\Omega_{z,m}<0} w_m \Omega_{z,m} \Psi^{bot}_{k,j,m,g,n} = \partial V_j Q_{k,j,g,0} \\
&\quad + \frac{1}{\Delta z_k} \sum_{\Omega_{z,m}>0} w_m \int_{\partial V_j} \mathbf{F} \Omega_{z,m} \psi^{top}_{k-1,m,g}(x,y)\, dA \\
&\quad - \frac{1}{\Delta z_k} \sum_{\Omega_{z,m}<0} w_m \int_{\partial V_j} \mathbf{F} \Omega_{z,m} \psi^{bot}_{k+1,m,g}(x,y)\, dA
\end{aligned} \tag{3.42}$$

This now gives a requirement on the operator $\mathbf{F}$ to preserve neutron balance in the coarse cell, an important feature for both accuracy and effective CMFD acceleration. To preserve neutron balance, the integral of the axial leakage in and out of the coarse cell at the top and bottom surface must equal the axial currents for those surfaces. Recalling the definition of current, this gives the following

requirements for $\mathbf{F}$:

$$\sum_{\Omega_{z,m}>0} w_m \int_{\partial V_j} \mathbf{F}\Omega_{z,m}\psi^{top}_{k-1,m,g}(x,y)\,dA = \partial V_j \sum_{\Omega_{z,m}>0} w_m \Omega_{z,m}\Psi^{top}_{k-1,j,m,g,n} \tag{3.43a}$$

$$\sum_{\Omega_{z,m}<0} w_m \int_{\partial V_j} \mathbf{F}\Omega_{z,m}\psi^{bot}_{k+1,m,g}(x,y)\,dA = \partial V_j \sum_{\Omega_{z,m}<0} w_m \Omega_{z,m}\Psi^{bot}_{k+1,j,m,g,n} \tag{3.43b}$$

If this condition is satisfied, then we can combine like terms and recalling the definition of current yields:

$$\begin{aligned}\Delta y_j(J_{x+,k,j,g} - J_{x-,k,j,g}) + \Delta x_j(J_{y+,k,j,g} - J_{y-,k,j,g}) \\ + \frac{\partial V_j}{\Delta z_k}(J_{z+,k,j,g} - J_{z-,k,j,g}) \\ + \sum_{i_k\in\partial V_j} \partial V_{k,i}\Sigma_{t,k,i,g}\Phi_{k,i,g,0} = \partial V_j Q_{k,j,g,0}\end{aligned} \tag{3.44}$$

Multiplying by Δz_k we can clean this up a bit and get:

$$\begin{aligned}\Delta y_j\Delta z_k(J_{x+,k,j,g} - J_{x-,k,j,g}) + \Delta x_j\Delta z_k(J_{y+,k,j,g} - J_{y-,k,j,g}) \\ + \partial V_j(J_{z+,k,j,g} - J_{z-,k,j,g}) \\ + \sum_{i_k\in\partial V_j} V_{k,i}\Sigma_{t,k,i,g}\Phi_{k,i,g,0} = V_{j,k} Q_{k,j,g,0}\end{aligned} \tag{3.45}$$

Which is the expected neutron balance equation, such that the sum of all net leakage out of the domain and net collisions in the domain, balance exactly with the total source in the domain.

Each of the presented leakage methods in Section 3.2 are here investigated to show adherence to the $\mathbf{F}$ operator requirement. Plugging in Equation 3.30 for the extruded mesh leakage method to the balance condition integral yields:

$$\sum_{\Omega_{z,m}>0} w_m \int_{\partial V_j} \mathbf{F}^{Ext}\Omega_{z,m}\psi^{top}_{k-1,m,g}(x,y)\,dA = \sum_{\Omega_{z,m}>0} w_m \sum_{i_{k-1}\in\partial V_j} \partial V_i \Omega_{z,m} \sum_{n=0}^{N} \Psi_{k-1,i,m,g,n} \tag{3.46a}$$

$$\sum_{\Omega_{z,m}<0} w_m \int_{\partial V_j} \mathbf{F}^{Ext}\Omega_{z,m}\psi^{bot}_{k+1,m,g}(x,y)\,dA = \sum_{\Omega_{z,m}<0} w_m \sum_{i_{k+1}\in\partial V_j} \partial V_i \Omega_{z,m} \sum_{n=0}^{N} (-1)^n \Psi_{k+1,i,m,g,n} \tag{3.46b}$$

which satisfies Equation 3.43 exactly. As such, it is shown that the extruded mesh leakage method preserves neutron balance.

Plugging in Equation 3.33 for the pin cell leakage method to the balance condition integral yields:

$$\sum_{\Omega_{z,m}>0} w_m \int_{\partial V_j} \mathbf{F}^{Pin} \Omega_{z,m} \psi^{top}_{k-1,m,g}(x,y)\, dA = \sum_{\Omega_{z,m}>0} w_m \Omega_{z,m} \sum_{i_{k-1}\in\partial V_j} \partial V_i \sum_{n=0}^{N} \Psi_{k-1,i,m,g,n} \tag{3.47a}$$

$$\sum_{\Omega_{z,m}<0} w_m \int_{\partial V_j} \mathbf{F}^{Pin} \Omega_{z,m} \psi^{bot}_{k+1,m,g}(x,y)\, dA = \sum_{\Omega_{z,m}<0} w_m \Omega_{z,m} \sum_{i_{k+1}\in\partial V_j} \partial V_i \sum_{n=0}^{N} (-1)^n \Psi_{k+1,i,m,g,n} \tag{3.47b}$$

which satisfies Equation 3.43 exactly. As such, it is shown that the pin cell leakage method preserves neutron balance.

Plugging in Equation 3.36 for the pin cell current leakage method to the balance condition integral yields:

$$\sum_{\Omega_{z,m}>0} w_m \int_{\partial V_j} \mathbf{F}^{PinCur} \Omega_{z,m} \psi^{top}_{k-1,m,g}(x,y)\, dA = \sum_{\Omega_{z,m}>0} w_m \frac{1}{2\pi} \sum_{\Omega_{z,m'}>0} \Omega_{z,m'} w_{m'} \sum_{i_{k-1}\in\partial V_j} \partial V_i \sum_{n=0}^{N} \Psi_{k-1,i,m',g,n} \tag{3.48a}$$

$$\sum_{\Omega_{z,m}<0} w_m \int_{\partial V_j} \mathbf{F}^{PinCur} \Omega_{z,m} \psi^{bot}_{k+1,m,g}(x,y)\, dA = \sum_{\Omega_{z,m}<0} w_m \frac{1}{2\pi} \sum_{\Omega_{z,m'}<0} \Omega_{z,m'} w_{m'} \sum_{i_{k+1}\in\partial V_j} \partial V_i \sum_{n=0}^{N} (-1)^n \Psi_{k+1,i,m',g,n} \tag{3.48b}$$

which satisfies Equation 3.43 exactly. As such, it is shown that the pin cell current leakage method preserves neutron balance. It can now be observed that all three methods of axial leakage presented Section 3.2 preserve neutron balance. Further methods of axial leakage may be investigated and applied given that they satisfy Equation 3.43.

3.3 Summary

In this chapter we have formulated the LPAEM. In this formulation we define the axial expansion equations in matrix vector form. Additionally, three methods of axial leakage treatment are introduced. The first of these methods requires axial extrusion of the fine mesh, which can be problematic for systems where different radial meshes may be desired on different axial levels.

The second of these methods preserves angular dependence while requiring only the pin cells be extruded. As such, the fine mesh may vary in each axial layer, so long as the coarse pin cells are axially extruded, a capability already in place in MPACT. The third method also allows fine mesh variation, however the nature of the use of current instead of angular flux does not preserve all angular dependence for the advantage of some memory savings. In the next chapter, some numerical methods for solving the axial expansion equations are investigated.

CHAPTER 4

Numerical Methods for Solving The Legendre Polynomial Axial Expansion Equations

With the formulation of the LPAEM in Chapter 3, it now becomes important to investigate methods for solving it, and inherent performance characteristics of the method.

4.1 1D/1D Equations

Our initial investigation of this method involved applying the principles laid out in section 3.1 to simpler 2D problems mimicking the axial characteristics typical of a traditional LWR. Referred to as *1D/1D*, these problems show method behaviors in a simple testing environment.

For the 1D/1D method, we assume that the system is homogeneous and infinite in the y direction. This means that all variables are independent of the y direction:

$$\Omega_{x,m}\frac{\partial}{\partial x}\bar{\Psi}_{k,m,g}(x)+\bar{\bar{S}}^{down}_{k,m,g}(x)\bar{\Psi}_{k,m,g}(x)=\bar{\mathcal{Q}}^{down}_{k,m,g}(x),\ \forall\,\Omega_{z,m}<0 \tag{4.1}$$

$$\Omega_{x,m}\frac{\partial}{\partial x}\bar{\Psi}_{k,m,g}(x)+\bar{\bar{S}}^{up}_{k,m,g}(x)\bar{\Psi}_{k,m,g}(x)=\bar{\mathcal{Q}}^{up}_{k,m,g}(x),\ \forall\,\Omega_{z,m}>0 \tag{4.2}$$

We will focus the rest of the discussion on the $\Omega_{z,m}>0$ equation since further discussion is easily seen to be analogous and can be translated for the downward moving flux. We can solve the ODE to get:

$$\bar{\Psi}_{k,m,g}(x)=\exp\left(-\int_{x_0}^{x}\frac{\bar{\bar{S}}^{up}_{k,m,g}(x'')}{\Omega_{x,m}}\,dx''\right)\bar{\Psi}_{k,m,g}(x_0)+\int_{x_0}^{x}\frac{1}{\Omega_{x,m}}\exp\left(-\int_{x'}^{x}\frac{\bar{\bar{S}}^{up}_{k,m,g}(x'')}{\Omega_{x,m}}\,dx''\right)\bar{\mathcal{Q}}^{up}_{k,m,g}(x')\,dx' \tag{4.3}$$

Now dividing the system into I_k cells on each slice (where no cell overlaps with multiple regions of

axial leakage indexed by j) we will assume each cell has a spatially flat source and and a constant cross section. This leaves us with equations for boundary flux moments:

$$\bar{\Psi}_{k,i+1/2,m,g} = \exp\left(-\frac{\Delta x_{k,i}}{\Omega_{x,m}}\bar{\bar{S}}^{up}_{k,i,m,g}\right)\bar{\Psi}_{k,i-1/2,m,g} + \left(\bar{\bar{S}}^{up}_{k,i,m,g}\right)^{-1}\left[\bar{\bar{I}} - \exp\left(-\frac{\Delta x_{k,i}}{\Omega_{x,m}}\bar{\bar{S}}^{up}_{k,i,m,g}\right)\right]\bar{\mathcal{Q}}^{up}_{k,i,m,g},\ \forall\,\Omega_{x,m} > 0 \quad (4.4)$$

$$\bar{\Psi}_{k,i-1/2,m,g} = \exp\left(\frac{\Delta x_{k,i}}{\Omega_{x,m}}\bar{\bar{S}}^{up}_{k,i,m,g}\right)\bar{\Psi}_{k,i+1/2,m,g} + \left(\bar{\bar{S}}^{up}_{k,i,m,g}\right)^{-1}\left[\bar{\bar{I}} - \exp\left(\frac{\Delta x_{k,i}}{\Omega_{x,m}}\bar{\bar{S}}^{up}_{k,i,m,g}\right)\right]\bar{\mathcal{Q}}^{up}_{k,i,m,g},\ \forall\,\Omega_{x,m} < 0 \quad (4.5)$$

And an equation for the cell integrated flux moments:

$$\bar{\Psi}_{k,i,m,g} = \Omega_{x,m}\left(\bar{\bar{S}}^{up}_{k,i,m,g}\right)^{-1}\left(\bar{\Psi}_{k,i-1/2,m,g} - \bar{\Psi}_{k,i+1/2,m,g}\right) + \Delta x_{k,i}\left(\bar{\bar{S}}^{up}_{k,i,m,g}\right)^{-1}\bar{\mathcal{Q}}^{up}_{k,i,m,g} \quad (4.6)$$

4.2 2D/1D MOC Equations

We start with the 2D equations and again just consider upward moving neutrons for purposes of the derivation.

$$\Omega_{x,m}\frac{\partial}{\partial x}\bar{\Psi}_{k,m,g}(x,y) + \Omega_{y,m}\frac{\partial}{\partial y}\bar{\Psi}_{k,m,g}(x,y) + \bar{\bar{S}}^{up}_{k,m,g}(x,y)\bar{\Psi}_{k,m,g}(x,y) = \bar{\mathcal{Q}}^{up}_{k,m,g}(x,y), \quad \forall\,\Omega_{z,m} > 0 \quad (4.7)$$

Now we know that by convention we consider

$$\hat{\Omega} = (\Omega_x, \Omega_y, \Omega_z) = (\sqrt{1-\mu^2}\cos\omega, \sqrt{1-\mu^2}\sin\omega, \mu) \quad (4.8)$$

where μ is the polar cosine ($-1 \leq \mu \leq 1$) and ω is the azimuthal angle ($0 \leq \omega < 2\pi$). So for a product quadrature angular discretization, we use the variable s to denote the total distance traveled along a 2D characteristic line $\boldsymbol{r} = (x, y)$ for a given 2D angular direction $\hat{\Omega}^r = (\Omega^r_x, \Omega^r_y) = (\cos\omega, \sin\omega)$:

$$\boldsymbol{r} = \boldsymbol{r}_0 + s\hat{\Omega}^r \quad (4.9)$$

Where $\boldsymbol{r}_0$ is the starting point of the line. So that now:

$$x = x_0 + s\Omega_x^r \Rightarrow \frac{\partial x}{\partial s} = \Omega_x^r \tag{4.10}$$

$$y = y_0 + s\Omega_y^r \Rightarrow \frac{\partial y}{\partial s} = \Omega_y^r \tag{4.11}$$

So that the 2D gradient is now:

$$\frac{df}{ds} = \frac{\partial x}{\partial s}\frac{\partial f}{\partial x} + \frac{\partial y}{\partial s}\frac{\partial f}{\partial y} = \Omega_x^r \frac{\partial f}{\partial x} + \Omega_y^r \frac{\partial f}{\partial y} \tag{4.12}$$

So now we have the ODE:

$$\frac{d}{ds}\bar{\Psi}_{k,m,g}(x_0 + s\Omega_x^r, y_0 + s\Omega_y^r) + \frac{\bar{\bar{S}}_{k,m,g}^{up}(x_0 + s\Omega_x^r, y_0 + s\Omega_y^r)}{\sqrt{1-\mu^2}}\bar{\Psi}_{k,m,g}(x_0 + s\Omega_x^r, y_0 + s\Omega_y^r)$$
$$= \frac{\bar{\mathcal{Q}}_{k,m,g}^{up}(x_0 + s\Omega_x^r, y_0 + s\Omega_y^r)}{\sqrt{1-\mu^2}}, \quad \forall\, \Omega_{z,m} > 0 \tag{4.13}$$

So we recognize that this is now just a function of s:

$$\frac{d}{ds}\bar{\Psi}_{k,m,g}(s) + \frac{\bar{\bar{S}}_{k,m,g}^{up}(s)}{\sqrt{1-\mu^2}}\bar{\Psi}_{k,m,g}(s) = \frac{\bar{\mathcal{Q}}_{k,m,g}^{up}(s)}{\sqrt{1-\mu^2}}, \quad \forall\, \Omega_{z,m} > 0 \tag{4.14}$$

Which we take an integrating factor with to get:

$$\frac{d}{ds'}\left[\exp\left(\frac{\int_{s_0}^{s'} \bar{\bar{S}}_{k,m,g}^{up}(s'')\, ds''}{\sqrt{1-\mu^2}}\right)\bar{\Psi}_{k,m,g}(s')\right]$$
$$= \exp\left(\frac{\int_{s_0}^{s'} \bar{\bar{S}}_{k,m,g}^{up}(s'')\, ds''}{\sqrt{1-\mu^2}}\right)\frac{\bar{\mathcal{Q}}_{k,m,g}^{up}(s')}{\sqrt{1-\mu^2}}, \quad \forall\, \Omega_{z,m} > 0 \tag{4.15}$$

We then integrate over s' from s_0 to s:

$$\int_{s_0}^{s} \frac{d}{ds'}\left[\exp\left(\frac{\int_{s_0}^{s'} \bar{\bar{S}}_{k,m,g}^{up}(s'')\, ds''}{\sqrt{1-\mu^2}}\right)\bar{\Psi}_{k,m,g}(s')\right] ds'$$
$$= \int_{s_0}^{s} \exp\left(\frac{\int_{s_0}^{s'} \bar{\bar{S}}_{k,m,g}^{up}(s'')\, ds''}{\sqrt{1-\mu^2}}\right)\frac{\bar{\mathcal{Q}}_{k,m,g}^{up}(s')}{\sqrt{1-\mu^2}}\, ds', \quad \forall\, \Omega_{z,m} > 0 \tag{4.16}$$

So that from the fundamental theorem of calculus, we can get:

$$\bar{\Psi}_{k,m,g}(s) = \exp\left(-\frac{\int_{s_0}^{s} \bar{\bar{S}}^{up}_{k,m,g}(s'')\,ds''}{\sqrt{1-\mu^2}}\right)\bar{\Psi}_{k,m,g}(s_0)$$
$$+ \exp\left(-\frac{\int_{s_0}^{s} \bar{\bar{S}}^{up}_{k,m,g}(s'')\,ds''}{\sqrt{1-\mu^2}}\right)\int_{s_0}^{s}\exp\left(\frac{\int_{s_0}^{s'} \bar{\bar{S}}^{up}_{k,m,g}(s'')\,ds''}{\sqrt{1-\mu^2}}\right)\frac{\bar{\mathcal{Q}}^{up}_{k,m,g}(s')}{\sqrt{1-\mu^2}}\,ds', \quad \forall\,\Omega_{z,m} > 0 \quad (4.17)$$

But the first exponential from the left in the source term is independent of s' so it can be moved inside of the integral to give:

$$\bar{\Psi}_{k,m,g}(s) = \exp\left(-\frac{\int_{s_0}^{s} \bar{\bar{S}}^{up}_{k,m,g}(s'')\,ds''}{\sqrt{1-\mu^2}}\right)\bar{\Psi}_{k,m,g}(s_0)$$
$$+ \int_{s_0}^{s}\exp\left(-\frac{\int_{s'}^{s} \bar{\bar{S}}^{up}_{k,m,g}(s'')\,ds''}{\sqrt{1-\mu^2}}\right)\frac{\bar{\mathcal{Q}}^{up}_{k,m,g}(s')}{\sqrt{1-\mu^2}}\,ds', \quad \forall\,\Omega_{z,m} > 0 \quad (4.18)$$

We now divide the characteristic line up into discrete segments, where each segment is in a discrete radial region, indexed $i = 1, 2, \ldots, I$, where we treat both the cross sections and the sources as spatially invariant. We take $s = s_{out}$ to now be the position on the line where it exits the region, and $s_0 = s_{in}$ to be the position on the line where it enters, so that the total distance traveled in the region by the line is $\Delta s = s_{out} - s_{in}$ This now leads to the following:

$$\bar{\Psi}_{k,m,g,out} = \exp\left(-\frac{\bar{\bar{S}}^{up}_{k,i,m,g}\Delta s}{\sqrt{1-\mu^2}}\right)\bar{\Psi}_{k,m,g,in}$$
$$+ \left(\bar{\bar{S}}^{up}_{k,i,m,g}\right)^{-1}\left[\bar{\bar{I}} - \exp\left(-\frac{\bar{\bar{S}}^{up}_{k,i,m,g}\Delta s}{\sqrt{1-\mu^2}}\right)\right]\bar{\mathcal{Q}}^{up}_{k,i,m,g}, \quad \forall\,\Omega_{z,m} > 0 \quad (4.19)$$

and similarly for downward traveling flux

$$\bar{\Psi}_{k,m,g,out} = \exp\left(-\frac{\bar{\bar{S}}^{down}_{k,i,m,g}\Delta s}{\sqrt{1-\mu^2}}\right)\bar{\Psi}_{k,m,g,in}$$
$$+ \left(\bar{\bar{S}}^{down}_{k,i,m,g}\right)^{-1}\left[\bar{\bar{I}} - \exp\left(-\frac{\bar{\bar{S}}^{down}_{k,i,m,g}\Delta s}{\sqrt{1-\mu^2}}\right)\right]\bar{\mathcal{Q}}^{down}_{k,i,m,g}, \quad \forall\,\Omega_{z,m} < 0 \quad (4.20)$$

We will also integrate Eq. 4.18 over the segment to get the segment integrated flux moments:

$$\bar{\Psi}_{k,m,g,int} = \left(\frac{\bar{\bar{S}}^{up}_{k,i,m,g}}{\sqrt{1-\mu^2}}\right)^{-1}\left[\bar{\bar{I}} - \exp\left(-\frac{\bar{\bar{S}}^{up}_{k,i,m,g}\Delta s}{\sqrt{1-\mu^2}}\right)\right]\bar{\Psi}_{k,m,g,in}$$
$$+\left(\frac{\bar{\bar{S}}^{up}_{k,i,m,g}}{\sqrt{1-\mu^2}}\right)^{-1}\left[\bar{\bar{I}}\Delta s - \left(\frac{\bar{\bar{S}}^{up}_{k,i,m,g}}{\sqrt{1-\mu^2}}\right)^{-1}\left[\bar{\bar{I}} - \exp\left(-\frac{\bar{\bar{S}}^{up}_{k,i,m,g}\Delta s}{\sqrt{1-\mu^2}}\right)\right]\right]\frac{\bar{\mathcal{Q}}^{up}_{k,i,m,g}}{\sqrt{1-\mu^2}}, \quad \forall\,\Omega_{z,m} > 0 \tag{4.21}$$

We can rearrange and plug in the definition of $\bar{\Psi}_{k,m,g,out}$ to get:

$$\bar{\Psi}_{k,m,g,int} = \left(\frac{\bar{\bar{S}}^{up}_{k,i,m,g}}{\sqrt{1-\mu^2}}\right)^{-1}\bar{\Psi}_{k,m,g,in} + \Delta s\left(\frac{\bar{\bar{S}}^{up}_{k,i,m,g}}{\sqrt{1-\mu^2}}\right)^{-1}\frac{\bar{\mathcal{Q}}^{up}_{k,i,m,g}}{\sqrt{1-\mu^2}}$$
$$-\left(\frac{\bar{\bar{S}}^{up}_{k,i,m,g}}{\sqrt{1-\mu^2}}\right)^{-1}\bar{\Psi}_{k,m,g,out}, \quad \forall\,\Omega_{z,m} > 0 \tag{4.22}$$

Which can be rearranged to give:

$$\bar{\Psi}_{k,m,g,int} = \left(\frac{\bar{\bar{S}}^{up}_{k,i,m,g}}{\sqrt{1-\mu^2}}\right)^{-1}\left[\bar{\Psi}_{k,m,g,in} - \bar{\Psi}_{k,m,g,out} + \Delta s\frac{\bar{\mathcal{Q}}^{up}_{k,i,m,g}}{\sqrt{1-\mu^2}}\right], \quad \forall\,\Omega_{z,m} > 0 \tag{4.23}$$

and similarly for downward traveling flux

$$\bar{\Psi}_{k,m,g,int} = \left(\frac{\bar{\bar{S}}^{down}_{k,i,m,g}}{\sqrt{1-\mu^2}}\right)^{-1}\left[\bar{\Psi}_{k,m,g,in} - \bar{\Psi}_{k,m,g,out} + \Delta s\frac{\bar{\mathcal{Q}}^{down}_{k,i,m,g}}{\sqrt{1-\mu^2}}\right], \quad \forall\,\Omega_{z,m} < 0 \tag{4.24}$$

4.3 CMFD Linkage

To link the CMFD implementation in MPACT with the axial expansion transport solution requires communication of the scalar flux and current between the two solvers. The iterates of the fine mesh scalar flux is passed to the CMFD solver as the 0th axial moment scalar flux. The radial currents on the coarse mesh are similarly computed using the 0th axial moment flux at the coarse mesh cell boundaries. So that the net radial current for the cell boundary between pin cells j and j' across surface p in plane k is

$$J^{net,rad}_{k,g,p} = \sum_m \hat{n}_p \cdot \hat{\Omega}_m w_m \Psi_{k,j,m,g,0} + \sum_m \hat{n}_p \cdot \hat{\Omega}_m w_m \Psi_{k,j',m,g,0} \tag{4.25}$$

Where $\hat{n}_p$ is the unit normal vector to surface p between the two coarse cells.

For the net axial current, the solution is taken at the top and bottom of the pin cell j in planes k and $k+1$ for horizontal surface p.

$$J^{net,ax}_{j,g,p} = \sum_m \Omega_{z,m} w_m \sum_{n=0}^{N} \Psi_{k,j,m,g,n} + \sum_m \Omega_{z,m} w_m \sum_{n=0}^{N} (-1)^n \Psi_{k+1,j,m,g,0} \tag{4.26}$$

Once the CMFD equation is solved, the solution is projected back onto the fine mesh transport problem. This projection is done identically for each axial moment to insure that the relative axial variation is preserved in the CMFD acceleration. So for iteration l in the MOC solution, the updated flux moments for fine cells i in coarse cell j become:

$$\Phi^{l}_{k,i,g,n} = \Phi^{l-1/2}_{k,i,g,n} \frac{\phi^{l}_{k,j,g}}{\phi^{l-1/2}_{k,j,g}},\ i \in j \tag{4.27}$$

Since the axial leakage is best accumulated in the transport sweep, the leakage must also be projected at this time since it will not inherit the projection of the flux. The projection must be done so that the cell that provides the axial leakage is the one doing the projection. This means that for downward moving leakage it is:

$$TL^{down,l}_{k,j,m,g} = TL^{down,l-1/2}_{k,j,m,g} \frac{\phi^{l}_{k+1,j,g}}{\phi^{l-1/2}_{k+1,j,g}} \tag{4.28}$$

And similarly for upward moving leakage:

$$TL^{up,l}_{k,j,m,g} = TL^{up,l-1/2}_{k,j,m,g} \frac{\phi^{l}_{k-1,j,g}}{\phi^{l-1/2}_{k-1,j,g}} \tag{4.29}$$

4.4 Matrix Exponential Lookup Tables

LPAEM presents the relatively rare problem of needing to compute matrix exponentials. Indeed, the computation of these exponentials represents perhaps the most computationally expensive part of this calculation, having to be performed in the innermost loop for every single ray segment and energy group. While a large degree of research has been done into the computation of matrix exponentials [70] [71] [72], their actual evaluation can still be quite expensive, especially beyond 3×3 sized matrices, where cheap and general analytic solutions are not known. For that reason, many matrix exponential calculations rely on iterative methods such as Padé approximations [73]. While these methods can be relatively fast, they are still quite slow in comparison to scalar exponential calculations.

However, the matrices that have their exponentials computed for this problem take on particular

forms that can be separated to vary by scalar variables. As such, the exponentials can be formulated in such a way that a set of matrix exponential tables may be formed, allowing the computation of matrix exponentials to be pre-calculated and then quickly looked up and interpolated using the pre-computed tables. This represents a substantial improvement in implementation speed and performance and a drastic improvement in matrix exponential cost scaling that could allow for much higher order polynomial approximations to be used by the method.

First, the definition of a matrix exponential is given by the convergent power series:

$$\exp\left(\bar{\bar{A}}\right) = \sum_{l=0}^{\infty} \frac{\bar{\bar{A}}^l}{l!} \tag{4.30}$$

We consider only the matrices from the up moving equations since the concept will be identical for the downward moving equations. Considering Eq. 3.26h and Eq. 4.19, the matrix exponential takes the form:

$$\exp\left(-\frac{\bar{\bar{S}}^{up}}{\sqrt{1-\mu^2}}\Delta s\right) \tag{4.31}$$

Where the S matrix is:

$$\bar{\bar{S}}^{up} = \frac{\mu}{\Delta z}\bar{\bar{C}}^{up} + \Sigma_t \bar{\bar{I}} \tag{4.32}$$

So let us now define:

$$\gamma = -\frac{\mu \Delta s}{\Delta z\sqrt{1-\mu^2}} \tag{4.33}$$

$$\zeta = -\frac{\Sigma_t \Delta s}{\sqrt{1-\mu^2}} \tag{4.34}$$

Then the matrix exponential now can be expressed as:

$$\exp\left(-\frac{\bar{\bar{S}}^{up}}{\sqrt{1-\mu^2}}\Delta s\right) = \exp\left(\gamma\bar{\bar{C}}^{up} + \zeta\bar{\bar{I}}\right) \tag{4.35}$$

But notice that the final matrix is the identity matrix, so it is commutative with all other matrices. Now if two matrices are commutative then it can be seen from the power series definition that the exponential can be split in a manner identical to scalar exponentials. So we get:

$$\exp\left(-\frac{\bar{\bar{S}}^{up}}{\sqrt{1-\mu^2}}\Delta s\right) = e^{\gamma\bar{\bar{C}}^{up}} e^{\zeta\bar{\bar{I}}} \tag{4.36}$$

First, notice that the fact that the second matrix is a matrix exponential of a factor of the identity matrix, then it will simply be the diagonal matrix where every diagonal term is e^{ζ} so we can pull

that factor out and treat it as a scalar to avoid some matrix-matrix multiplication:

$$e^{\zeta} e^{\gamma \bar{\bar{C}}^{up}} \tag{4.37}$$

Now consider γ_1 and γ_2 such that $\gamma_1 - \gamma_2 \sim \epsilon$. Then we see:

$$e^{(\gamma_1-\gamma_2)\bar{\bar{C}}^{up}} = \sum_{k=0}^{\infty} \frac{(\gamma_1-\gamma_2)^k}{k!} \left(\bar{\bar{C}}^{up}\right)^k \tag{4.38}$$

If $\epsilon \ll 1$ then we see that the importance of the terms geometrically decreases so that we can ignore high order terms to get:

$$e^{\gamma_1 \bar{\bar{C}}^{up}} e^{-\gamma_2 \bar{\bar{C}}^{up}} \approx \bar{\bar{I}} + (\gamma_1 - \gamma_2)\bar{\bar{C}}^{up} \Rightarrow e^{\gamma_1 \bar{\bar{C}}^{up}} \approx e^{\gamma_2 \bar{\bar{C}}^{up}} + (\gamma_1 - \gamma_2)\bar{\bar{C}}^{up} e^{\gamma_2 \bar{\bar{C}}^{up}} \tag{4.39}$$

So if we have already determined the matrix $e^{\gamma_2 \bar{\bar{C}}^{up}}$ and $\bar{\bar{C}}^{up} e^{\gamma_2 \bar{\bar{C}}^{up}}$ then we can do a linear calculation and matrix addition to compute an approximation to $e^{\gamma_1 \bar{\bar{C}}^{up}}$. This prompts us to create a table of matrix exponentials for varying values of γ_i associated with $e^{\gamma_i \bar{\bar{C}}^{up}}$ and $\bar{\bar{C}}^{up} e^{\gamma_i \bar{\bar{C}}^{up}}$ that is used in the sweep to give the desired matrix exponentials at a fraction of the cost of computing those same matrix exponentials using traditional methods. Additionally, this innovation precludes the need for further research into efficient methods of computing matrix exponentials for this method, since the computation of the matrix exponential tables is front-loaded and computationally inexpensive.

For the actual implementation of the matrix exponential tables in MPACT, the minimum and maximum value of the unitless variable γ is computed for the given problem. Investigating γ, we see that it will be symmetric due to the symmetric nature of angular quadrature sets. That is to say, for every direction m in a quadrature set, there will be some m' such that $\omega_m = \omega_{m'}$ and $\mu_m = -\mu_{m'}$. This means that the minimum value of γ will be the negative of the maximum value of γ. Furthermore, γ is the multiple of the two ratios $\frac{\mu}{\sqrt{1-\mu^2}}$ and $\frac{\Delta s}{\Delta z}$. Now, $\left|\frac{\mu}{\sqrt{1-\mu^2}}\right|$ is less than 1 unless $|\mu| \geq \frac{1}{\sqrt{2}}$ and will still be small unless $|\mu|$ is close to 1. For most angular quadrature sets used in reactor physics problems this ratio stays small. Additionally, $\left|\frac{\Delta s}{\Delta z}\right|$ is typically less than 1 since slice sizes are normally around 10 cm whereas most segment lengths are much shorter than 1 cm. As such, the upper bound for $|\gamma|$ will be much less than 1 in most reactor physics problems.

Once the bounds of γ have been computed, the bounds are rounded up to the next integer, typically 1. Following this, a uniform grid of points, indexed i here, between the two integers is made, each 0.0001 away from each other. This spacing was determined by comparing the accuracy of the linear interpolation halfway between the grid points and a 12th order Padé approximation of that exponential. The sufficient accuracy was determined such that it would be similar that of the difference between a 6th order and 12th order Padé approximation, since 6th order Padé

approximations are typically considered to be of sufficient accuracy in general matrix exponential calculations. Once the grid spacing is set, the values of $e^{\gamma_i \bar{\bar{C}}^{up}}$ and $\bar{\bar{C}}^{up} e^{\gamma_i \bar{\bar{C}}^{up}}$ are computed for each positive grid point, and the values of $e^{\gamma_i \bar{\bar{C}}^{down}}$ and $\bar{\bar{C}}^{up} e^{\gamma_i \bar{\bar{C}}^{down}}$ are computed for each negative grid point. These grid point matrix exponentials are computed using a 12th order Padé approximation. Notice that $e^{0\bar{\bar{C}}^{up}} = e^{0\bar{\bar{C}}^{down}} = \bar{\bar{I}}$.

The tables for ζ were similarly constructed using an identical grid, but ranging from 0 to the minimum computed value since ζ is universally negative. Optical thickness of a ray segment, $\Sigma_t \Delta s$, is typically much less than 1 in most reactor physics meshes. Additionally, $\frac{1}{\sqrt{1-\mu^2}}$ is relatively small except for values of $|\mu|$ near 1, which is uncommon in angular quadrature sets. As such, the minimum value of ζ is often above -1. The creation and use of these tables is identical to the matrix exponential tables except for scalar exponentials instead of matrix exponentials.

With the tables now made, in the axial expansion sweep γ and ζ is computed for each segment and the associated matrix exponential is linearly interpolated with the nearest grid point, γ_i, as described in Equation 4.39. Similarly, the ζ exponential is also computed using the nearest grid point, $\zeta_{i'}$, and the interpolated matrix exponential is multiplied by the resulting scalar to give the complete matrix exponential table calculation of $\exp\left(-\frac{\bar{\bar{S}}^{up}}{\sqrt{1-\mu^2}}\Delta s\right)$ or $\exp\left(-\frac{\bar{\bar{S}}^{down}}{\sqrt{1-\mu^2}}\Delta s\right)$.

Track Renormalization Investigation

During the implementation phase of this method, some investigation was made into the consistency of the "seen" area of a FSR, that is to say the sum of ray segment areas (ray spacing width multiplied by segment length) for a given discrete angle, with the known FSR area. This investigation led to the observation that if ray spacing was too large, a non-negligible discrepancy between angularly seen area and true area could occur. To fix this, a renormalization area was pre-computed for each FSR in each direction. This area was used to correct the relative amount of source contribution compared to material and geometric attenuation in the matrix exponential for each angle in a given FSR. Unfortunately, application of this correction introduced inconsistencies in the neutron balance of the calculation. These inconsistencies added instability to the calculation particularly when attempting to couple it with CMFD. Additionally, it was determined that for most typical ray spacings used in reactor physics problems, that the "seen" area was relatively close to the true area. As such, no track renormalization is currently used in the MPACT implementation of the axial expansion method.

Since the implementation relies on MPACT's ray tracing, the track renormalization capabilities of MPACT's modular ray tracing calculation can be utilized by the axial expansion method in MPACT. However, no track renormalization is currently the default method for the LPAEM in MPACT and those renormalization's effects on the method have yet to be thoroughly explored.

4.5 Memory Usage Analysis

Memory usage is one of the primary computational concerns in solving neutron transport problems. Even if a method of solving the system is efficient with respect to solution time, if it is expensive in terms of memory usage it may not be usable for large problems. To determine the memory cost of this method, analysis was performed to estimate the memory usage of the primary memory contributing terms for the method beyond the standard memory required by traditional 2D/1D methods.

For a general problem, the primary memory scaling factors for axial expansion specific terms are as follows:

1. N_{FSR} - Number of FSRs
2. N_{PC} - Number of pin cells
3. K - Number of axial slices
4. N_G - Number of energy groups
5. N_p - Number of polar angles
6. N_a - Number of azimuthal angles
7. N_{SegMax} - Maximum number of segments in a modular ray
8. N_{RadFSR} - Maximum number of radial FSRs
9. N_{surf} - Number of coarse mesh surfaces
10. N_{rays} - Number of rays
11. N_{poly} - Number of axial Legendre polynomials

These factors then are components of the primary additional memory added by the axial expansion method. In Table 4.1 the functional forms of the largest additional memory terms are recorded. Additionally, the added memory for the small 9×9 fuel array detailed in Section 5.2.2 is both computed and the full increase recorded for a run with $N_{poly} = 2$.

Component	Function	9×9 Array Memory [MB]
Radial Boundary Values	$2KN_GN_pN_{rays}N_{poly}$	250
Leakage Incremental Source	$8N_GN_pN_aN_{RadFSR}N_{poly}$	40.9
Sweep Leakage Accumulation	$8N_GN_pN_aN_{RadFSR}N_{poly}$	13.6
Axial Leakage	$16KN_{PC}N_GN_pN_a$	8.86
Sweep Computed Matrices	$4N_GN_pN_aN_{RadFSR}N_{poly}^2$	3.83
Matrix Exponential Tables	$20000N_{poly}^2$	1.37
Sweep Intermediate Flux	$4N_GN_pN_{RadFSR}N_{poly}$	1.28
Stored Source	$N_{FSR}N_GN_{poly}$	0.807
Scalar Flux	$N_{FSR}N_GN_{poly}$	0.807
Sweeper Source	$N_{FSR}N_GN_{poly}$	0.807
Sweep Exponent Matrices	$N_GN_pN_{SegMax}N_{poly}^2$	0.227
Sweep Surface Flux	$2N_GN_{surf}$	0.0644
Sweep FSR Flux	$N_GN_{RadFSR}N_{poly}$	0.0532
Sweep Segment Flux	$N_G(N_{SegMax}+1)N_{poly}$	0.0256
Percent Additional Memory	N/A	195.21%

Table 4.1: Memory Analysis.

It can be observed in Table 4.1 that the bulk of the memory increase comes from the radial boundary storage. Because the ray boundary values must be stored for each axial moment, there is unfortunately no real way to mitigate this. Unfortunately, it does appear that the axial expansion method requires significantly more memory than traditional transport. However, one positive thing to note is that the matrix exponential tables are relatively cheap with respect to memory, and scale only with number of axial moments, independent of problem size.

Alternatively, using the FSR extruded leakage, which was not implemented in MPACT but was investigated in the 1D/1D exploratory code, the axial leakage term becomes $16N_{FSR}N_GN_pN_a$. With this formulation, the memory usage for the axial leakage term in the 9×9 array increases to 413 MB, which would be nearly 50 times the memory usage found in the pin cell averaged implementation and make it the largest single source of additional memory introduced by the axial expansion method. Fortunately, analysis in Section 5.1.1 reveals that FSR extruded leakage provides minimal benefits in terms of accuracy.

4.6 Summary

In this chapter we investigated a number of numerical aspects and methods for solving the LPAEM. 1D/1D equations were derived and similarly MOC was applied to the full 3D axial expansion equations to provide an algebraic set of equations for the axial expansion method. The requisite linkage with CMFD was introduced including the necessary projection of the coarse mesh leakage. Matrix exponential lookup tables are also introduced and formed in such a manner that they can be used for this method. Finally, memory usage of the method is introduced and analyzed for a small array of pin cells. The next chapter describes some of the computational campaigns performed using the axial expansion method and their results.

CHAPTER 5

Method Demonstration and Numerical Results

5.1 1D/1D Demonstrations

To demonstrate the method's capabilities, limitations, and correctness, it is useful to start with investigations involving 2D systems with axial characteristics similar to those in an LWR. These tests capture some of the fundamental behaviors of the method, but must be necessarily limited in their demonstrative capabilities by the lack of y direction radial variability. As such, these investigations, whether performed using an exploratory code or using the full implementation in MPACT, can serve to demonstrate useful characteristics of the method but need to be followed up on with full 3D problems.

5.1.1 Exploratory Code Demonstration

These demonstrations took place using an exploratory code explicitly implemented for the 1D/1D method described in Section 4.1. The code was written in modern Fortran and made use of multi-threading for parallelism. This section describes the primary models run in this exploratory code. All future sections involving 1D/1D models involve computations performed using the full axial expansion method implemented in MPACT.

The basis of the exploratory code test problem designs is an assembly of six pairs of fuel slabs, each surrounded by moderator on both sides. At the center there is a fission chamber surrounded by alternating fuel and guide tubes where each guide tube is separated by two slabs of fuel.

1. The first pair is separated from the second by a guide tube.
2. The second pair is separated from the third by another guide tube.
3. The third pair is separated from the fourth by a fission chamber
4. The fourth pair is separated from the fifth by another guide tube.

5. The fifth pair is separated from the sixth by another guide tube.

Control rods replace the guide tubes in the design in some problems. The assembly is then surrounded above, below, and on both sides by moderators. The design is made to mimic some aspects of the traditional test problem C5G7 [68]. The cross sections of the system are those of the 3D C5G7 problem.

Four variations on the test problem are used. The first two variations are axially and radially symmetric all rods out (ARO) and all rods in (ARI) configurations. These configurations are shown in Figure 5.1.

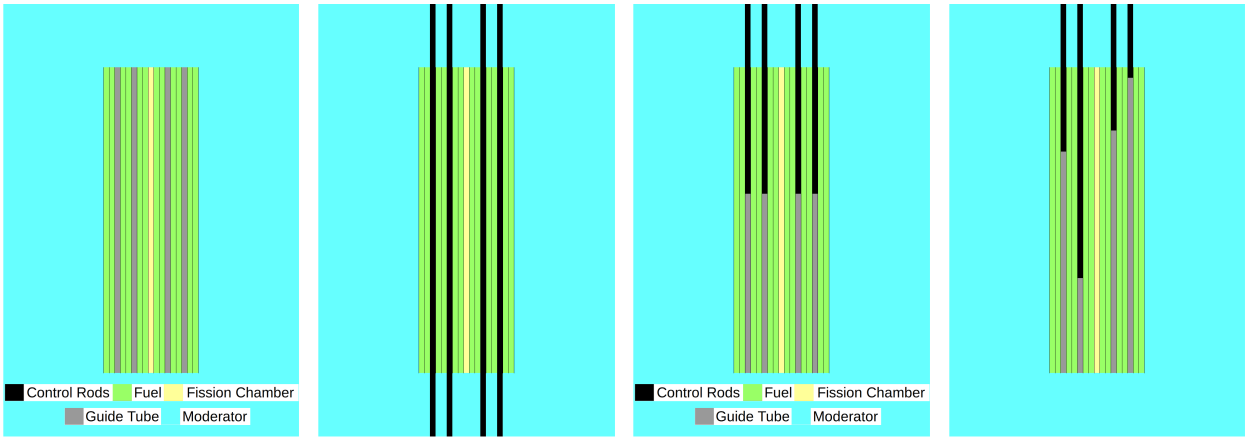

ARO. ARI. RSAARI. RAAARI.

Figure 5.1: Symmetric assembly configurations.

The third configuration is the radially symmetric but axially asymmetric rod insertion (RSAARI). The fourth configuration features a radially asymmetric and axially asymmetric rod insertion (RAAARI). These configurations are both shown in Figure 5.1.

The meshes are identical for all configurations and are extruded, but need not be since the method requires extruded coarse pins, not extruded meshes. The extrusion allows comparison of pin leakage to cell leakage on identical meshes.

The meshes had slice heights of 3.57 cm and pin cell widths of 1.87 cm. An important note is that all configurations ran for a case where a single slice 100 times thinner is inserted into the interior of the reactor configuration; in this case, MPACT's 2D/1D calculation failed to converge, but the axial expansion calculation did converge.

Reference calculations for this testing were performed by laying the system on its side and performing an ultra-fine mesh 2D MPACT calculation. The 1D/1D calculations for these tests were performed on a small independent code written specifically for this initial testing.

A comparison of the global eigenvalue errors is shown in Table 5.1.

Solver/Case	ARO	ARI	RSAARI	RAAARI
Ref 2D MPACT k_{eff}	1.03528	0.63391	0.99988	0.96280
MPACT 1D/1D	-93	-433	-116	-206
Pin Cell Leakage N=4	-16	-398	17	-47
FSR Leakage N=4	-32	-179	-6	-31

Table 5.1: Eigenvalues and eigenvalue errors in [pcm].

The eigenvalue errors are smaller when using the axial expansion methods than when using MPACT's current axial approximation. The ARI case seems to be an outlier in terms of eigenvalue errors for all three methods. This may be because this case is the only case that is more than 10,000 pcm away from criticality so that smaller relative errors in difference from the criticality will result in larger absolute errors. Ignoring this outlier, the pin and cell leakage errors in cases in which the system is fairly close to critical are nearly identical and are both more than five times smaller than the error from MPACT's approximation.

A plot of eigenvalue error progression vs. the order of axial polynomial expansion is shown in Figure 5.2.

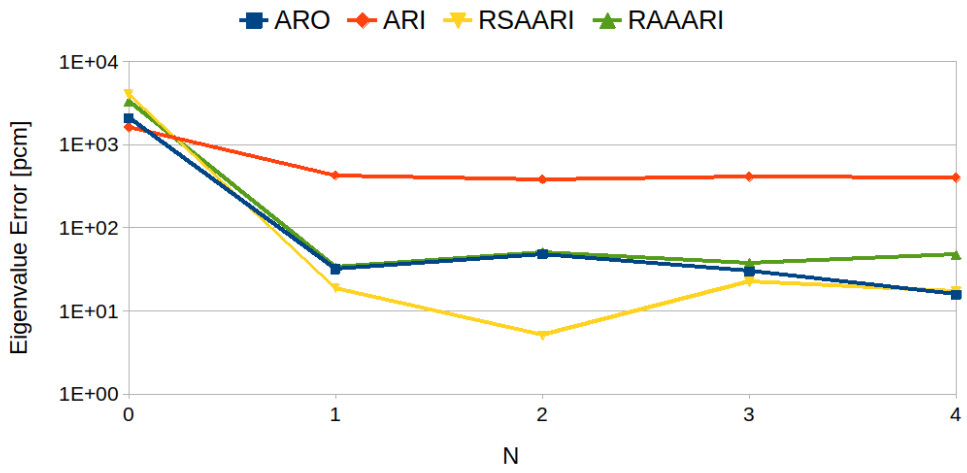

Figure 5.2: Legendre order effect on eigenvalue error.

The linear approximation appears good, and higher order approximations seem to have little improvement on eigenvalue errors for these problems.

Fast and thermal flux profiles from the reference calculation for the RAAARI case are shown in Figure 5.3.

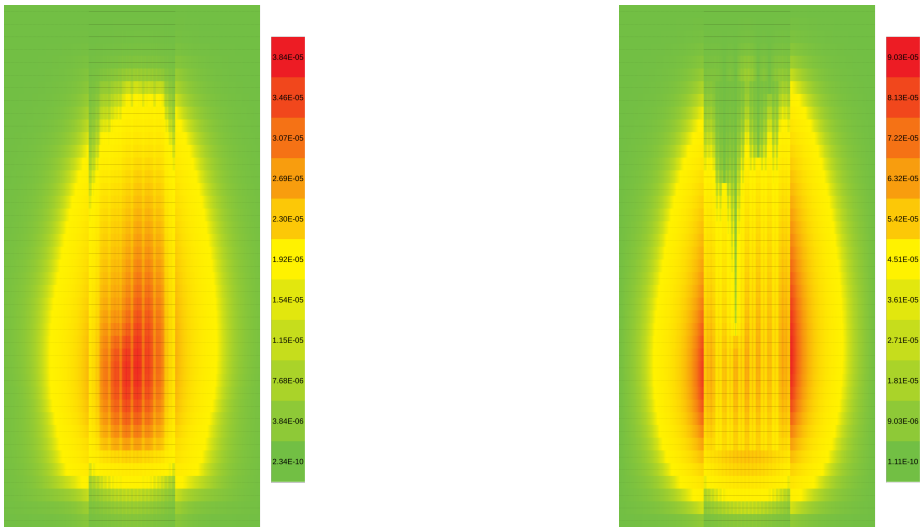

Group 1 flux. Group 7 flux.

Figure 5.3: Asymmetric insertion (RAAARI) flux profiles.

The asymmetry of the flux profiles is on display, and sudden flux gradients are much more noticeable in the thermal flux than in the fast flux, likely due to the large poisoning effect that control rod materials have on thermal flux.

Figure 5.4 shows a comparison of the errors from the reference of the axial local pin power profiles for the fourth fuel pin in the asymmetric insertion (i.e., the fuel pin immediately to the left of the longest inserted control rod) for the three calculation methods. This pin was chosen because it was determined to be the most abnormal and sharply changing of the fuel pins, as shown in Figure 5.3, making it the most likely candidate for noticeable errors coming from axial approximations.

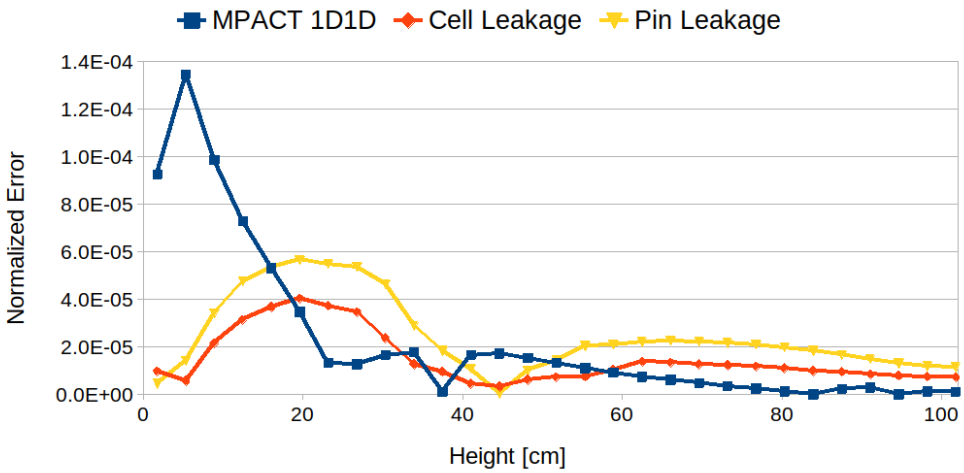

Figure 5.4: RAARI fuel pin four power profile errors.

The cell and pin leakage calculations are both performed for the case in which the Legendre polynomial expansion uses $N = 4$. So, the matrices used for the transport system are 5×5, and the vectors similarly have a length of five. Although the MPACT axial approximation has lower error across a longer portion of the axial profile, the areas of largest error are much larger than those found in the axial expansion approximation. Additionally, this area of highest error is lower on the axial length, which is the location at which the flux is much higher for this configuration (Figure 5.3) and at which the local accuracy plays a much more important role in bulk system behavior. Although the cell-leakage method shows lower local errors than the pin-leakage method, the error bears roughly the same shape in both situations.

5.1.2 Thin Slice Stability Demonstration

Over the course of the implementation, a number of regression tests were created in order to determine robustness of the method in various circumstances. Some of these tests included thin axial slices for an axially thin problem to prove the ability of the method to converge in such circumstances. As mentioned in Section 1.2.1, traditional 2D/1D methods can have instability in such systems so this can provide a useful demonstration for the adaptability of the axial expansion method.

The models tested for this purpose were intentionally simple to minimize confounding factors. For this test 6 different models were made, three of which used 1 group cross sections, and three of which used seven group cross sections from C5G7. All of these demonstrations used a single fissionable material, a single pin cell, and two 1 cm thick axial slices.

The first system, 1GIH, was a one group system which was infinite and homogeneous in all directions, and therefore had no spatial variation axial or otherwise. The second system, 1GHS, was a one group system with vacuum boundary conditions at the top and reflective boundary conditions everywhere else, and therefore had solely axial variation centered about the bottom of the model. The third system, 1GS, was a one group system with vacuum boundary conditions at the top and bottom, and reflective boundary conditions everywhere else, and therefore had solely axial variation centered about the middle of the model. The last three systems (7GIH, 7GHS, and 7GS) were the exact same as the first three systems except with 7 group cross sections from C5G7. All models were given a maximum of 100,000 iterations to converge. The convergence results demonstrating the stability of the method are shown for runs without CMFD in Table 5.2 and with CMFD in Table 5.3. By necessity, traditional 2D/1D must be run with CMFD in MPACT.

The convergence in Table 5.2 and 5.3 results show an interesting trend. The fact that the convergence greatly slowed down with the addition of CMFD in the axial expansion systems that had axial variability, indicates that some of the instability in these systems are present in

CMFD itself. However, the observation that traditional 2D/1D with with CMFD enabled still did not converge, indicates that the traditional 2D/1D method introduced additional instability not found in the axial expansion method. Whether that instability alone would be sufficient to prevent convergence with CMFD disabled is difficult to determine due to limitations preventing MPACT from running traditional 2D/1D without CMFD. Regardless, these results demonstrate that the axial expansion method is convergent both with and without CMFD in thin slice systems where traditional 2D/1D is not.

Case	$N = 0$ **no CMFD**	$N = 1$ **no CMFD**	$N = 2$ **no CMFD**
1GIH	23	25	31
1GHS	90	131	139
1GS	48	38	37
7GIH	6562	6558	6558
7GHS	32	34	34
7GS	18	16	16

Table 5.2: Convergence Iterations for Thin Slice Problems.

Case	$N = 0$ **CMFD**	$N = 1$ **CMFD**	$N = 2$ **CMFD**	**Traditional 2D/1D**
1GIH	2	2	2	2
1GHS	146	313	341	Did not converge
1GS	65	77	169	Did not converge
7GIH	7	8	8	7
7GHS	69	310	Did not converge	Did not converge
7GS	41	75	125	Did not converge

Table 5.3: Convergence Iterations for Thin Slice Problems.

Additionally, in this discussion of instability for thin slices, the 1D/1D case with an inserted thin slice in Section 5.1.1 was rerun in MPACT with axial expansion and exhibited the same behavior. Failure to converge in traditional 2D/1D and convergence with the axial expansion method. CMFD in this case did improve convergence, reducing the number of iterations to converge from $O(1000)$ to $O(100)$. Furthermore, the RAARI case described in Section 5.1.1 was run in MPACT where all 3.57 cm slices were replaced with four 1 cm slices. This case also failed to converge in traditional 2D/1D but converged both with and without CMFD using axial expansion with a similar speedup to the thin slice insertion case.

These results indicate that some of the instability in thin slice problems can come from CMFD, however not all of it does. And even with CMFD, the axial expansion method seems capable of

converging in these systems, while traditional 2D/1D does not always converge in these types of systems. Indeed, even in systems where CMFD speeds up the convergence, and is therefore presumed to be relatively stable, traditional 2D/1D is still not necessarily convergent.

5.1.3 Void Stability Demonstration

In order to demonstrate the axial expansion method's capabilities in systems with void-like regions surrounding fuel, a 1D/1D pin-cell like model was created. The axial properties of the model mirrored the cold KRITZ-2:1 case described in Section 5.3.1, while the radial portion of the model involved infinite slabs of fuel surrounded by either moderator or air depending on the axial position. 51 group MPACT cross sections were used for this problem. The geometry for this model is shown in Figure 5.5.

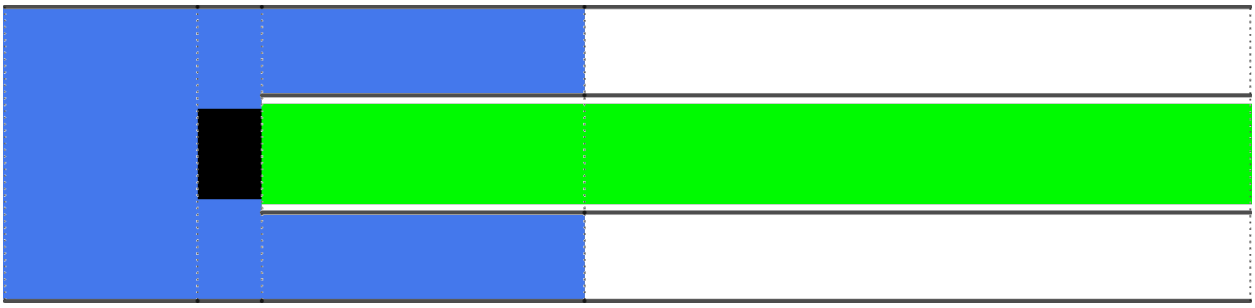

Figure 5.5: 1D/1D Void Demonstration Model (Not to Scale, Rotated)

Convergence results for the model are shown in Table 5.4. The results show that the axial expansion method universally converges for this voided problem, while traditional 2D/1D failed to converge. Furthermore, CMFD is shown to be effective in accelerating the convergence of the axial expansion method even in void-like systems. The stability of CMFD in the axial expansion calculation would seem to indicate that the instability of traditional 2D/1D is either exclusive to 2D/1D for this void problem, or is a result of the interaction between traditional 2D/1D and CMFD. Either way, the voided problem demonstrates the improved robustness of the axial expansion compared to traditional 2D/1D in problems with neutronically important void-like regions surrounding fuel.

CMFD?	**AxExp** $N = 0$	**AxExp** $N = 1$	**AxExp** $N = 2$	**Traditional 2D/1D**
CMFD	21	90	90	Did not converge
No CMFD	216	407	402	Not Available

Table 5.4: 1D/1D Void Convergence

5.2 2D/1D Demonstrations

With the method fully implemented in MPACT, 2D/1D runs using the method could be made. Initial runs featured pure source iterations to converge the system, but eventually CMFD was implemented and used for later runs. Initial runs were used to demonstrate correctness in comparison with traditional 2D/1D, and during the development of CMFD balance tests were made and used. Eventually, demonstration of capabilities in problems with void-like regions was performed with and without CMFD acceleration.

5.2.1 Pin Cell Demonstration

For confirmation that the method was implemented correctly in MPACT, three models of gradually increasing complexity were tested. This testing involved first running a reference calculation using MPACT's traditional 2D/1D method on a very fine axial grid. Next both the traditional 2D/1D and the axial expansion method are both run on identical meshes and compared. If the error from the axial expansion is similar or less than the error from the traditional 2D/1D, then it is determined to have succeeded the comparison test and confidence in the implementations correctness is increased.

The first model was that of a one group homogeneous 1 cm cube with reflective BCs (boundary conditions) on all sides except the top which has vacuum BCs. The one group cross sections were simple and formulated such that the eigenvalue for an infinite homogeneous system was 1.425. Since the system is equivalently a 1D slab system, the reference calculation was done exclusively using the radial solver by making the model a single slice and moving the vacuum BC to the right side. Then 20 equal sized 0.05 cm slices in the x direction were used for the radial solver. For the comparison calculations, the slice size was 0.5 cm with no radial divisions since the system is radially invariant. This model was run to test simple single region leakage.

The second model was of an extruded fuel pin cell model based off of the C5G7 [68] UO2-3.0 pin cells. The cross sections were similarly sourced from the C5G7 benchmark, and as such were 7 group cross sections. The pin cell was given reflective BCs on all sides except the top which had vacuum BCs and had a axial length of 15 cm. The reference mesh had 100 axial slices of 0.15 cm thickness each. The comparison calculations had 3 slices of 5 cm thickness each. This model was run to test more complex multi-region/multi-group leakage. An illustration of the radial divisions within the pin cell is shown in Figure 5.6.

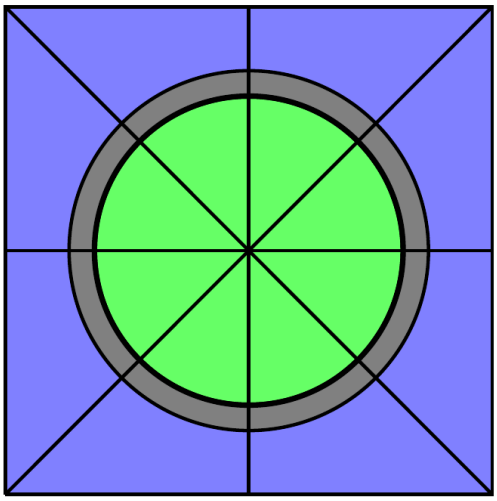

Figure 5.6: Pin Cell Divisions

The third model identical to the pin cell from the second model but with the addition of an non-extruded 1 cm buffer of pure moderator at the top before the vacuum BCs. The system was given reflective BCs on all sides except the top which had vacuum BCs. The reference mesh had 100 axial slices of 0.15 cm thickness each in the fuel, and 10 slices of 0.1 cm thickness each in the moderator. The comparison calculations had 3 slices of 5 cm thickness each in the fuel, and a single slice of 1 cm thickness in the moderator. This model was run to test leakage for situations without purely extruded meshes and where not all slices are of equal thickness. An illustration of the disjoint nature of the mesh is shown in Figure 5.7.

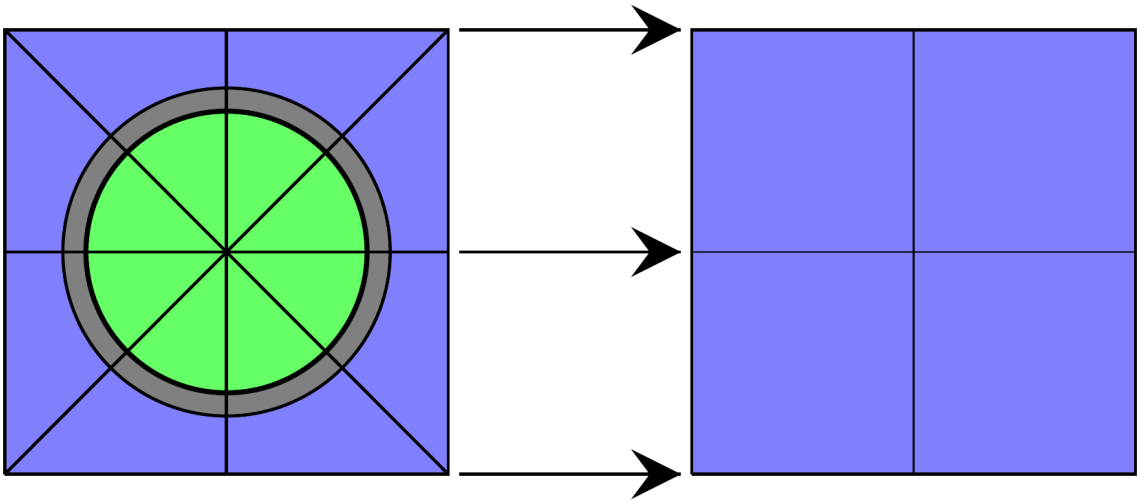

Figure 5.7: Disjoint Mesh

For analysis of the implementation, we are investigating comparison of the globally calculated eigenvalue. The eigenvalue results from this computations for all 3 models are shown in Table 5.5.

Method/Case	One Group Block	Pin Cell No Buffer	Pin Cell With Buffer
Reference	1.350394	0.987853	1.015915
Traditional 2D/1D	302	694	467
Axial Expansion	-2	122	252

Table 5.5: Eigenvalue results and errors in pcm.

So it can be observed that the one group homogeneous system is quite far from criticality, while the pin cell with no buffer and the pin cell with moderator buffer are both near criticality, being just subcritical and just supercritical respectively.

The associated eigenvalue errors compared to the reference calculation are shown in Table 5.5. These results show that the axial expansion method consistently performs about as well or better than traditional 2D/1D.

The axial expansion calculations are all performed for the case in which the Legendre polynomial expansion uses $N = 3$. So, the matrices used for the transport system are 4×4, and the vectors similarly have a length of four. All models used a Chebyshev-Yamamoto product quadrature for angular discretization with 16 azimuthal angles per quadrant and 2 polar angles per half sphere with 0.05 cm ray spacing.

5.2.2 Small Array Demonstration

A small pin cell array model was tested as an intermediate system before testing a larger assembly level system. The model used pins from the C5G7 [68] benchmark. The pin cell grid is shown in Figure 5.8

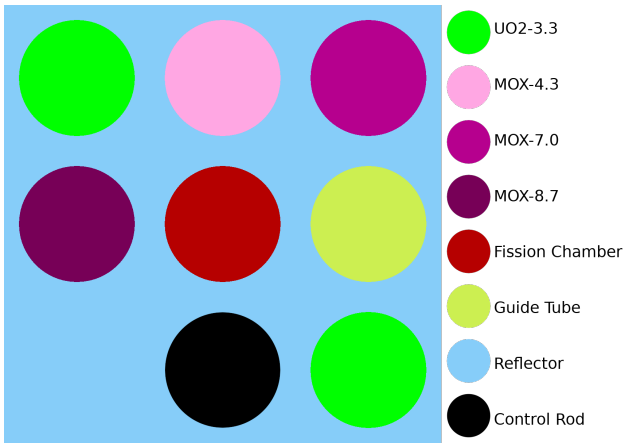

Figure 5.8: Small Pin Cell Array

All fuel pins were 42.84 cm tall with a buffer of 21.42 cm of water above them. All fuel pins

were 1.08 cm in diameter with a fuel pitch of 1.26 cm. The fuel rod extended from the top of the model to one of three locations for three different tests. The first test extended it to 10.71 cm above the bottom in order to make the model as close to critical as possible with this configuration and these slice sizes. The second test extended it all the way into the bottom of the system. The third test fully withdrew it to the top of the fuel, but not out of the water. The model had reflective boundary conditions on all sides except the top.

The mesh axial slices were all 3.57 cm tall, except for the reference test case which used an axial slice size of 0.357 cm. The mesh had pin cells composed of 8 radial divisions in total, 5 of fuel and 3 of moderator. The fuel pins also used 8 azimuthal divisions for a total of 64 regions in each fuel pin. The moderator pins had 5 equal divisions in the x direction and 5 in the y for 25 regions in each moderator pin. The model was run with 16 azimuthal angles and 2 polar angles per octant. This equates to 32 total angles per octant of the unit sphere. The model was run with 0.05 cm ray spacing. 7 group C5G7 cross sections were used.

The eigenvalue results from this computations for all 3 test cases are shown in Table 5.6.

Method/Case	**Fully Inserted**	**Fully Withdrawn**	**Partially Inserted**
Reference	0.830497	1.186888	1.0320475
Traditional 2D/1D	-0.14	4.82	52.36
Axial Expansion	-405.58	-22.21	-42.51

Table 5.6: Eigenvalue results and errors in PCM.

So it can be observed that all cases behaved roughly along expectations with the fully withdrawn control rods being very supercritical, the fully inserted being subcritical, and the fine tuned insertion being nearly critical.

The associated eigenvalue errors compared to the reference calculation are shown in Table 5.6. These results show that the axial expansion method consistently performs about as well as traditional 2D/1D, except in the situation of the fully inserted calculation. What is most surprising about this calculation is that the traditional method did so well when this eigenvalue was so far from criticality. Previous experience has shown that the coarser meshes tend to do worse when further from criticality. As of yet, no explanation has been discovered for why the axial expansion calculation performed so poorly on this calculation or why coarse meshed traditional 2D/1D performed so well. It is likely this was the result of some form of cancellation of error.

The axial expansion calculations are all performed for the case in which the Legendre polynomial expansion uses $N = 2$. So, the matrices used for the transport system are 3×3, and the vectors similarly have a length of three. All models used a Chebyshev-Yamamoto product quadrature for angular discretization with 16 azimuthal angles per quadrant and 2 polar angles per half sphere with

0.05 cm ray spacing.

5.2.3 B&W 1484 Demonstration

The B&W 1484 Core 1 [74] critical experiment shown in Figure 5.9 is a popular benchmarking problem for neutron transport codes [75]. Core 1 is not an exact model of the critical experiment since an extra column of pin cells was added in the center of the core so that the core was fully quarter core symmetric.

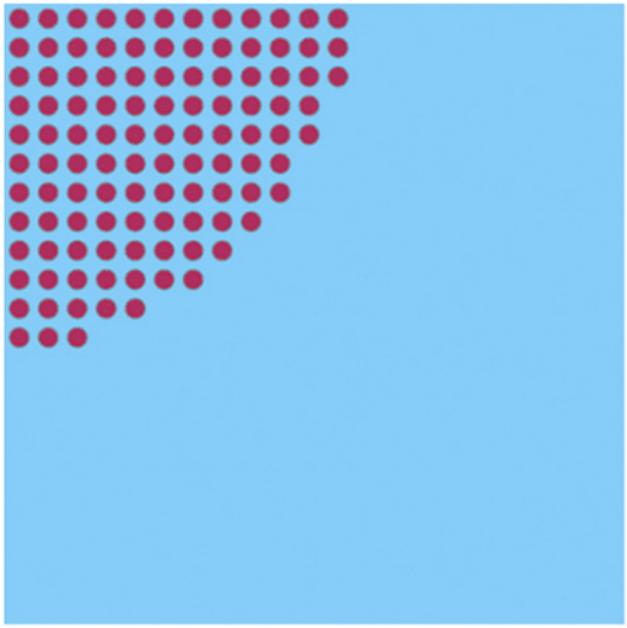

Figure 5.9: B&W 1484 Core 1 [74]

The model was run with 16 azimuthal angles and 2 polar angles per octant. This equates to 32 total angles per octant of the unit sphere. The model was run with 0.05 cm ray spacing. 51 group MPACT cross sections were used.

The mesh had pin cells composed of 4 radial divisions in total, 1 of fuel, 1 of gap, 1 of clad, and 1 of moderator. The fuel pins also used 8 azimuthal divisions for a total of 32 regions in each fuel pin. The moderator pins had 2 equal divisions in the x direction and 2 in the y for 4 regions in each moderator pin. These pin cell divisions are then identical to those shown in Figure 5.7. This results in a total of 5,384 source regions in the model.

Due to the large nature of the assembly sized B&W model and current issues involving present inefficiencies in the axial expansion implementation in both speed and memory usage, the B&W model was only run for the standard mesh and conditions. The axial expansion calculation resulted in a computed eigenvalue of 0.9987379 and the MPACT 2D/1D resulted in a computed eigenvalue

of 1.0029452 representing a disparity of about 400 pcm. Which is roughly consistent with the disparities we have observed in other tests.

As a critical experiment, the expectation is that the result with be critical with an eigenvalue of 1. In this regard, the axial expansion method was 126 pcm off of criticality while traditional 2D/1D was 295 pcm off criticality. This indicates an improvement in accuracy using the axial expansion method over 2D/1D for the same mesh.

5.2.4 Void Stability Demonstration

Building upon the 1D/1D work in Section 5.1.3, a 3D pin cell model were created from the KRITZ-2:1 model at 19.7°C described in Section 5.3.1. The pin cell model was an exact copy of the pin cell found in the full KRITZ-2:1 model and as such, the axial shape matches that represented in Figure 5.5. 51 group MPACT cross sections were used for this problem. The model had varying slice sizes, all on the order of 10 cm. The FSR divisions and radial geometry for this model is shown in Figure 5.10.

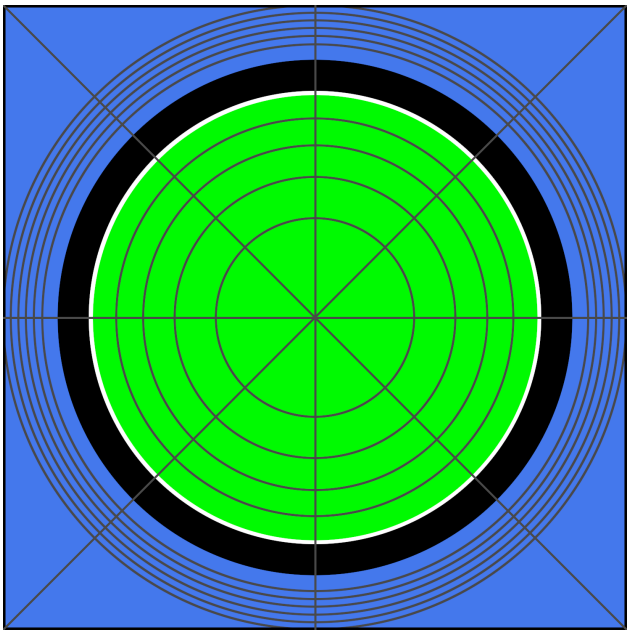

Figure 5.10: 2D/1D Void Model Radial FSR Division. To Scale

Convergence results for the model are shown in Table 5.7. The results show that the axial expansion universally converges for this voided problem, while traditional 2D/1D failed to converge. In fact, these results almost exactly mirror the results shown in Table 5.4, indicating that the conclusions drawn from the 1D/1D investigations into uncovered fuel hold true in full 3D neutron transport.

CMFD?	AxExp $N = 0$	AxExp $N = 1$	AxExp $N = 2$	Traditional 2D/1D
CMFD	20	50	91	Did not converge
No CMFD	219	409	404	Not Available

Table 5.7: 1D/1D Void Convergence

We once again observe that the axial expansion method is stable for this problem for $N = 0$ to $N = 2$ expansions while traditional 2D/1D is not. Additionally, CMFD is effective at accelerating the axial expansion calculation, indicating that the instability does not solely lie in CMFD for this problem.

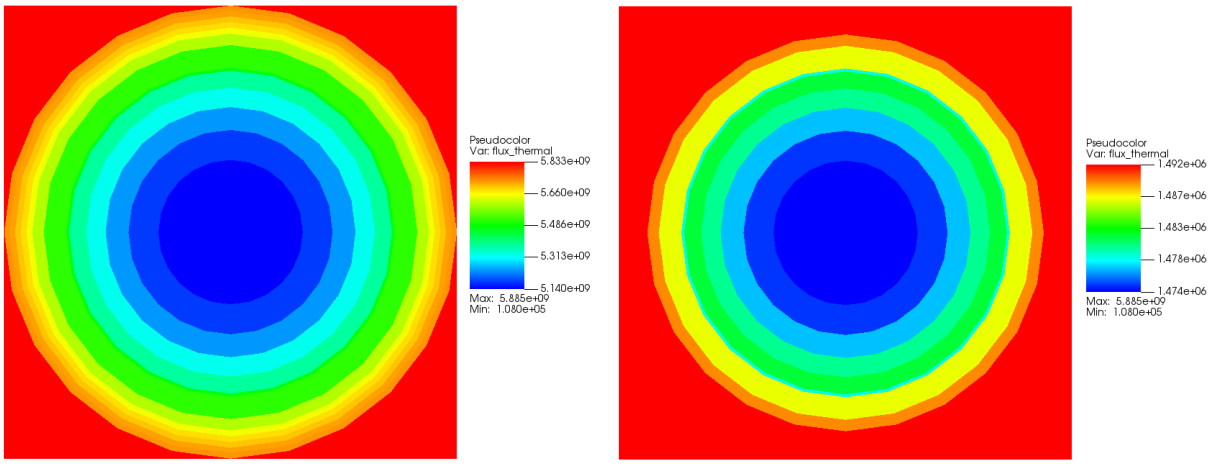

Submerged Fuel Thermal Flux Bare Fuel Thermal Flux

Figure 5.11: Void Test Thermal Flux.

Figure 5.11 shows radial slices of the thermal flux distribution in both submerged and bare portions of the fuel pin. It can be observed that the radial distribution is very similar for the thermal flux both above and below the water line. As expected, thermal flux is very low inside the fuel where thermal neutrons would be expected to quickly be removed either through absorption or fission. Also unsurprisingly, the thermal flux is greater in magnitude below the water line, where the moderator is dense enough to produce a lot of thermal flux. It can also be observed that in the bare fuel portion, the relative magnitude difference between the thermal flux in the fuel and the thermal flux outside the fuel is much smaller compared to the submerged fuel. This is likely due to the fact that the void surrounding the bare fuel is very low in density and therefore does very little to moderate neutrons, resulting in the majority of thermal flux likely coming from axial leakage.

Figure 5.12 shows radial slices of the fast flux distribution in both submerged and bare portions of the fuel pin. This distribution shows an interesting reversal in trends. Fast flux is higher inside the fuel where fission is expected to occur in the submerged region, however it is very spatially

invariant, and in fact slightly higher outside the fuel in the bare region. This reversal seems to indicate two things. First, as expected there is little moderation in the void region, resulting in little loss of fast neutrons outside the fuel. Second, the fact that the fast flux is actually slightly higher in the void would not be expected even without much moderation in the void unless another source of fast flux was dominant over the fission production. This other dominant source of fast flux could only be the axial leakage, which must be translated using the 1D portion of the method. As such, it can be observed that void-like regions above moderated regions can lead to situations where the dominant source of flux in some groups is the axial leakage of that flux, not the production within the coarse cell. As explained in Section 1.2.1, this can potentially lead to instability of traditional 2D/1D and lead it to fail, which is exactly what is observed in this test.

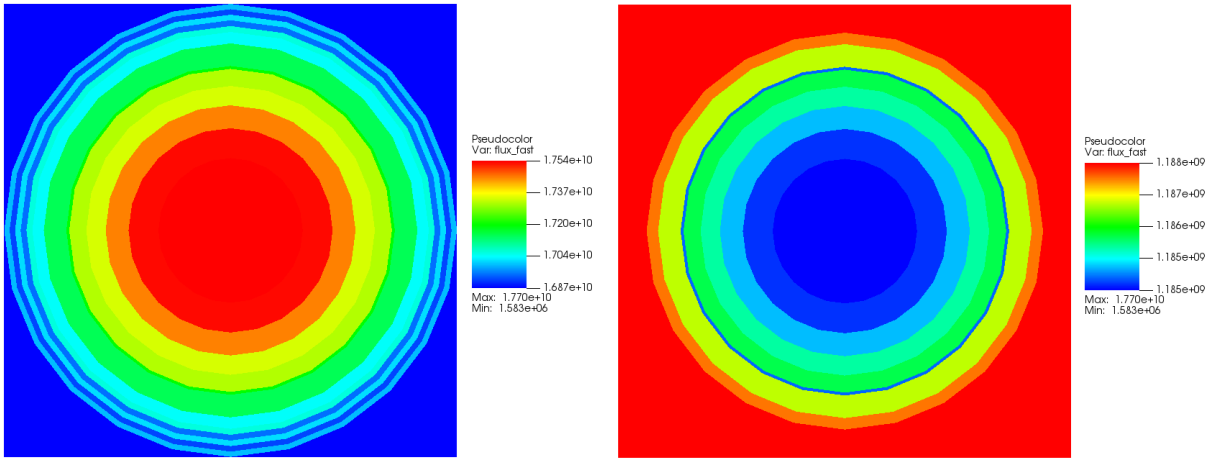

Submerged Fuel Fast Flux Bare Fuel Fast Flux

Figure 5.12: Void Test Fast Flux.

Void Models Axial Expansion Convergence

The convergence of the axial expansion order was investigated for the fuel pin models with void-like regions described in Sections 5.1.3 and 5.2.4. Figure 5.13 shows the convergence of the the k_{eff} eigenvalue for both the 2D and 3D void stability models. It can be seen in this figure that the eigenvalues of both models converge to around 1.14.

In Figure 5.14, the pcm difference between each axial expansion order and the $N = 10$ run is plotted. For both the 2D and 3D void stability problems, quick convergence is achieved, with $N = 1$ differing by about 45 pcm in both models, and $N = 4$ being sufficient to achieve less than 1 pcm difference from the $N = 10$ model for both the 2D and 3D fuel pin models. This is quite consistent with the change in errors observed in Figure 5.2, so this result indicates that the method is well behaved in terms of axial expansion convergence even for problems with void-like regions surrounding fuel.

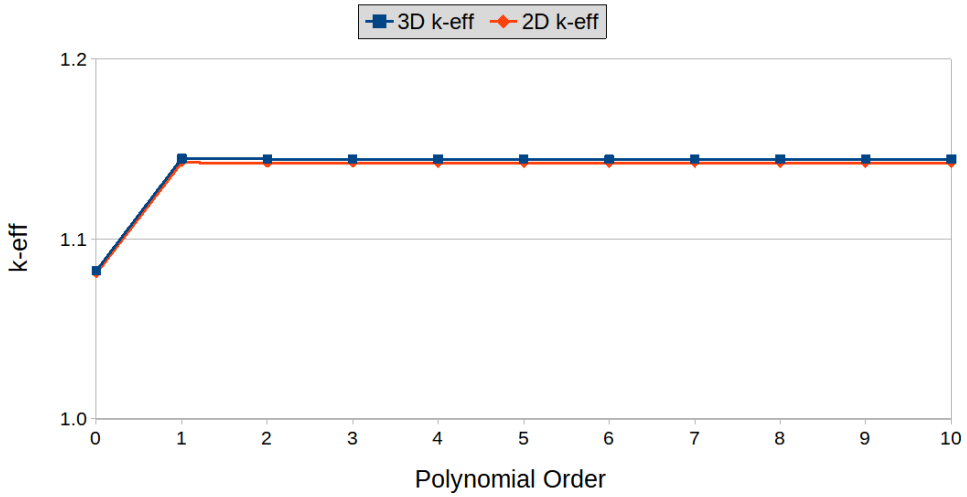

Figure 5.13: Void Stability Models k_{eff} Convergence

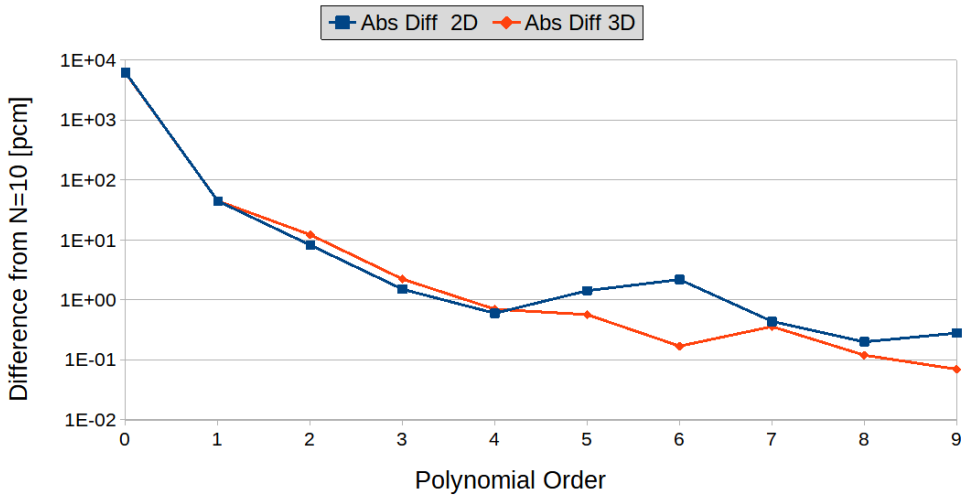

Figure 5.14: Void Stability Models Absolute k_{eff} Difference from $N = 10$

5.3 KRITZ-2:1 Experiments

From 1972 to 1973, various experiments using the KRITZ-2 system were performed at Studsvik, Sweden. These experiments were designed to create critical configurations of rectangular (often square) arrangements of uranium or MOX Zircaloy-2 clad fuel rods in light water. This criticality was achieved by adjusting the water level in the core and the boron concentration in the moderator. These experiments were performed to achieve criticality at both room temperature (called cold) conditions, around 20°C, as well as hot conditions, around 250°C.

As critical configurations, the k_{eff} eigenvalue for these systems is necessarily known to be 1. Additionally, axial critical buckling was determined as were relative rod powers for fission rate distributions in selected fuel rods.

Several experiments were performed in KRITZ including the subject of this section, KRITZ-2:1. The top view of the layout is shown in Figure 5.15. KRITZ-2:1 was a square 44×44 array of LEU fuel pins surrounded by water. The square lattice pitch was 18-mm and the UO_2 fuel in the fuel rods had a density of 10.415 g/cm^3 with a U^{235} enrichment of 1.86 wt% and negligible plutonium oxide. The cold experiment for KRITZ-2:1 was performed at 19.7°C while the hot experiment was performed at 248.5°C. Since the experimental design had a negative thermal reactivity coefficient (which is to say that increases in temperature will decrease the eigenvalue [76]), the moderator height is increased for the hot run and the boron concentration is further diluted. For both these critical configurations, a non-negligible amount of fuel was exposed above the water line surrounded by a void-like material of saturated steam.

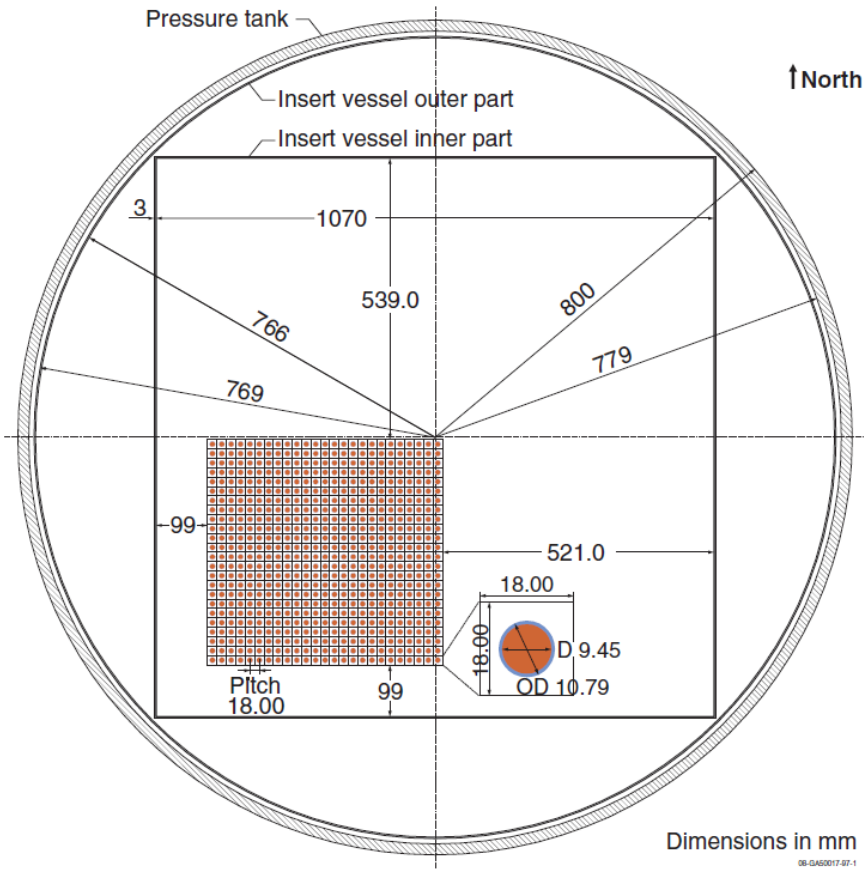

Figure 5.15: Top View of KRITZ-2:1 Experiment [9]

However, this region of the fuel is still neutronically important to the solution of the transport equation. As such, modeling of this region is important in order to obtain accurate simulation results

for the KRITZ-2:1 experiments. Unfortunately, traditional 2D/1D can be unstable for systems with neutronically important void-like regions adjacent to fuel regions. This is the case with KRTIZ-2:1 and, as such the 3D simulation of these critical configurations has previously been limited in MPACT to either simulation of the covered fuel, which underestimates the eigenvalue due to missing a large portion of the active fuel, or simulation of the system with artificially increased steam density in order to maintain stability in the bare fuel region which overestimates the eigenvalue due to additional moderation. Additionally, 2D axial buckling cases can be performed for the KRITZ-2:1 experiment, but the data is not considered acceptable as a buckling benchmark experiment.

5.3.1 KRITZ-2:1 Cold (19.7°C)

For the cold KRITZ-2:1 experiment, the reactor was operated at a temperature of 19.7°C. At this temperature criticality was achieved at a moderator height of 652.8 mm and a moderator boron concentration of 217.9 ppm. Since the active fuel was 2000 mm in total height, this left 1347.2 mm of fuel bare and uncovered, surrounded by saturated vapor which neutronically is considered a void-like material. The radial distribution of the flux is shown in Figure 5.16 and Figure 5.17.

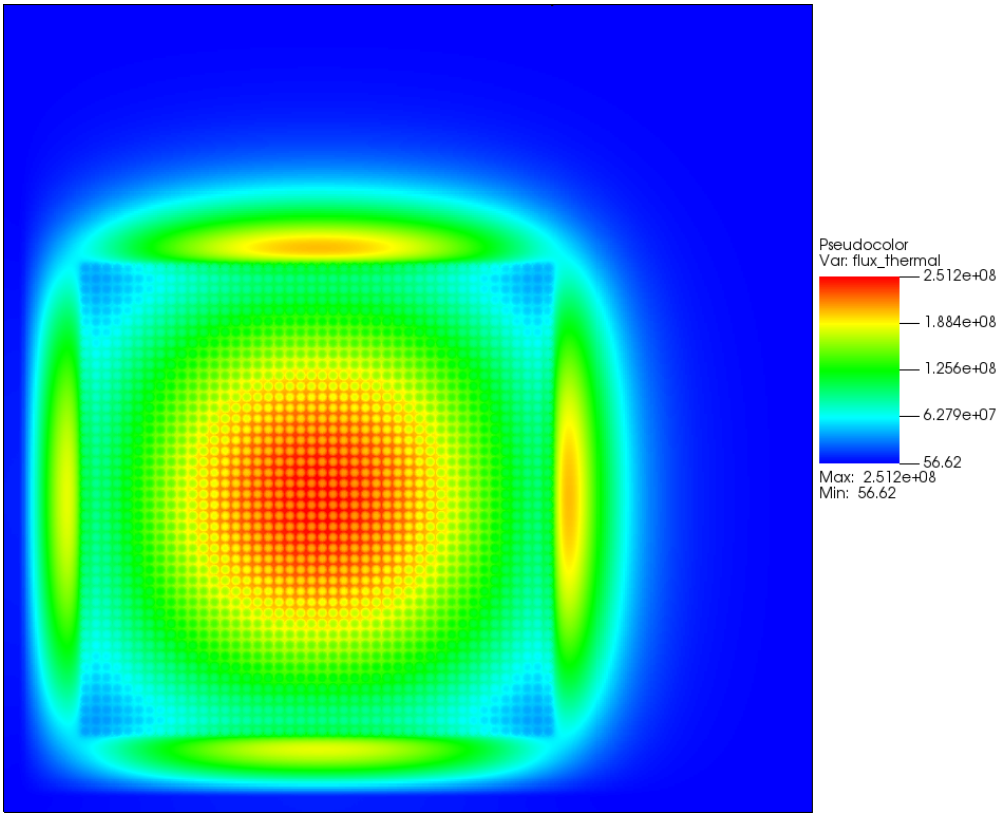

Figure 5.16: KRITZ-2:1 19.7°C Thermal Flux

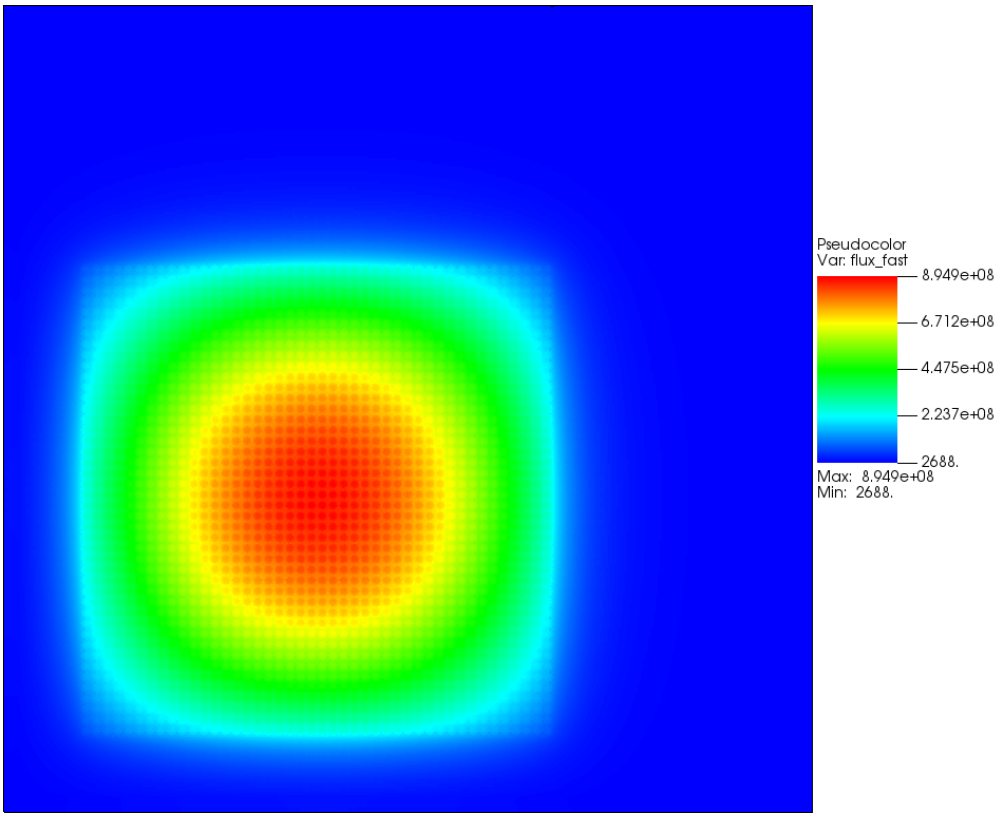

Figure 5.17: KRITZ-2:1 19.7°C Fast Flux

This model was run for 2D axially buckled cases for three different levels of anisotropic scattering. Eigenvalues are shown in Table 5.8.

Scattering	TCP0	P1	P2	P3
Eigenvalue	1.0252118	0.9903782	0.9910047	0.9908927

Table 5.8: 2D Axial Buckling Eigenvalue Results

These results demonstrate a significant dependence of the system eigenvalue on anisotropic scattering. Indeed, TCP0, which is often expected to be very similar to P1 scattering in LWR systems, is 3483 pcm different from P1 scattering and 3431 pcm different from the P3 scattering. These results also demonstrate that the axial buckling data for KRITZ-2:1 is not sufficient to create accurate 2D simulations since even the P3 scattering results are 911 pcm off of criticality.

Traditional 2D/1D cases were run for a cutoff, covered, and voided model. The cutoff model involves only modeling the axial portion of the fuel which is below the water line in the original experiment. The covered model involves modeling the entire system, but artificially increases the steam density to match the density of moderator and avoid void-like regions. Finally, the voided

model is the entire experiment, modeling the bare fuel true to experimental specifications with saturated steam surrounding it instead of water.

Case/Scattering	TCP0	P1	P2	P3
Cutoff	Did not converge	Did not converge	Did not converge	Did not converge
Covered	1.0881198	1.0525992	1.053239	1.0531229
Voided	Did not converge	Did not converge	Did not converge	Did not converge

Table 5.9: Traditional 2D/1D Eigenvalue Results

Results for traditional 2D/1D cases in Table 5.9 for these models demonstrate three things. First, as expected the fully covered model greatly over-predicts the eigenvalue with the P3 case being 5312 pcm over criticality. Second, we again observe that for this problem, TCP0 scattering over-predicts the eigenvalue compared to P3, being 3500 pcm over the P3 result which is pretty consistent with the 3431 pcm over-prediction observed from the 2D axial buckling results. Third, these models do appear to be relatively unstable using traditional 2D/1D with not only the voided model failing to converge, which was expected, but also the axial variance is large enough in the shorter cutoff model that the calculation for that model still failed to converge.

For the axial expansion model of this experiment, the full active fuel length was modeled. This includes both the 65.28 cm of submerged fuel, as well as the 134.72 cm of uncovered bare fuel above it. The axial expansion cases were limited to TCP0 scattering since anisotropic scattering has not yet been implemented for the axial expansion method in MPACT. All cases were run with CMFD enabled, this is especially important in a large system like this where the flat error modes may take a very long time to converge. Due to implementation limitations in both time and memory efficiency, the axial expansion calculations were limited to $N = 0$ and $N = 1$. From the results in Figures 5.2, 5.13, and 5.14, the difference between $N = 1$ and higher order axial expansion is expected to be well under 100 pcm. Eigenvalues are shown in Table 5.10.

Solver	AxExp $N = 0$	AxExp $N = 1$	Traditional 2D/1D
Eigenvalue	0.9684086	1.0389560	Did not converge

Table 5.10: 3D Eigenvalue Results

In these results, it can be observed that the $N = 0$ axial expansion shows an expected large difference relative to the $N = 1$ calculation of 7055 pcm, which is quite close to the 3D model difference of 6203 pcm shown in Figure 5.14 from the void stability demonstration. One thing of note is that while the $N = 1$ result is 3896 pcm above the ideal result of criticality, this is actually quite close to the difference observed in the 2D results of TCP0 being 3431 pcm above the P3

scattering results from Table 5.8 and the traditional 2D/1D difference of TCP0 being 3500 pcm over P3 scattering from Table 5.9. While this trend should not be expected to exactly hold when moving from 2D axially buckled or traditional 2D/1D to axial expansion 3D neutron transport, it may be an indicator that near critical results could be achieved using the axial expansion method with higher order scattering for this simulation.

5.3.2 KRITZ-2:1 Hot (248.5°C)

For the hot KRITZ-2:1 experiment, the reactor was operated at a temperature of 248.5°C. At this temperature criticality was achieved at a moderator height of 1055.2 mm and a moderator boron concentration of 26.2 ppm. Since the active fuel was 2000 mm in total height, this left 944.8 mm of fuel bare and uncovered, surrounded by saturated vapor which neutronically is considered a void-like material. The radial distribution of the flux is shown in Figure 5.18 and Figure 5.19.

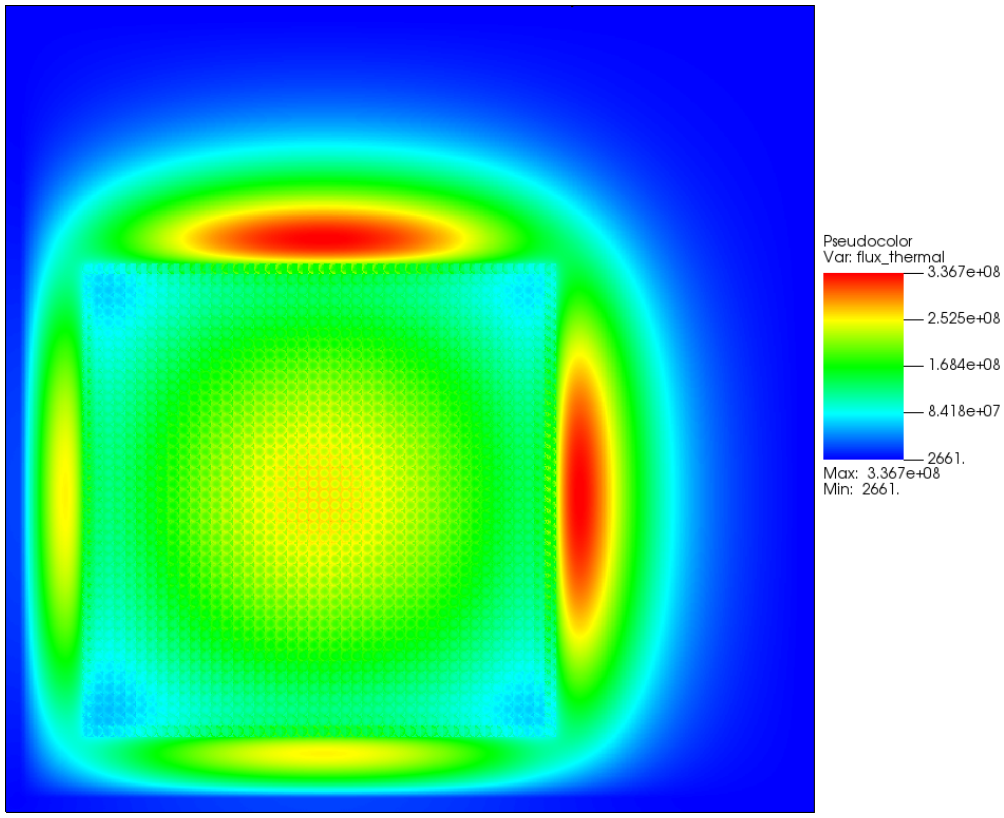

Figure 5.18: KRITZ-2:1 248.5°C Thermal Flux

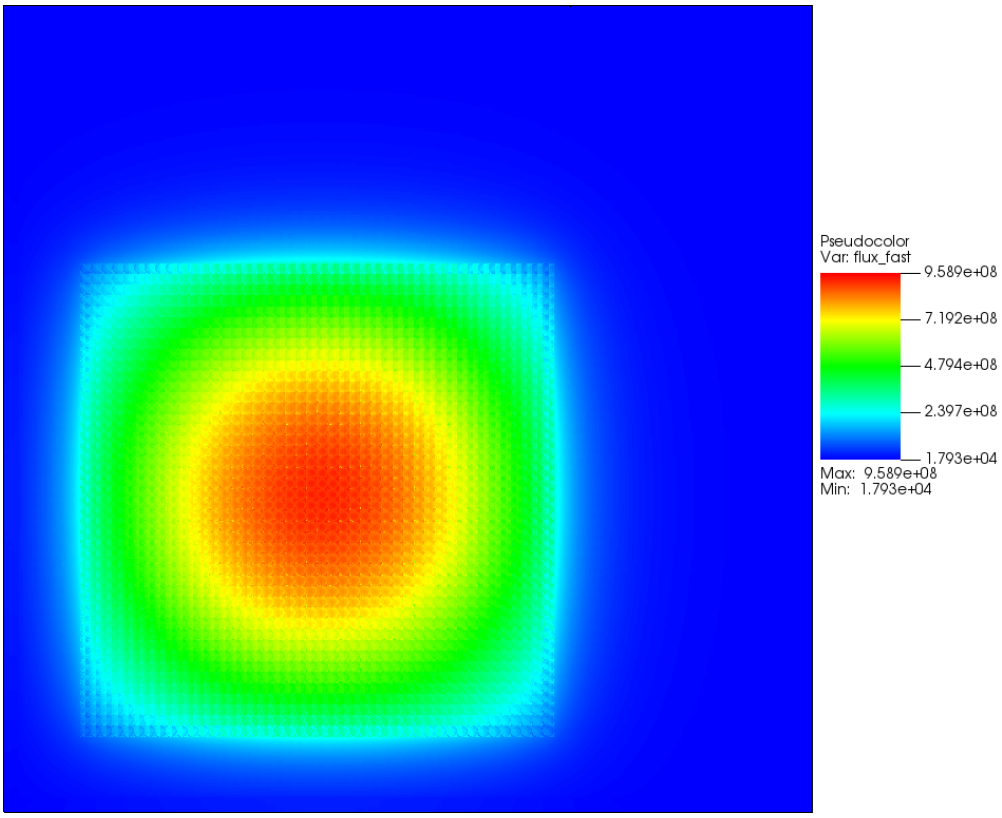

Figure 5.19: KRITZ-2:1 248.5°C Fast Flux

This model was run for 2D axially buckled cases for three different levels of anisotropic scattering. Eigenvalues are shown in Table 5.11.

Scattering	TCP0	P1	P2	P3
Eigenvalue	1.0331942	0.9918227	0.9926015	0.9924803

Table 5.11: 2D Axial Buckling Eigenvalue Results

These results demonstrate a significant dependence of the system eigenvalue on anisotropic scattering. Indeed, TCP0, which is often expected to be very similar to P1 scattering in LWR systems, is 4137 pcm different from P1 scattering and 4071 pcm different from the P3 scattering. These results also demonstrate that the axial buckling data for KRITZ-2:1 is not sufficient to create accurate 2D simulations since even the P3 scattering results are 752 pcm off of criticality.

Traditional 2D/1D cases were run for a cutoff, covered, and voided model. The cutoff model involves only modeling the axial portion of the fuel which is below the water line in the original experiment. The covered model involves modeling the entire system, but artificially increases the steam density to match the density of moderator and avoid void-like regions. Finally, the voided

model is the entire experiment, modeling the bare fuel true to experimental specifications with saturated steam surrounding it instead of water.

Case/Scattering	TCP0	P1	P2	P3
Cutoff	1.0238304	0.9902754	0.9908828	0.9907986
Covered	1.0406973	1.0068462	1.0074712	1.007359
Voided	Did not converge	Did not converge	Did not converge	Did not converge

Table 5.12: Traditional 2D/1D Eigenvalue Results

Results for traditional 2D/1D cases in Table 5.12 for these models demonstrate four things. First, the fully covered model over-predicts the eigenvalue with the P3 case being 736 pcm over criticality, much closer than the results in Table 5.9. This is likely explained by the fact that the bare region is as smaller percentage of the active fuel length in the hot case than the cold case so increase in moderation in that region will have less of an impact on the eigenvalue. Second, the cutoff model is stable enough to converge in traditional 2D/1D and the eigenvalue is under-predicted as expected. The under-prediction is 920 pcm, which indicates that the neutronic value of the bare fuel is still significant. Third, we again observe that for this problem, TCP0 scattering over-predicts the eigenvalue compared to P3, being 3303 pcm over the P3 result for the cutoff case and 3334 pcm over the P3 case for the covered case, which is pretty close to the 4071 pcm over-prediction observed from the 2D axial buckling results.

For the axial expansion model of this experiment, the full active fuel length was modeled. This includes both the 105.5 cm of submerged fuel, as well as the 94.48 cm of uncovered bare fuel above it. The axial expansion cases were limited to TCP0 scattering since anisotropic scattering has not yet been implemented for the axial expansion method in MPACT. All cases were run with CMFD enabled, this is especially important in a large system like this where the flat error modes may take a very long time to converge. Due to implementation limitations in both time and memory efficiency, the axial expansion calculations were limited to $N = 0$ and $N = 1$. From the results in Figure 5.2, the difference between $N = 1$ and higher order axial expansion is expected to be well under 100 pcm. Eigenvalues are shown in Table 5.13.

Solver	AxExp $N = 0$	AxExp $N = 1$	Traditional 2D/1D
Eigenvalue	0.9765394	1.0363372	Did not converge

Table 5.13: 3D Eigenvalue Results

In these results, it can be observed that the $N = 0$ axial expansion shows an expected large difference relative to the $N = 1$ calculation of 5980 pcm, which is quite close to the 3D model

difference of 6203 pcm shown in Figure 5.14 from the void stability demonstration. One thing of note is that while the $N = 1$ result is 3634 pcm above the ideal result of criticality, this is actually quite close to the difference observed in the 2D results of TCP0 being 4071 pcm above the P3 scattering results from Table 5.11 and the traditional 2D/1D difference of TCP0 being both 3303 pcm and 3334 pcm over P3 scattering from Table 5.12. While this trend should not be expected to exactly hold when moving from 2D axially buckled or traditional 2D/1D to axial expansion 3D neutron transport, it may be an indicator that near critical results could be achieved using the axial expansion method with higher order scattering for this simulation.

5.4 Matrix Exponential Tables Speedup

The speedup capabilities of the matrix exponential calculation tables mentioned in Section 4.4 were tested on the third pin cell model described in Section 5.2.1. The model was tested for a set number of iterations for axial polynomial expansion from N=0 to N=10. Calculation walltime is shown in Figure 5.20.

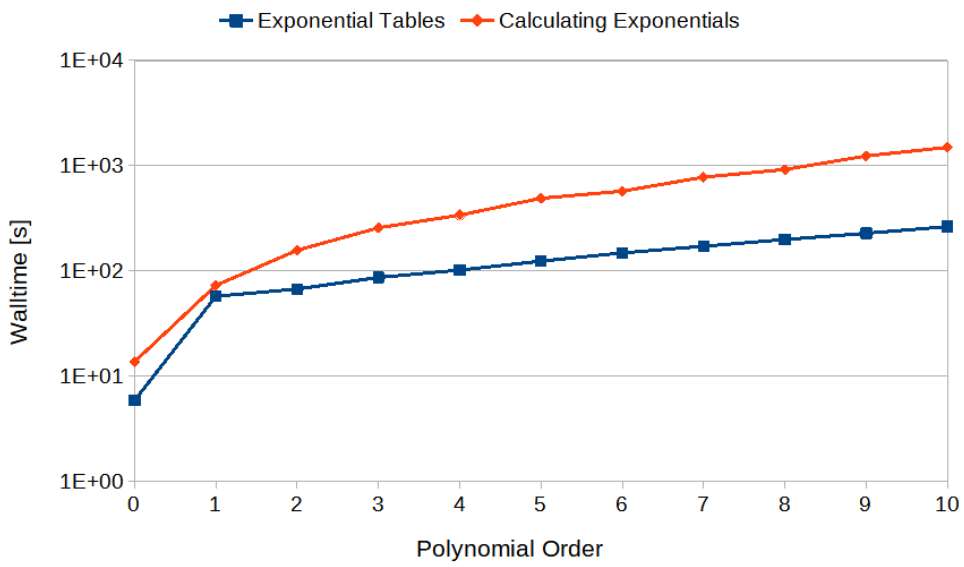

Figure 5.20: Axial Expansion Calculation Times

Relative calculation speedup is shown in Figure 5.21. It can be noticed that the speedup exhibits strange behaviors prior to N=2. This is due to the fact that the implementation of the matrix exponential calculations is analytic for N=0 and N=1. After this, the calculation uses a 6th order Pade approximation, so the comparison then becomes directly between Pade approximations and matrix exponential tables.

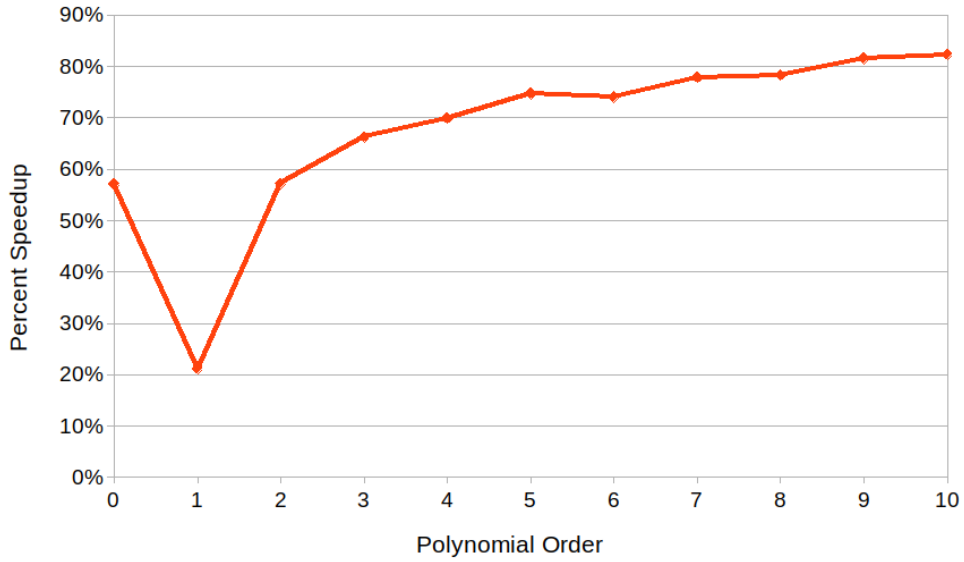

Figure 5.21: Matrix Exponential Tables Speedup

Both methods result in identical calculations, however, the exponential tables are universally faster. Additionally, they scale much better with higher order polynomials with wall-time scaling roughly as $N^{1.4}$ when calculating matrix exponentials and scaling roughly as $N^{0.85}$ when using the matrix exponential tables. This implies that using matrix exponential tables can allow for much higher order axial approximations if they are determined useful or necessary in certain problems, while paying a much smaller price in runtime.

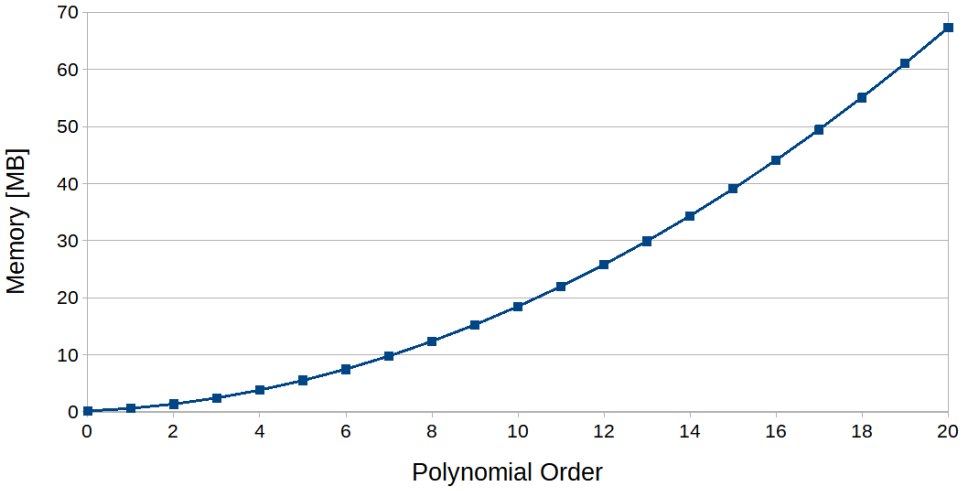

Figure 5.22: Axial Expansion Tables Memory Usage

An analysis of the memory usage by the matrix exponential tales was performed. As explained in Section 4.5, memory usage for the matrix exponential tables is invariant of problem size and

depends solely on order of the Legendre polynomial axial expansion being use. Figure 5.22 shows the memory usage for the axial expansion tables for up to $N = 20$. It can be observed that the memory usage does not exceed 1 MB until $N = 2$ and does not exceed 10 MB until $N = 8$. The memory scaling for the matrix exponential tables is known to be N^2 per Table 4.1

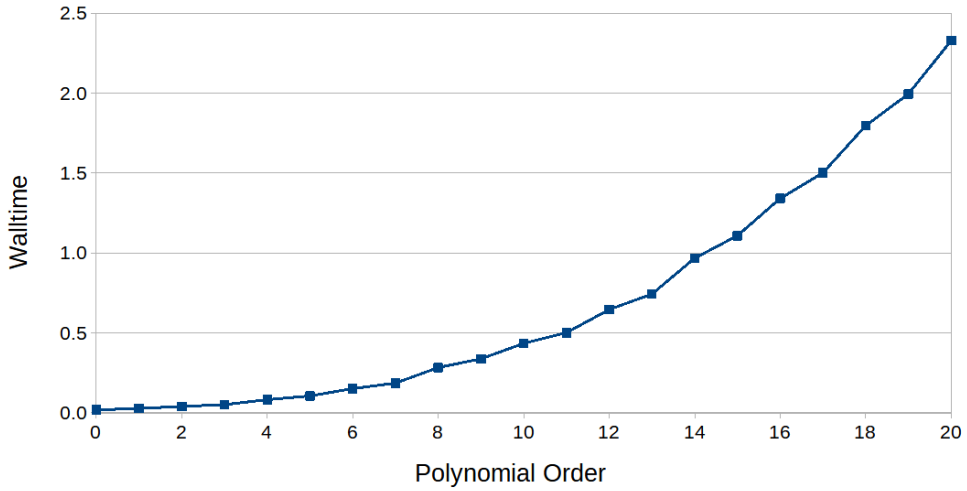

Figure 5.23: Axial Expansion Pre-Computational Time

The pre-computational timing costs of computing the matrix exponential tables were also measured. Figure 5.23 demonstrates the pre-computational time costs for up to $N = 20$. Since these tables are independent of problem size or cross sections, this calculation only needs to be performed once, even for multiphysics problems, and the pre-computational time is invariant with respect to system model. It can be observed that the pre-computational time is quite small even for large values of N. Indeed, the pre-computational time for the matrix exponential tables does not exceed 0.1 seconds until $N = 5$ and is not more than 1 second until $N = 15$. The pre-computational time scaling is measured to be roughly $N^{1.6}$.

5.5 Summary

In this chapter computational experiments using the axial expansion method were performed. The method was initially tested for viability in an exploratory 1D/1D code that revealed that axial mesh extrusion was unnecessary. In 1D/1D explorations using MPACT, stability of the method for contrived problems with thin slices and void-like regions was devised and the method was demonstrated to be more stable than traditional 2D/1D even in cases where CMFD introduced some instability. The 2D/1D implementation in MPACT was then more fully tested from a pin cell up to a large B&W 1484 experiment core.

Additionally, stability of problems with void-like regions in 2D/1D was investigated and the axial expansion method was shown to be stable with CMFD providing effective acceleration, while the traditional 2D/1D failed to converge. This failure was investigated further by analyzing the radial flux distribution both in the submerged and bare portions of the fuel rod. It was observed that the fast flux in the bare fuel portion of the model showed characteristics consistent with axial leakage dominance of the flux, which can cause instability in traditional 2D/1D calculations.

Next, the KRITZ-2:1 experiments were investigated and the stability of the axial expansion method was demonstrated. While the accuracy was not ideal given that the current implementation is limited to isotropic scattering, the error seemed consistent with what could be expected given the difference between isotropic and anisotropic scattering calculations performed using 2D axial buckling calculations and traditional 2D/1D calculations in altered systems without bare fuel.

Finally, the speedup from the matrix exponential tables was demonstrated and the tables were shown to effectively produce a notable speedup in computational time. The cost of this speedup in terms of memory and pre-computational time was analyzed, and the costs of the matrix exponential tables was determined to be quite small.

CHAPTER 6

Conclusions

This chapter provides a brief summary of the work in this thesis. The motivation is reiterated and computational demonstrations are reviewed. Conclusions from these demonstrations are also discussed and possible subjects of future research related to the LPAEM are explored.

6.1 Summary and Conclusions

In this work the problem of instability of the traditional 2D/1D method was explored and difficulties involving use of the method in solving models based on the KRITZ-2 experiments were introduced. While instability in traditional 2D/1D calculations can come from a variety of sources, the primary one believed to be destabilizing these systems is the potential negativity, or even just very small magnitude, of the flux in a coarse cell for some groups. This can lead to destabilizing and non-physical cross section homogenization necessary in the 1D nodal sweep for traditional 2D/1D methods. This potential instability is particularly likely in systems with sharp axial changes to the flux solution and systems with regions of low local sources. Both of these situations are found in systems with bare fuel above submerged fuel since the axial shape of the flux will be rapidly changing at the water-air interface, and the void-like nature of air results in low source production in air regions. This is exactly the physical characteristics present in the KRITZ-2 experiments as they chose to reach criticality by leaving part of the fuel uncovered.

To fill this limitation of traditional 2D/1D methods, an alternative *Legendre Polynomial Axial Expansion Method* (LPAEM) is proposed. The LPAEM explicitly solves the 3D transport equation, albeit with a different spatial discretization method for the axial variable, the same as STREAM and Proteus-MOC but with avoidance of axially extruded FSRs. This is compared to the solving separate equations for the radial plane and the axial direction that is characteristic of traditional 2D/1D methods. Since the method requires no homogenization of cross sections for the axial solution, and since the axial portion of the solution is full transport instead of a lower order P_N equation, it was conjectured that the axial expansion method would not suffer the same instability

in problems with bare fuel. Additionally, the lack of a nodal solver in the axial direction led to predictions that the method would not suffer from the same instability present in traditional 2D/1D for problems with very thin axial slices due to how the transverse leakage is interpolated.

The axial expansion method is then formulated in this work. The derivation is performed from the base transport equation and the axial expansion equations are composed in a matrix-vector form. MOC is then applied to this form of the equations to give the algebraic system of equations that can be solved. In addition, the necessary considerations for CMFD linkage are described. Following this, the matrix exponentials present in the MOC form of the equations were investigated and a faster method to solve them was created in the form of matrix exponential tables. The additional memory needed by these tables and other aspects of the method was then investigated. It was determined that the additional memory needed by the LPAEM could potentially be substantial, but the additional memory needed by the matrix exponential tables was relatively negligible.

The results from Table 5.1 show that the axial expansion method is about as accurate as the current MPACT default isotropic leakage 2D/1D approximation for the 1D/1D problems. Furthermore, the results show that the difference in extruded cell leakage vs. pin cell leakage is small. These results suggest that the axial expansion method is competitive in terms of accuracy with the current MPACT 2D/1D approximation for identical meshes.

The results from Figures 5.2, 5.13, and 5.14 show that axial expansion greater than linear is likely unnecessary for most problems. The difference quickly becomes quite small for the examined problems, becoming less than 10 pcm different after $N = 2$ and less than 1 pcm after $N = 4$. This suggests that linear axial expansion alone might be a preferable alternative to MPACT's current 2D/1D approximation for systems where it breaks down.

The results from Figure 5.4 show that the axial expansion methods experience more consistent and smooth local pin-profile errors compared with MPACT, and although the extruded cell leakage results in slightly lower errors, the shape is similar to that of the pin-leakage method. This suggests that local effects will likely be improved, or at least be competitive, by using the axial expansions rather than the traditional 2D/1D method in MPACT. The nature of the axial expansion gives additional intra-slice power resolution (not shown explicitly here) through the non-flat nature of the axial flux solution that is not present in results from the traditional 2D/1D method in MPACT.

So, for the 2D pseudo-reactor system configurations, the axial expansion methods are competitive with MPACT's 2D/1D in terms of accuracy. Additionally, the naturally created intra-nodal power resolution for pin cells due to the non-flat axial expansion might lead to some improvements in multi-physics calculations, which rely on accurate axial power shapes.

Results in Tables 5.2 and 5.3 demonstrated the stability of the axial expansion method in contrived systems with thin axial slices. These systems showed the instability that thin slices can create, and while some of the instability seemed to come from CMFD, which is a requirement for

a traditional 2D/1D calculation in MPACT, the ability of the axial expansion method to converge in those problems with CMFD enabled indicates that at least some of the instability is inherent in traditional 2D/1D methods themselves.

In Table. 5.4, the stability of the method in systems with void-like regions surrounding fuel was demonstrated. In these results, CMFD seemed effective at accelerating the axial expansion method indicating that any instability from CMFD was likely minor. The fact that traditional 2D/1D methods were unable to converge for this problem demonstrates the theory that void-like regions surrounding fuel can cause instability in traditional 2D/1D. Along with the thin slice results, these results demonstrate robustness of the axial expansion method in systems where traditional 2D/1D fails to converge for a 1D/1D problem.

Results in Tables 5.5 and 5.6 show good agreement between the axial expansion implementation and the reference calculation. This agreements indicate the implementation is correct and further comparisons can be done using the new axial expansion capabilities in MPACT.

In Tables 5.5 and 5.6, we also see that the errors from the axial expansion method are close to those observed in the traditional 2D/1D calculation for the same mesh. In fact, these results show that the axial expansion method results in similar global eigenvalue calculations as had previously been seen. So, for these 3D configurations, the axial expansion methods are competitive with MPACT's 2D/1D in terms of accuracy.

Table 5.7 demonstrates the stability in problems with void-like regions for a 3D pin cell problem. Again, we observe that traditional 2D/1D fails to converge in these problems, yet the axial expansion method both converges and is effectively accelerated by CMFD. The radial slices of the fast flux shown in Figure 5.12 indicate that the dominant source of fast flux in the bare fuel region of the pin cell is from the axial leakage. This dominance of the axial leakage over the local coarse cell production is a driving force of the instability in traditional 2D/1D, and is predicted to occur in systems with bare fuel above moderated fuel.

Results in Tables 5.9 and 5.10 demonstrate the ability of the LPAEM to converge in the cold version of KRITZ-2:1, a system that has been previously attempted to be used as a validation problem for MPACT. This stability extends the previous results if the 1D/1D pincell with void as well as the 3D KRITZ-2 pin cell model, both of which showed these same improved stability properties. These results now show those same stability properties, but on a much larger scale with the full KRITZ-2:1 cold critical experiment. Along with Table 5.8, the eigenvalue error present in the axial expansion calculation seems to be in line with the error caused by using TCP0 scattering instead of higher order anisotropic scattering. Since the implementation in MPACT is limited to TCP0, this error is presently necessary in axial expansion calculations.

Results in Tables 5.11, 5.12, and 5.13 reiterate those same results with the hot KRITZ-2:1 system. The only additional observation is that this problem is a bit more stable for traditional

2D/1D since it converges for the bare fuel cutoff case, which the cold KRITZ-2:1 model did not. This is likely the result of the increased water height resulting in smoother axial variation of the flux in the submerged fuel. Similarly the eigenvalue error present in the axial expansion calculation seems to again be in line with the error caused by using TCP0 scattering instead of higher order anisotropic scattering.

Results in Figures 5.20 and 5.21 show that the calculation of matrix exponentials is much faster than the originally implemented Pade approximations. In fact, these results show us that even for both cases where the matrix exponential calculations were analytic, up to the 2×2 matrix, we still observe that the matrix exponential tables are far faster. Furthermore, the additional pre-computational time and required additional memory is shown to be negligible even for relatively large values of N in Figures 5.22 and 5.23 As such, it was determined that matrix exponential tables would take over as the primary method of computing matrix exponentials for this method.

This work has shown a limitation of traditional 2D/1D and proposed an alternative method to fill this limitation based upon the axial expansion method developed by ANL for Proteus-MOC. The method derived here uses a new higher-order discretization and the axial coupling has been reformulated to reduce memory usage and allow it to be compatible with non-extruded FSR meshes. Additionally, the explicit use of Legendre polynomials in the new discretization lead to the development of matrix exponentials that have demonstrated significant time savings with minimal computational costs, even when compared to analytic computations possible for lower order expansions. The method has been demonstrated to be effective with respect to accuracy compared to traditional 2D/1D, but more importantly it has been shown to be stable for problems with bare fuel above submerged fuel, which was the limitation we desired to fill. Overall, the hope is that this method will provide a robust alternative in systems where traditional 2D/1D is too unstable to converge.

6.2 Future Work

The theoretical progress for this project is mostly limited to the contents of Chapters 3 and 4 of this document. The discovery of the viability of matrix exponential tables for these problems precludes the need for additional research in efficient matrix exponential calculations for this problem, and the method is complete in terms of derivation.

The implementation aspect of this project currently exists in a relatively robust, if somewhat inefficient, state. The method is implemented in MPACT with full support for ray-wise multi-threading and spatial message passing parallelism. The implementation now makes use solely of the matrix exponential tables method for matrix exponential calculations. Matrix exponential tables are computed once at the start of problem (which takes on the order of 0.01 seconds) and never need to

be computed again. The tables are cross section independent, so multi-physics calculations do not need additional table computations after each multi-physics step. Implementation is properly linked to MPACT's CMFD and can run in 3D with or without CMFD acceleration (traditional 2D/1D requires CMFD acceleration in MPACT). The implementation is properly linked with MPACT's shielding calculations and can accept cross sections that require shielding computations.

With the implementation completed in MPACT, further work can be done in the investigation of the effectiveness of the method as well as investigation of various approximations that can be introduced to decrease computational costs. The following are proposed areas of further investigation for this work should there exist desire to pursue the method further:

1. Despite some optimizations and adoption of matrix exponential tables, the implementation still needs more thorough optimization to make appropriate timing and memory comparisons with traditional 2D/1D in MPACT. Included in this is the fact that the implementation currently requires a fully anisotropic storage of the coarse cell axial leakage in between iterations. This represents a nontrivial amount of additional memory. Investigation of potentially reducing the leakage to net current, or more likely angular moments, to reap the computational savings should be performed to determine the consequences of such an approximation.

   Additionally, it is observed in Figures 5.2 and 5.14 that $N = 1$ or $N = 2$ seem to provide good convergence for the eigenvalue result in most problems. It should be investigated whether higher order axial expansion approximations provide better accuracy offset by computational costs, when compared to lower order axial expansions on a finer axial mesh.

   Currently, $N = 1$ runs can be between 2 and 16 time slower than $N = 0$ and $N = 2$ runs can be between 2 and 18 times slower still than $N = 1$ runs. The exact additional computational cost varies greatly with size of the problem. Where exactly the additional costs are seen should be profiled and the reason for nonlinear dependence on problem size should be investigated. This could further aid decisions involving higher order axial expansions versus finer axial meshes.

2. It is believed that the axial expansion method does in fact spatially converge to the transport solution as the slice sizes go to 0 along with other spatial refinement such as ray spacing going to 0 and FSR size going to 0. This is because it is a direct discretization of the 3D transport equation. An analytic proof of this is a step that could potentially give further insight into the difference between the axial expansion method and traditional 2D/1D. Additionally, such a proof may reveal where exactly errors in the approximation are pronounced and aid with optimal balance between expansion order and mesh thickness.

3. One of the largest limiting factors of the method in terms of accuracy at this point appears

to be the lack of anisotropic scattering. Results indicate that the implementation may in fact serve to sufficiently validate MPACT using the KRITZ-2 experiments if anisotropic scattering were available. Implementation of anisotropic scattering for this method should be pursued in MPACT, but due to the current computational costs of the method, it is suggested that optimization work is first attempted since anisotropic scattering can add significant computational costs.

4. The axial expansion method implicitly gives an intra-nodal axial shape in each slice. This could be of value in multi-physics computations if properly utilized since higher order coupling between the transport solution and the other multi-physics solutions, such as the thermal hydraulics or depletion, could potentially provide increased accuracy. Thus far, all LPAEM runs in MPACT have been single-physics neutron transport calculations, but further investigation into potential multi-physics implications could be useful.

Bibliography

[1] R.A. Knief. *Nuclear Engineering Theory and Technology of Commercial Nuclear Power*. La Grange Park, IL, USA: American Nuclear Society, 2014.

[2] J.R. Lamarsh. *Introduction to Nuclear Reactor Theory*. La Grange Park, IL, USA: American Nuclear Society, 2002.

[3] E.E. Lewis. *Fundamentals of Nuclear Reactor Physics*. Burlington, MA, USA: Elsevier, 2008.

[4] J.J. Duderstadt and L.J. Hamilton. *Nuclear Reactor Analysis*. New York, NY, USA: John Wiley & Sons, Inc., 1976.

[5] M.M.R. Williams. *Mathematical Methods in Particle Transport Theory*. London, UK: Butterworth & Co, 1971.

[6] J.R. Askew. *A characteristics formulation of the neutron transport equation in complicated geometries*. Tech. rep. OECD/NEA, NEA/NSC/DOC, 1972.

[7] F. Fitzgerald. "Parallel 3-D Method of Characteristics with Linear Source and Advanced Transverse Integration". PhD thesis. Nuclear Engineering and Radiological Sciences: University of Michigan, 2020.

[8] G. Yuan. "Convergence of P_N approximation for the neutron transport equation with reflective boundary condition". In: *Journal of Mathematical Physics* 41 (2000), pp. 867–874.

[9] L. Snoj, J. Gehin, and I. Remec. *KRITZ-2:1 Experiment on Regular H2O/Fuel Pin Lattices with Low Enriched Uranium Fuel at Temperatures 19.7 °C and 248.5 °C*. Tech. rep. OECD/NEA, NEA/NSC/DOC, 2006.

[10] L. Snoj, J. Gehin, and I. Remec. *KRITZ-2:13 Experiment on Regular H2O/Fuel Pin Lattices with Low Enriched Uranium Fuel at Temperatures 22.1 °C and 243 °C*. Tech. rep. OECD/NEA, NEA/NSC/DOC, 2006.

[11] L. Snoj, J. Gehin, and I. Remec. *KRITZ-2:19 Experiment on Regular H2O/Fuel Pin Lattices with Mixed Oxide Fuel at Temperatures 21.1 °C and 235.9 °C*. Tech. rep. OECD/NEA, NEA/NSC/DOC, 2006.

[12] L Snoj, I Kodeli, and I Remec. “Evaluation of the KRITZ-2 Criticality and Reaction Rate Benchmark Experiments”. In: *Nuclear Science and Engineering* 178 (2014), pp. 496–508.

[13] I. Kodeli and L. Snoj. “Evaluation and Uncertainty Analysis of the KRITZ-2 Critical Benchmark Experiments”. In: *Nuclear Science and Engineering* 171 (2012), pp. 231–238.

[14] S. Jeon and H.G. Joo. “Analyses of the B&W-1810 and KRITZ-2 Critical Experiments with nTRACER”. In: Advances in Nuclear Fuel Management IV 2009. Jeju, Korea, 2018.

[15] *Benchmark on the KRITZ-2 LEU and MOX Critical Experiments*. Tech. rep. OECD/NEA, NEA/NSC/DOC, 2006.

[16] M. Jarrett, B. Kochunas, and T. Downar. *KRITZ-2 Benchmark Results with MPACT*. Tech. rep. CASL, 2018.

[17] S. Palmtag and S. Stimpson. *MPACT Validation with Critical Experiments*. Tech. rep. CASL, 2017.

[18] Abel Marin-Lafleche, Micheal A. Smith, and Changho Lee. “Proteus-MOC: A 3D Deterministic Solver Incorporating 2D Method of Characteristics”. In: ANS M&C 2013. Sun Valley, ID, USA, 2013.

[19] Nicholas F. Herring, Benjamin S. Collins, and Thomas J. Downar. “Legendre Polynomial Expansion for Axial Transport Approximations”. In: ANS Winter Conference 2020. Chicago, IL, USA, 2020.

[20] Nicholas F. Herring, Benjamin S. Collins, and Thomas J. Downar. “Legendre Polynomial Expansion for Axial Transport Approximations”. In: ANS M&C 2021. Raleigh, NC, USA, 2021.

[21] Mathieu Hursin. “Full Core, Heterogeneous, Time Dependent Neutron Transport Calculations with the 3D Code DeCART”. PhD thesis. Nuclear Engineering: University of California Berkeley, 2010.

[22] J.Y. Cho et al. “Axial SP_N and Radial MOC Coupled Whole Core Transport Calculation”. In: *Journal of Nuclear Science and Technology* 44 (2007), pp. 1156–1171.

[23] N. Soppera, M. Bossant, and E. Dupont. “CRX : A Code for Rectangular and Hexagonal Lattices Based on the Method of Characteristics”. In: *Annals of Nuclear Energy* 25 (1998), pp. 547–565.

[24] H.J. Yoo and N.Z. Cho. “3D/2D rotational plane slicing method for 3D whole-core transport calculation”. In: *Annals of Nuclear Energy* 87 (2016), pp. 30–38.

[25] S.G. Stimpson. “An Azimuthal, Fourier Moment-Based Axial SN Solver for the 2D/1D Scheme”. PhD thesis. Nuclear Engineering and Radiological Sciences: University of Michigan, 2015.

[26] M.G. Jarrett. “A 2D/1D Neutron Transport Method with Improved Angular Coupling”. PhD thesis. Nuclear Engineering and Radiological Sciences: University of Michigan, 2018.

[27] B. Faure et al. “A 2D/1D Algorithm for Effective Cross-Section Generation in Fast Reactor Neutronic Transport Calculations”. In: *Nuclear Science and Engineering* 192 (2018), pp. 40–51.

[28] T. Zhang et al. “A Variational Nodal Approach to 2D/1D Pin Resolved Neutron Transport for Pressurized Water Reactors”. In: *Nuclear Science and Engineering* 186 (2017), pp. 120–133.

[29] Zhouyu Liu et al. “The material-region-based 2D/1D transport method”. In: *Annals of Nuclear Energy* 128 (2018), pp. 1–11.

[30] Y.Q. Zheng, S.Y. Choi, and D.J. Lee. “A new approach to three-dimensional neutron transport solution based on the method of characteristics and linear axial approximation”. In: *Journal of Computational Physics* 350 (2017), pp. 25–44.

[31] Michael Jarrett. personal communication. Dec. 20, 2021.

[32] Blake Kelley. “An Investigation of 2D/1D Approximations to the 3D Boltzmann Transport Equation”. PhD thesis. Nuclear Engineering and Radiological Sciences: University of Michigan, 2015.

[33] Zackary Dodson. “Linear Diffusion Acceleration for Neutron Transport Problems”. PhD thesis. Nuclear Engineering and Radiological Sciences: University of Michigan, 2021.

[34] Z. Dodson, B. Kochunas, and E. Larsen. “The Stability of Linear Diffusion Acceleration Relative to CMFD”. In: *Journal of Nuclear Engineering* 2 (2021), pp. 336–344.

[35] Chen Zhao et al. “Improved leakage splitting method for the 2D/1D transport calculation”. In: *Progress in Nuclear Energy* 105 (2018), pp. 202–210.

[36] G.I. Bell and S. Glasstone. *Nuclear Reactor Theory*. New York, NY, USA: Van Nostrand Reinhold Company, 1970.

[37] Alain Hébert. *Applied Reactor Physics*. Montréal, Quebec, Canada: Presses Internationales Polytechnique, 2009.

[38] A.K. Prinja and E.W. Larsen. “Handbook of Nuclear Engineering”. In: Springer, 2010. Chap. General Principles of Neutron Transport, pp. 427–542.

[39] I. Lux and L. Koblinger. *Monte Carlo Particle Transport Methods: Neutron and Photon Calculations*. Boca Raton, FL, USA: CRC Press, 1991.

[40] E.E. Lewis and W.F. Miller. *Computational Methods of Neutron Transport*. La Grange Park, Illinois, USA: John Wiley & Sons, Inc., 1993.

[41] N. Soppera, M. Bossant, and E. Dupont. "JANIS 4: An Improved Version of the NEA Java-based Nuclear Data Information System". In: *Nuclear Data Sheets* 120 (2014), pp. 294–296.

[42] R.C. Block et al. "Handbook of Nuclear Engineering". In: Springer, 2010. Chap. Neutron Cross Section Measurements, pp. 1–81.

[43] Hervasio Guimarães de Carvalho. "Total Cross Sections of 208-Mev and 315-Mev Protons for Light Elements". PhD thesis. Nuclear Engineering: North Carolina State University, 1954.

[44] Alain Hébert. "Handbook of Nuclear Engineering". In: Springer, 2010. Chap. Multigroup Neutron Transport and Diffusion Computations, pp. 751–911.

[45] K.D. Lathrop. "Ray Effects in Discrete Ordinates Equations". In: *Nuclear Science and Engineering* 32 (1968), pp. 357–369.

[46] J.K. Shultis and R.E. Faw. *Radiaiton Shielding*. Upper Saddle River, NJ, USA: Prentice Hall PTR, 1996.

[47] K.D. Lathrop. "Remedies For Ray Effects". In: *Nuclear Science and Engineering* 45 (1971), pp. 255–268.

[48] N.F. Herring. "Ray Effects Mitigation in S_N Problems through General Collision Monte Carlo Coupling and Numerical Validation of the THOR S_N Code for Nuclear Nonproliferation Applications". MA thesis. Nuclear Engineering: North Carolina State University, 2018.

[49] R.E.J. Miller. "The Importance of Discrete-Ordinate Ray Effects in Fast Reactor Design Studies". In: *Transactions of the American Nuclear Society* 32 (1970), pp. 629–630.

[50] J.J. Jarrell and M.L. Adams. "Discrete-Ordinates Quadrature Sets Based on Linear Discontinuous Finite Elements". In: ANS M&C 2011. Rio de Janeiro, Brazil, 2011.

[51] I.K. Abu-Shumays. "Compatible Product Angular Quadrature for Neutron Transport in x-y Geometry". In: *Nuclear Science and Engineering* 64 (1977), pp. 299–316.

[52] Yaqi Wang et al. "Rattlesnake: A MOOSE-Based Multiphysics Multischeme Radiation Transport Application". In: *Nuclear Technology* 207 (2021), pp. 1047–1072.

[53] M.D. Brough and C.T. Chudley. "Characteristic Ray Solutions of the Transport Equation". In: *Advances in Nuclear Science and Technology* 12 (1980), pp. 1–31.

[54] R.A. Karam and K.D. Kirby. *Assessment of flat-flux and flat-source approximations in generating resonance cross sections. Final report*. Tech. rep. ORO–4750-3, 1975.

[55] A.P. Fitzgerald, B.M. Kochunas, and T.J. Downar. “Improved Formulation of the Method of Characteristics with Linear Source for 2D/1D and Multiphysics Calculations”. In: ANS M&C 2019. Portland, OR, USA, 2019.

[56] N.F. Herring et al. “Improved Anisotropic Linear Source Formulation for Multiphysics Problems”. In: PHYSOR 2020. Cambridge, England, UK, 2020.

[57] A Vidal-Ferràndiz. “Optimized Eigenvalue Solvers for the Neutron Transport Equation”. In: International Conference on Computational Science. Wuxi, China, 2018.

[58] E.W. Larsen. “Diffusion-synthetic acceleration methods for discrete-ordinates problems”. In: *Transport Theory and Statistical Physics* 13 (1983), pp. 107–126.

[59] E.W. Larsen and B.W. Kelley. “The Relationship between the Coarse-Mesh Finite Difference and the Coarse-Mesh Diffusion Synthetic Acceleration Methods”. In: *Nuclear Science and Engineering* 178 (2014), pp. 1–15.

[60] L.R. Cornejo and D.Y. Anistratov. “Nonlinear Diffusion Acceleration Method with Multigrid in Energy for k-Eigenvalue Neutron Transport Problems”. In: *Nuclear Science and Engineering* 184 (2017), pp. 514–526.

[61] Benjamin Collins et al. “Stability and Accuracy of 3D Neutron Transport Simulations Using the 2D/1D Method in MPACT”. In: *Journal of Computational Physics* 326 (2016), pp. 612–628.

[62] Francois Fevotte and Bruno Lathuiliere. “MICADO : Parallel Implementation of a 2D1D Iterative Algorithm for the 3D Neutron Transport Problem in Prismatic Geometries”. In: ANS M&C 2013. Sun Valley, ID, USA, 2013.

[63] G. Zhang and W.S. Yang. “Quadratic axial expansion function with sub-plane acceleration scheme for the high-fidelity transport code PROTEUS-MOC”. In: *Annals of Nuclear Energy* 148 (2020).

[64] T.N. Nguyen et al. “Implementation of the transient fixed-source problem in the neutron transport code PROTEUS-MOC”. In: *Annals of Nuclear Energy* 129 (2019), pp. 199–206.

[65] A. Hsieh, G. Zhang, and W.S. Yang. “Consistent Transport Transient Solvers of the High-Fidelity Transport Code PROTEUS-MOC”. In: *Nuclear Science and Engineering* 194 (2020), pp. 508–540.

[66] G. Zhang et al. “Consistent pCMFD Acceleration Schemes of the Three-Dimensional Transport Code PROTEUS-MOC”. In: *Nuclear Science and Engineering* 193 (2019), pp. 828–853.

[67] Sooyoung Choi and Deokjung Lee. “Three-dimensional method of characteristics/diamond-difference transport analysis method in STREAM for whole-core neutron transport calculation”. In: *Computer Physics Communications* 260 (2020).

[68] M A Smith, E E Lewis, and B C Na. *Benchmark on Deterministic Transport Calculations Without Spatial Homogenisation - A 2-D/3-D Mox Fuel Assembly Benchmark*. Tech. rep. OECD/NEA, NEA/NSC/DOC, 2003.

[69] N. Horelik et al. “MIT BEAVRS: Benchmark for Evaluation and Validation of Reactor Simulations”. In: ANS M&C 2013. Sun Valley, ID, USA, 2013.

[70] N.J. Higham. *Functions of Matrices: Theory and Computation*. Philadelphia, PA, USA: Society for Industrial and Applied Mathematics, 1985.

[71] C. Moler and C. Van Loan. “Nineteen Dubious Ways to Compute the Exponential of a Matrix”. In: *SIAM Review* 20 (1978), pp. 801–836.

[72] C. Moler and C. Van Loan. “Nineteen Dubious Ways to Compute the Exponential of a Matrix, Twenty-Five Years Later”. In: *SIAM Review* 45 (2003), pp. 3–49.

[73] M. Arioli, B. Codenotti, and C. Fassino. “The Padeé method for computing the matrix exponential”. In: *Linear Algebra and its Applications* 240 (1996), pp. 111–130.

[74] M.N. Baldwin. *Critical Experiments Supporting Close Proximity Water Storage of Power Reactor Fuel*. Babcock & Wilcox, 1979.

[75] C.A. Wemple. “Benchmarking the HELIOS-2 ENDF/B-VII Library: B&W-1484 and DIMPLE S-06 Criticals”. In: Advances in Nuclear Fuel Management IV 2009. Hilton Head Island, South Carolina, USA, 2009.

[76] KO. Ott and R.J. Neuhold. *Nuclear Reactor Dynamics*. La Grange Park, Illinois, USA: American Nuclear Society, 1985.